MReadings: MR in RT

8th Edition 2022

siemens-healthineers.com/magnetom-world-rt

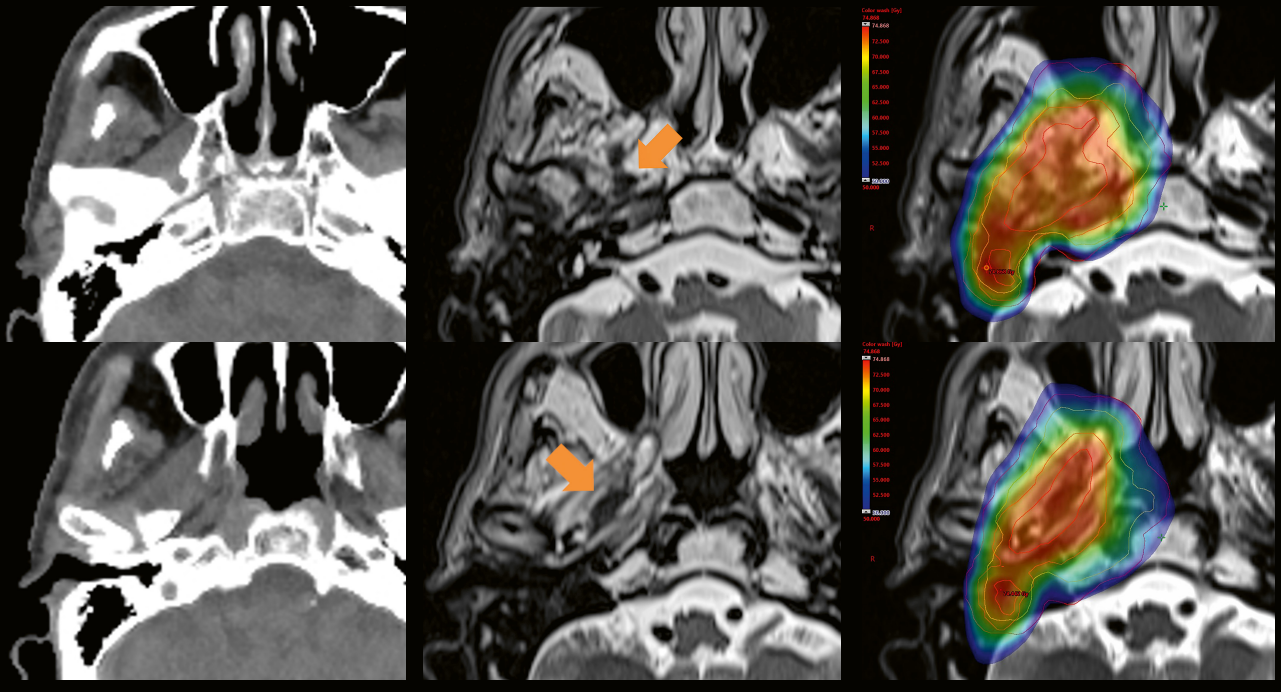

Not for distribution in the US

SIEMENS Healthineers

The entire editorial staff at University of California at Los Angeles (UCLA) and at Siemens Healthineers extends their appreciation to all the radiation oncologists, radiologists, technologists, physicists, experts, and scholars who donate their time and energy – without payment – in order to share their expertise with the readers of MAGNETOM Flash and the MReadings.

MAGNETOM Flash – Imprint

© 2022 by Siemens Healthcare GmbH,
All Rights Reserved

Publisher:
Siemens Healthcare GmbH
Magnetic Resonance,
Karl-Schall-Str. 6, D-91052 Erlangen, Germany

Editor-in-chief:
Antje Hellwich
(antje.hellwich@siemens-healthineers.com)

Guest editor:
Daniel Low, Ph.D., FAAPM, FASTRO
Professor and Vice Chair of Medical Physics,
Radiation Oncology
Professor of Radiological Sciences
UCLA
Los Angeles, CA, USA

Editorial Board:
Rebecca Ramb, Ph.D.; Heiko Meyer, Ph.D.; Wellesley Were; Nadine Leclair, M.D.; Jane Kilkenny

Review Board:
Nuria Escobar Corral, Ph.D.; Glen Roberts; Elena Nioutsikou, Ph.D.; Daniel Fischer; Martin Requardt, Ph.D.

Copy Editing:
Sheila Regan, Jen Metcalf, UNIWORKS,
www.uni-works.org
(with special thanks to Kylie Martin)

Layout:
Agentur Baumgärtner,
Friedrichstr. 4, D-90762 Fürth, Germany

Production:
Norbert Moser,
Siemens Healthcare GmbH

Printer:
Schmidl & Rotaplan Druck GmbH,
Hofer Str. 1, D-93057 Regensburg, Germany

Note in accordance with § 33 Para.1 of the German Federal Data Protection Law: Despatch is made using an address file which is maintained with the aid of an automated data processing system.

MAGNETOM Flash is sent free of charge to Siemens Healthineers MR customers, qualified physicians, technologists, physicists and radiology departments throughout the world. It includes reports in the English language on magnetic resonance: diagnostic and therapeutic methods and their application as well as results and experience gained with corresponding systems and solutions. It introduces from case to case new principles and procedures and discusses their clinical potential. The statements and views of the authors in the individual contributions do not necessarily reflect the opinion of the publisher.

The information presented in these articles and case reports is for illustration only and is not intended to be relied upon by the reader for instruction as to the practice of medicine. Any health care practitioner reading this information is reminded that they must use their own learning, training and expertise in dealing with their individual patients. This material does not substitute for that duty and is not intended by Siemens Healthcare to be used for any purpose in that regard. The drugs and doses mentioned herein are consistent with the approval labeling for uses and/or indications of the drug. The treating physician bears the sole responsibility for the diagnosis and treatment of patients, including drugs and doses prescribed in connection with such use. The Operating Instructions must always be strictly followed when operating the MR system. The sources for the technical data are the corresponding data sheets. Results may vary.

Partial reproduction in printed form of individual contributions is permitted, provided the customary bibliographical data such as author's name and title of the contribution as well as year, issue number and pages of MAGNETOM Flash are named, but the editors request that two copies be sent to them. The written consent of the authors and publisher is required for the complete reprinting of an article.

We welcome your questions and comments about the editorial content of MAGNETOM Flash. Please contact us at magnetomworld.team@siemens-healthineers.com

Manuscripts as well as suggestions, proposals and information are always welcome; they are carefully examined and submitted to the editorial board for attention. MAGNETOM Flash is not responsible for loss, damage, or any other injury to unsolicited manuscripts or other materials. We reserve the right to edit for clarity, accuracy, and space. Include your name, address, and phone number and send to the editors, address above.

MReadings: MR in RT is also available online:

www.siemens-healthineers.com/magnetom-world-rt

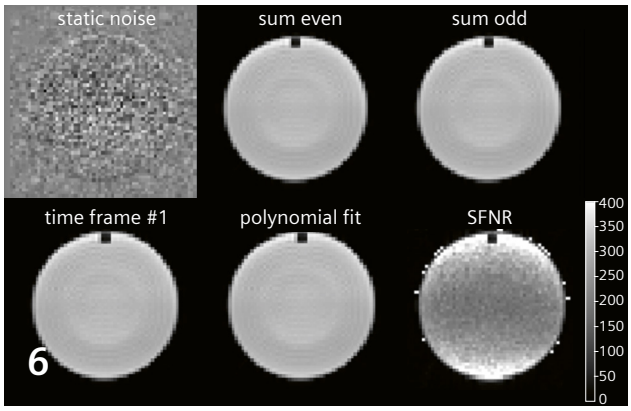

Commissioning and QA for dedicated radiation oncology MRI scanners

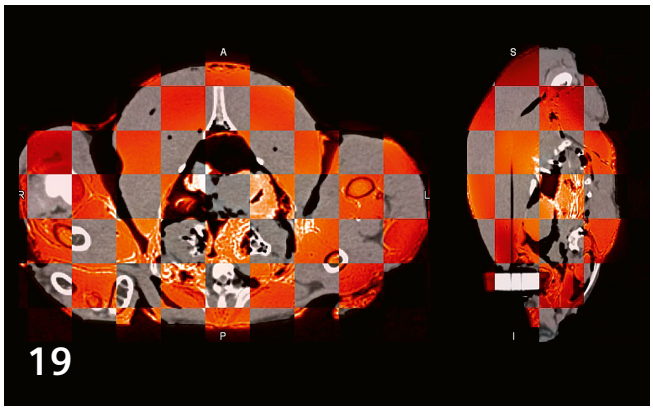

PETRA for catheter detection in interstitial HDR Brachytherapy

Editorial Comment

Quality Assurance

Brachytherapy

Cover from *The Application and Utility of Radiotherapy Planning MRI at the Cancer Institute Hospital of JFCR* by Yasuo Yoshioka, M.D., Ph.D., Director of the Department of Radiation Oncology, Cancer Institute Hospital of the Japanese Foundation for Cancer Research (JFCR), Tokyo, Japan

Radiation Therapy

Product News

Meet Siemens Healthineers

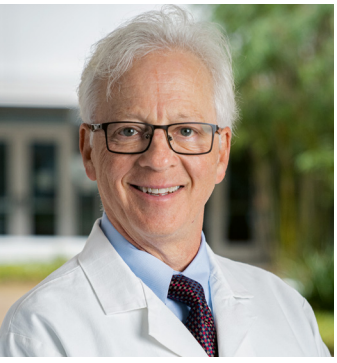

Dr. Low is the Vice Chair of Medical Physics in the Department of Radiation Oncology at University of California at Los Angeles. Before joining UCLA in 2010, he was a professor and Director of Medical Physics in the Department of Radiation Oncology at Washington University.

He earned his Ph.D. in Physics in 1988 from Indiana University and was a postdoctoral fellow for two years in radiation therapy physics at MD Anderson Cancer Center.

He is a Fellow of the American Association of Physicists in Medicine and the American Society of Radiation Oncology and is certified by the American Board of Radiology in Radiation Therapy Physics.

He has been principal investigator on five National Institutes of Health R01 grants and has published almost 300 peer-reviewed manuscripts. His areas of research interests include magnetic resonance imaging in radiation therapy and human breathing motion.

Dear readers and colleagues,

Radiation therapy technology has continuously evolved since 3-dimensional (3D) conformal radiation therapy was introduced in the 1990s. The goal of conformal RT has been to provide radiation doses that hug the tumor while avoiding nearby critical organs. This 3D quantitation of tumor geometry led to the method of explicitly defining regions of suspected disease and the use of spatial margins to account for errors and variability that could not be eliminated using the current technology [1]. Image guidance further enabled the tumor and internal organs to be reproducibly positioned such that the highly conformal dose distributions matched the patient's anatomy for each treatment. This in turn allowed the reduction of margins, reducing the overall irradiated volumes and reducing toxicity [2]. This technology has allowed the quality of radiation therapy to improve treatment efficacy to the point that many modern clinical trials focus on reducing side effects as much as they focus on improving local control and ultimately long-term survival [3].

Modern radiation therapy image guidance was initiated by the commercial availability of cone-beam CT (CBCT), even though co-registered ultrasound had been available for a limited number of tumor sites, and the skull has always been an excellent bony surrogate for lesions in the brain. CBCT provides 3D anatomical information in the form of normalized tissue linear attenuation coefficients, which have contrast characterizations similar to those of conventional CT, in that low-density tissues such as lung have small attenuations, soft-tissues have moderate attenuation, and bone has the greatest attenuation. The similarity between CBCT and CT simulation images allows reference images generated using the CT simulation to be straightforwardly compared against CBCT for patient alignment.

Both the planning and delivery of conformal radiation therapy dose distributions are greatly improved when the efficacy of the imaging technology is improved. Computed tomography has been the mainstay imaging modality for radiation therapy treatment planning. Its qualities include high spatial integrity, rapid acquisition time, highly consistent and quantifiable images, reasonable contrast, and relatively low cost. On the other hand, it is relatively inflexible with respect to the type of information it gathers and provides to the clinician.

Magnetic resonance imaging shares some of the features of computed tomography, including providing a 3D image, but there are features of magnetic resonance images that are superior to those of computed tomography, specifically its improved soft tissue contrast and tremendous flexibility in design, which allows acquisition of functional image data for purposes of tumor localization, tumor biology characterization, tumor environment characterization, and radiation response information. On the other hand, magnetic resonance imaging suffers from poorer spatial integrity, and a difficulty in securing stable image quantification, especially between clinics. A great deal of effort has gone into improving the spatial integrity of magnetic resonance imaging, to the point that the spatial integrity is considered a relatively minor and manageable issue for radiation therapy.

One of the most important promises of magnetic resonance imaging is its use in radiation therapy treatment planning and assessment via MR simulation. MR simulation parallels CT simulation in that the patient is imaged in treatment position with positioning and immobilization accessories. The MR simulation procedure is typically considered as a supplement to CT simulation, but in fact the information the clinician wants to know, namely normal organ segmentation, tumor delineation, functional information, and treatment response, are better gleaned from MR simulation than CT simulation. Due to need for electron density information for treatment planning and the wide-spread adoption of X-ray or cone-beam CT based positioning, there remains a need for the information a CT simulation provides. Efforts have been made to provide that information using just an MR image dataset [4], but those efforts have not led to wide-spread adoption of what is termed MR-only simulation.

One reason for this is, as previously mentioned, CBCT is the dominant image-guided technology, so having a

MRI allows acquisition of functional data for purposes of tumor localization, tumor biology characterization, tumor environment characterization, and radiation response information.

reference image with similar tissue conspicuity than the positioning image aids in patient positioning.

The introduction of MR-guided radiation therapy (MRgRT) machines, which combine magnetic resonance imaging and linear accelerators, may alter this calculus. At their most basic, these systems use magnetic resonance imaging rather than CBCT or radiographic imaging for positioning. This implies that reference images with CT-like contrast may be more difficult to use for setup. This is in fact the case; our clinic acquires a MR-simulation image using our MRgRT system so that we have a reference image that has tissue contrast that matches the contrast of the setup images. While MRgRT systems provide improved soft tissue contrast, their benefits extend much deeper. Because they can acquire images during treatment, gating with these systems is straightforward. The improved image quality also enables more accurate and sophisticated adaptive radiation therapy approaches, which have been shown to potentially improve outcomes, both for tumor control and complications [5, 6]. These features, along with clinical evidence of their effectiveness, may accelerate the adoption of MRgRT systems.

Whether MRgRT replaces a large segment of CBCT-based machines remains to be seen, but its impact on MR in RT will be significant. The radiation therapy community is paying more attention to the use of MR for treatment planning and assessment monitoring, the importance of which is being accelerated by MRgRT. This will in turn demonstrate the benefits of MR in RT to an increasingly widening array of radiation therapy departments, and since much of the benefit of MRgRT is access to an in-house MR scanner, those departments with MRgRT will themselves deepen their appreciation for the use of MR in RT. It is likely, therefore that even a relatively small adoption rate of MRgRT will further accelerate the importance and adoption of MR in RT.

The increased importance of MR imaging for radiation therapy will in turn cause radiation therapy departments to examine their roadmaps for the time when their CT simulators need replacement. Replacing one CT with another will offer limited benefits to the department, while acquiring an MR simulator will open their department to the myriad of opportunities that MR simulation offers. It will be up to the vendors and the rest of the community to make this transition painless and affordable, offering convenient and accurate simulated CT scans for their CBCT and other X-ray related alignment tools. These clinics will in turn thrive, offering their patients the benefits of improved treatment accuracy and functional-response based adaptation. When a radiation oncology department owns the MR scanner, it will be willing and able to conduct the necessary quality control to provide stable image values that AI algorithms will need to optimally function. Ideally the CT to MR trend will snowball to the point that MR simulation will displace CT simulation, providing the clinician with the benefits of improved image quality and process automation.

References

1 International Commission on Radiation Units and Measurements. Prescribing, recording, and reporting photon beam therapy. Bethesda, Md.: International Commission on Radiation Units and Measurements; 1999. 52 p. p.

2 van der Veen J, Nuyts S. Can Intensity-Modulated-Radiotherapy Reduce Toxicity in Head and Neck Squamous Cell Carcinoma? Cancers (Basel). 2017;9(10). Epub 20171006.

3 Chen YP, Chan ATC, Le QT, Blanchard P, Sun Y, Ma J. Nasopharyngeal carcinoma. Lancet. 2019;394(10192):64-80.

4 Han X. MR-based synthetic CT generation using a deep convolutional neural network method. Med Phys. 2017;44(4):1408-19.

5 Henke L, Kashani R, Robinson C, Curcuru A, DeWees T, Bradley J, Green O, Michalski J, Mutic S, Parikh P, Olsen J. Phase I trial of stereotactic MR-guided online adaptive radiation therapy (SMART) for the treatment of oligometastatic or unresectable primary malignancies of the abdomen. Radiother Oncol. 2018;126(3):519-26.

6 Chuong MD, Kirsch C, Herrera R, Rubens M, Gungor G, et al. Long-Term Multi-Institutional Outcomes of 5-Fraction Ablative Stereotactic MR-Guided Adaptive Radiation Therapy (SMART) for Inoperable Pancreas Cancer With Median Prescribed Biologically Effective Dose of 100 Gy10. International Journal of Radiation Oncology*Biology*Physics. 2021;111(3):S147-S8.

Commissioning and Implementing a Quality Assurance Program for Dedicated Radiation Oncology MRI Scanners

Éric Poulin[1,2]; Frederic Lacroix[1,2]; Jean-David Jutras[1,2]

[1]Département de physique, de génie physique et d'optique et Centre de recherche sur le cancer de l'Université Laval, Université Laval, Québec, Canada
[2]Département de radio-oncologie et Axe Oncologie du Centre de recherche du CHU de Québec, CHU de Québec-Université Laval, Québec, Canada

Introduction

Modern radiation oncology treatment, neuro navigation and intraoperative magnetic resonance imaging (MRI) require high geometric fidelity images in combination with high spatial and contrast resolution in order to precisely identify disease extent and adjacent organs at risk (OAR). Magnetic resonance imaging has demonstrated superior soft tissue contrast and was shown to substantially improve target and OAR segmentation accuracy and reliability [1–4]. In addition, it was demonstrated that MRI can reduce treatment-related toxicities due to more accurately delineated OARs [5–7] and identify regions of high tumor burden to facilitate dose escalation [6, 8, 9]. However, conventional computed tomography (CT) simulation is still needed for many disease sites with target and OAR definition performed after MRI-to-CT image registration. This co-registration process may introduce geometrical uncertainties in the range of ~2 mm for the brain [10] and pelvis [11], and up to 5 mm in the abdomen [12] particularly if performed in a radiology setting. Furthermore, MR images are often used without considering the intrinsic geometric fidelity, precision and stability of the MR machine; an approach that may adversely impact dosimetric endpoints and increase the uncertainty beyond co-registration errors. For example, a recent radiosurgery study showed that geometric accuracy becomes a critical issue with small targets; for a target diameter of 3 cm, geometric distortions of 1.5 mm may impact the dose to 95% of the volume, while for targets less than 2 cm, a geometric distortion of 1 mm could significantly affect plan acceptance/quality indices [13].

A 2011 study showed a 78% failure rate during American College of Radiology (ACR) Quality Assurance testing [14]. The impact of geometric distortion in MR-guided radiation therapy has been the object of a recent study which demonstrated a relation between margin and system-related geometric distortion [15]. Neuronavigation accuracy was also shown to be affected by MRI geometric distortion [16]. Overall, the impact from distortions will depend on factors such as the distance of the anatomy from the magnet isocenter, magnetic field strength, and MRI acquisition parameters and sequences, as well as MRI magnet and gradient coil properties. To address these limitations, dedicated MR simulator platforms have been recently introduced with the aim of improving the accuracy of target and OAR delineations required for radiotherapy treatment planning [17]. Moreover, the ACR [18] and American Association of Physicists in Medicine (AAPM) task group's [19–21] guidelines were recently published, addressing the specific aspects of a quality assurance program and commissioning for both cases of MR images used in conjunction with CT, as well as MR images used as a primary modality.

The radiation oncology department of the CHU de Québec-Université Laval is moving into a brand-new facility and accordingly acquired two new MRI machines dedicated to radiation therapy (RT) (MAGNETOM Aera and MAGNETOM Sola, Siemens Healthcare, Erlangen, Germany). The goal of the current paper is therefore to present the authors' experience regarding the commissioning and introduction of a Quality Assurance program for radiation oncology-dedicated MRI scanners.

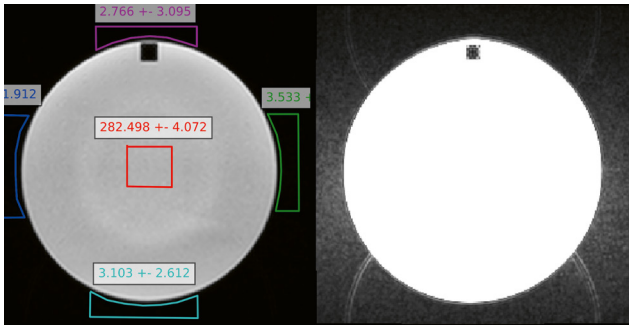

1 Ghosting ratio test, showing ROI locations on a uniform slice of the ACR phantom.

Materials and Methods

MRI systems

The CHU de Québec – Université Laval acquired a MAGNETOM Sola 1.5T MRI simulator (Siemens Healthcare, Erlangen, Germany) dedicated to external-beam RT planning and a Nexaris MR with MAGNETOM Aera 1.5T scanner (Siemens Healthcare, Erlangen, Germany) for interventional brachytherapy. The MAGNETOM Sola is equipped with XQ gradients (45 mT/m, 200 T/m/s), a fixed table (for improved setup accuracy) and the *syngo* MR XA20 software platform with high-end computing (later upgraded to *syngo* MR XA31 on November 2021); it also has the complete QFix solution for radiotherapy simulation (QFix, Avondale, PA, USA) and the DORADOnova MR3T LAP laser system (LAP GmbH Laser Applikationen, Lüneburg, Germany). The Nexaris MR with MAGNETOM Aera is equipped with XQ gradients (45 mT/m, 200 T/m/s), a dockable table, an additional Combi-Suite Dockable Table and was installed with the *syngo* MR E11E software platform on March 2021 and later upgraded to *syngo* MR XA30 on September 2021.

Commissioning and QA

The development of wide bore (70 cm) high field (≥ 1.5T) MRI scanners starting with the Siemens MAGNETOM Espree in 2004 has provided the within-bore space to image patients in Radiation Oncology treatment position and with dedicated immobilization devices in place. Recently, RT-dedicated MRI simulator platforms incorporating external lasers, a flat RT table, and specialized RT workflows have been made available by the major scanner manufacturers and are being installed in Radiation Oncology departments worldwide. The integration of dedicated MRI systems into the radiotherapy workflow necessitates the development of specific Quality Assurance programs as well as acceptance/commissioning tests. The AAPM as well as the Canadian Partnership for Quality Radiotherapy (CPQR) have drafted recommendations for the establishment of Quality Assurance (QA) programs [20–23] and commissioning [20, 22] for dedicated MRI RT systems. All mandatory commissioning tests suggested by the AAPM report 284 [22] were performed and the authors' main findings are shown in the results section. QA tests and associated tolerances are defined so as to ensure the highest possible geometric accuracy, image integrity and stability of RT MRI images. Table 1–4 summarizes the QA program established at the CHU de Québec, which is derived from the most recent AAPM and CPQR recommendations for RT MRI.

Table 1–4 provides an overview of the QA tests to be performed according to their frequency: daily, monthly, semi-annual and annual. Column 1 provides a short description of the test and column 2 outlines its associated analysis method. A variety of analysis methods are used: visual inspection, in-house tools provided by the Siemens Healthineers clinical or service platform, third party software (e.g. AutoQAplus from QA Benchmark, Frederick, MD, USA, and GRADE QA software, Spectronics Medical, Helsingborg, Sweden) or in-house python-based code. Tests in Table 1 are performed by the radiation therapists but the MRI physicists do the ACR analysis. Most monthly, semi-annual and annual tests are performed by the MRI physicists, except for a few specific tests in Table 4 which may only be performed by a certified Siemens Healthineers technician, for example the emergency quench button check. A level 5 service key is necessary in order to run the Siemens Healthineers service platform tests while a level 7 service key is necessary to visualize the detailed results and export the analysis in a PDF file format.

In the QA program established at the CHU de Québec–Université Laval, the lasers are verified and adjusted using the Aquarius phantom from LAP (Lüneburg, Germany). Note that the MAGNETOM Aera scanner (dedicated to brachytherapy) has no external LAP laser system and no UltraFlex antennas. The Siemens Healthineers service phantoms, including a 25 cm sphere for B_0 homogeneity, and various cylindrical phantoms and custom-fitting foam mats for antenna channel uniformity testing are also used. The Siemens Healthineers service tests and platform were previously shown in a white paper [24] and the prescribed methodology was followed here; ACR testing is also shown.

The geometric accuracy of MR images has always been of paramount concern in RT. Geometric distortions in MR images arise from two main sources:

1) system-related effects and
2) patient-related effects.

System-related effects include the B_0 field inhomogeneity and the gradient nonlinearities. Patient-related effects include magnetic field susceptibility variations in the body of the patient, while the chemical-shift artifact is both a system and patient-related effect. The resulting total distortion is highly dependent on the imaging parameters including the specific pulse sequence, acquisition orientation, the field-of-view (FOV), acquisition and RF pulse bandwidth (BW), as well as being patient-dependant. It has been shown that system-related distortions typically are greater than patient-related distortions and that gradient nonlinearities can be the largest-contributing source of geometric distortions [25]. While the patient-specific distortions are more difficult to mitigate, vendors have incorporated two dimensional (2D) or three dimensional (3D) algorithms to automatically correct raw MRI data for known gradient nonlinearities. Such algorithms, however, do not correct for B_0 inhomogeneity and suffer from residual distortion. It has been demonstrated that the residual distortions once vendor-supplied 3D correction factors are applied, can be greater than 1 mm at 10 cm from the isocenter [22]. An accurate characterization of

Daily QA	
Test	Analysis Method
Safety and emergency (cameras, intercom, emergency buttons, O_2 sensor)	Visual
Mechanical QA (table, antenna and connector integrity, temperature, helium, water level)	Visual
ACR phantom with alternate daily coil setup (Monday-Friday)	QA Benchmark software
Image origin correspondence with LAP lasers (Sagittal localizer sequence on ACR)	Siemens clinical platform
Transmit gain setting (T1w SE sequence on ACR)	Siemens clinical platform
SNR stability (T1w SE sequence on ACR)	Siemens clinical platform

Table 1: MRI Daily Quality Assurance tests performed as part of a Radiation Therapy QA program.

Monthly QA	
Test	Analysis Method
Coil QA (for all regularly-used coils e.g. Body-18, Body-30, Head&Neck-20, UltraFlexLarge-18, Spine-32)	Siemens service platform
RF noise check	Siemens service platform
RF spike check	Siemens service platform
B_0 homogeneity phantom shim check	Siemens service platform / Siemens customer platform[1]
Helium level and cooling water flow rate	Siemens service platform
RF artifact check (based on the ACR image data of the month)	Visual
3D geometric distortion QA with gradient correction using 3DGRADE phantom (gre_ax_LR only)	Spectronics software
EPI average ghosting ratio check (on ACR phantom)	In-house python code
EPI geometric distortion check (on ACR phantom)	In-house python code
EPI long-term stability check (on ACR phantom)	In-house python code

Table 2: MRI Monthly Quality Assurance tests performed as part of a Radiation Therapy QA program.

[1]These QA tests are available on the Siemens Healthineers customer platform with MAGNETOM Sola and Vida scanners on *syngo* MR XA31 software and later versions, only. Otherwise, the tests are available on the Siemens Healthineers service platform.

Semi-Annual QA	
Test	Analysis Method
Gradient eddy-currents compensation/cross-term check	Siemens service platform
Gradient sensitivity check	Siemens service platform / Siemens customer platform[1]
Body coil tuning check	Siemens service platform
RF gain calibration check	Siemens service platform
Transmitter grain stability check	Siemens service platform
Slice position/thickness synthesizer check	Siemens service platform / Siemens customer platform[1]
LAP Lasers-on-marks verification (laser location is marked on the walls/ceiling around the room)	Visual
Table semi-annual test using Aquarius phantom	Siemens clinical platform

Table 3: MRI Semi-Annual Quality Assurance tests performed as part of a Radiation Therapy QA program.

Annual QA	
Test	Analysis Method
Coil QA (for all other coils not verified monthly, e.g. FlexSmall-4)	Siemens service platform
B_0 inhomogeneity check using dual-echo 3D GRE using the 25cm Siemens sphere of $NiS0_4$ solution	In-house python code
3D geometric distortion QA without gradient correction on 3DGRADE phantom (gre_ax_LR only)	Spectronics software
Parallel Imaging SNR verification on 3D MPRAGE for SRS (using ACR phantom)	In-house python code
B_0-field lines verification with Gauss meter incl. 5/200 Gauss	Visual
Mechanical table movement QA with ruler (5, 10, 20, 200, 350mm)	Visual
Secondary Systems check (incl. injector, anesthesia)	Visual
Oxygen sensor check	Visual
Electrical shutdown check	Siemens Technician
Table movement during emergency check	Siemens Technician
Quench button check	Siemens Technician

Table 4: MRI Annual Quality Assurance tests performed as part of a Radiation Therapy QA program.

the system-related effects is therefore of paramount importance for the correct use of MR images in RT. This is especially critical in the event that MR images are not fused to planning CT images, but used in a standalone fashion for MR-only RT planning. Therefore, geometric distortions were tested using the GRADE QA phantom (Spectronic Medical SE, Karbingatan, Sweden). The GRADE QA phantom consists of approximately 1200 17 mm diameter spherical markers made of polyethylene glycol imbedded in expanded foam [26]. The resulting phantom is of large diameter (47.9 cm lateral, 38.5 cm height and 50 cm longitudinal) and relatively light weight (approximately 10 kg). Note that the MAGNETOM Sola FOV is $50 \times 50 \times 50$ cm^3 while the MAGNETOM Aera FOV is slightly shorter in the longitudinal dimension and covers $50 \times 50 \times 45$ cm^3. It is important to note that a significant portion of the FOV, namely the area located under the imaging table, is a "dead zone" with respect to MR imaging. The width, height and length of the GRADE QA phantom ensures that a significant proportion (> 90%) of the usable scanner FOV can therefore be characterized for distortion. A 3D FLASH sequence was used to image the GRADE QA phantom as recommended [26]. The sequence parameters (*FLASH3D_geo*) are provided in Table 5. The phase encoding direction selected was the Left-Right (LR) direction.

The goal of this QA program is to ensure the best possible performance of RT MRI scanners, while optimizing or minimizing the QA time requirements. A significant effort was made to automate the data analysis as much as possible through the use of in-house or third-party software. Note also that QA data logging and storage is performed using QATrack+, an open source database for managing QA data [27]. Every test contains one or more measurement results that are uploaded in QAtrack+ and monitored over time.

CHU de Quebec in-house experience

For five of the quality assurance tests recommended by the AAPM reports, or the CPQR, no dedicated commercial software exists yet; therefore, we had to develop our own in-house python programs to perform an automatic analysis. The analysis of those five tests is described below:

EPI geometric distortions

For the EPI geometric distortion check (recommended in the AAPM Report 100 [20]), the same EPI pulse sequence is employed as for the ghosting ratio measurement and is shown in Table 5. An additional turbo spin echo (TSE) sequence with the same FOV, slice positions and acquisition/reconstruction matrix size (shown also in Table 5) is used as a geometric reference to measure the EPI distortion in both frequency-encode and phase-encode directions. The ITK Canny Edge Detection Filter was used to automatically detect the edges of both the TSE and the EPI image as shown in Figure 6 of the Results section. From the edge masks, the distances in the central row and column of the images are automatically subtracted, yielding a relative measure of distortion in the frequency and phase directions to an accuracy in the order of the image resolution (1 mm).

EPI ghosting ratio

The EPI average ghosting ratio is calculated using Eq. 1 within the central uniform slice of the ACR phantom. The main EPI sequence parameters used are listed in Table 5.

$$\%GR = \left| \frac{(S_L + S_R) - (S_T + S_B)}{2S_C} \right| \times 100\% \quad (1)$$

Here, S_L, S_R, S_T, S_B and S_C are the average signal in the left-side, right-side, top, bottom and central ROI locations shown in Figure 1, respectively. The ROIs are drawn manually for a first time as shown in Figure 1, and then saved as masks which can be re-used indefinitely to improve the consistency or reproducibility over time. A threshold of 3% was chosen as the acceptable upper limit for ghosting.

Sequence Name	α/TR/TE/TE$_2$	# Slices	FOV (freq×ph×sl)	Acq. Voxel Resolution	BW	TSE / EPI factor	Scan time
	°/ms/ms/ms		(mm)	(mm)	Hz/pix		(min:sec)
FLASH3D_geo	20/6.0/2.16/ –	480	500×500×480	0.98×0.98×1.0	330	– / –	24:36
EPI_ghost_geo	90/4860/61/ –	34	240×240×170	1.88×1.88×5.0	1260	– /128	0:6
TSE_ghost_geo	150/4860/59/ –	34	240×240×170	1.88×1.88×5.0	465	17/ –	1:24
EPI_stability	90/3370/40/ –	32	260×260×159	4.06×4.06×4.0	1202	– /64	8:30
FLASH3D_B$_0$	20/22/9.53/19.06	128	280×280×282	2.19×2.19×2.2	540	– / –	9:25

Table 5: Sequences with important parameters used in the QA program.

EPI long-term stability

The EPI long-term stability check was based on two previous publications, including the Glover stability QA protocol (GSQAP) [28] and the ROI analysis of Weisskoff [29]. Both analyses were performed on the same uniform ACR phantom slice of the *EPI_stability* sequence with parameters listed in Table 5.

B_0-inhomogeneity mapping

Although the B_0-homogeneity phantom shim check on the Siemens Healthineers service platform (Siemens customer platform[1] as of *syngo* MR XA31 for MAGNETOM Vida and MAGNETOM Sola) is run on a monthly basis (see monthly QA listed in Table 2), we also implemented a common B_0-inhomogeneity mapping technique described in both the AAPM report 284 [22] and the AAPM Report 100 [20]. Only the body-coil was used as receiver to avoid phase inconsistencies across various multi-channel head coils. The other alternative is to perform phase-unwrapping on each coil of a multi-coil array separately, but poses more challenges than benefits. The *unwrap phase* algorithm as part of the *skimage.restoration* python toolkit was found sufficiently robust to perform 3D phase-unwrapping on the 25 cm Siemens Healthineers spherical phantom images of a double-echo spoiled gradient echo sequence (*FLASH3D_B_0*) listed in Table 5. The following equation is employed to measure the final field inhomogeneity in ppm:

$$\text{(2)} \quad \Delta B_0[\text{ppm}] = \frac{\Delta\phi[\text{rad}]\ (42.576\ \frac{\text{MHz}}{\text{T}})}{\gamma[\frac{\text{MHz}}{\text{Ts}}]\ \Delta\text{TE}[\text{s}]\ f_0\ [\text{MHz}]} \times 10^6\ \text{ppm}$$

Here, $\Delta\phi = \phi_2 - \phi_1$ is the phase difference after unwrapping the phase ϕ_1, ϕ_2 corresponding to each echo TE_1, TE_2 with difference $\Delta TE = TE_2 - TE_1$, f_0 is the Larmor frequency (in MHz) of the scanner, and γ is the proton gyromagnetic ratio.

Parallel imaging SNR stability

The SNR verification of parallel imaging was performed using the image difference method (described in AAPM TG-118 [21]), via two 3D MPRAGE dynamics without acceleration (R = 1) and two with GRAPPA acceleration (R = 2), including 48 integrated *k*-space lines. The SNR ratios of R = 1 to R = 2 were then measured in five square ROIs inside the uniform slice of the ACR phantom image as shown in Figure 2. The 3D MPRAGE pulse sequence with iPAT = 2 was the same as our in-house protocol optimized for brain stereotactic radiosurgery planning (FOV: 240 × 240 × 176 mm³, Acquisition matrix: 384 × 384, axial slice thickness 1 mm, reconstruction matrix: 768 × 768 × 176, $TI/TR_{shot}/TR/TE/\alpha$ = 845/1670/8.16/3.31 ms/10°, iPAT = 2 with 48 integrated lines, BW = 160 Hz/pixel, RL phase-encode direction, scan time: 6 min).

Evaluation of parallel imaging

Siemens Healthineers GRAPPA parallel imaging method allows the possibility to use an integrated or separated method to acquire the reference lines. The separated method uses a gradient echo (GRE) sequence and allows the user to choose the number of reference lines in both phase directions (in plane and slice). The impact of the reference line acquisition scheme on SNR and time was evaluated using the sequence and methodology described in the parallel imaging SNR stability test. The MPRAGE sequence was used and the acquisition time was recorded for each acquisition. For the integrated method, the number of lines was varied from 24 to 96 lines while for the GRE method

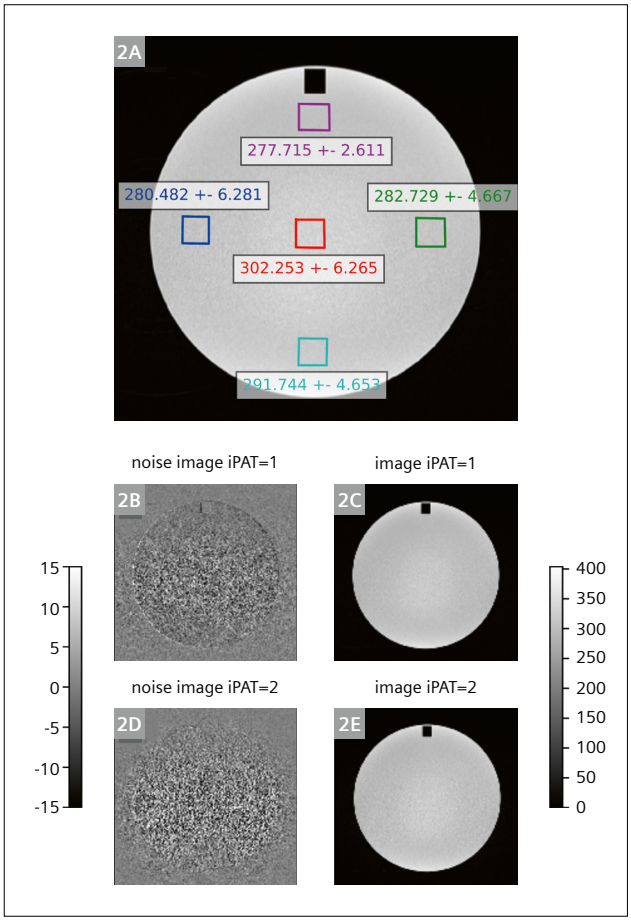

2 Parallel imaging SNR stability test showing **(2A)** ROI regions within the ACR phantom, **(2B)** noise image with iPAT = 1, **(2C)** image with iPAT = 1, **(2D)** noise image with iPAT = 2, **(2E)** image with iPAT = 2.

[1]These QA tests are available on the Siemens Healthineers customer platform with MAGNETOM Sola and Vida scanners on *syngo* MR XA31 software and later versions, only. Otherwise, the tests are available on the Siemens Healthineers service platform.

the following configurations were tested: 64 in-plane lines and 24 slice lines (gre 64-24) as well as 96 in-plane lines and 48 slice lines (gre 96-48).

Results

The complete AAPM TG 284, TG 100 and CPQR tests were performed as part of commissioning and no failures were detected on both MAGNETOM Aera and MAGNETOM Sola

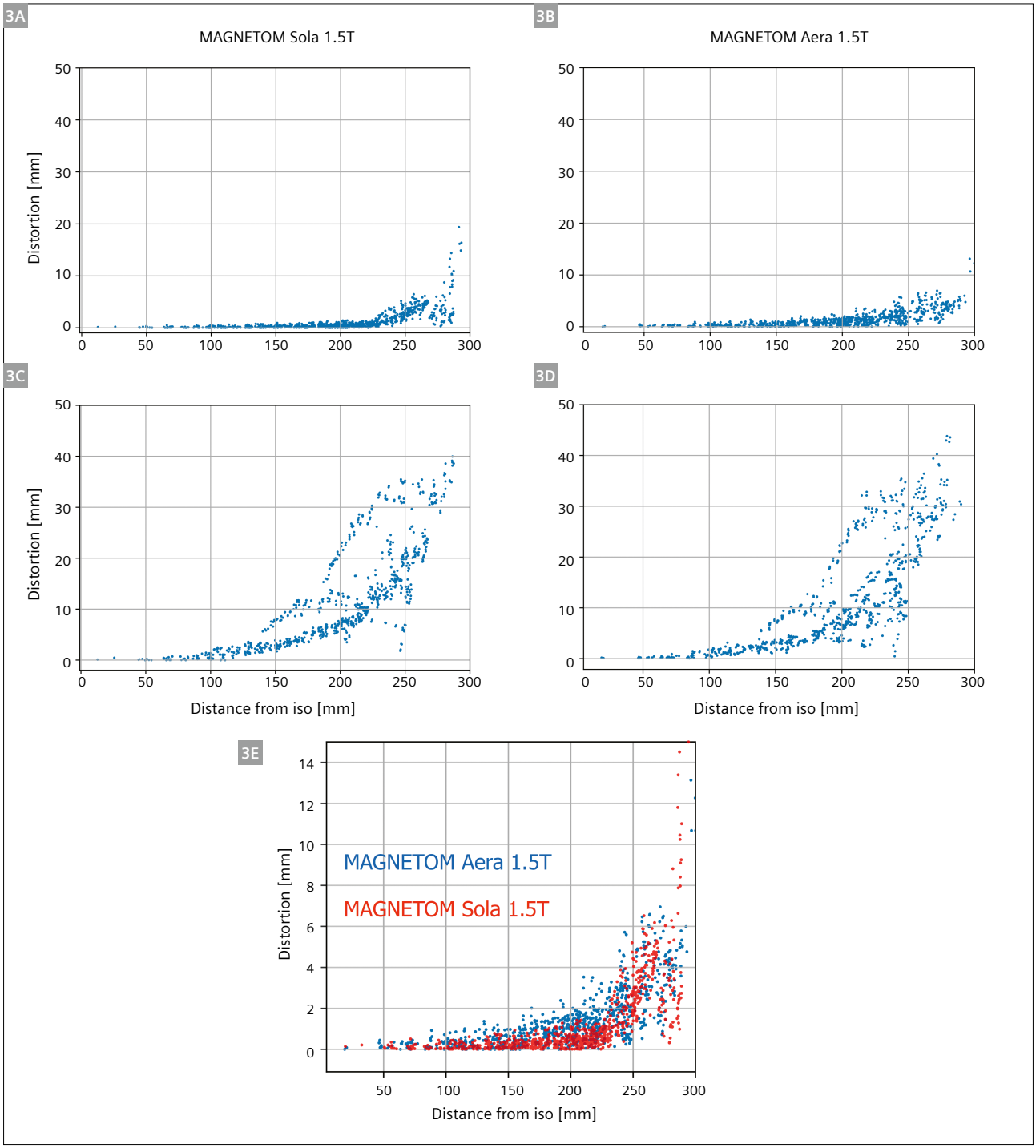

3 Comparison of Siemens Healthineers MAGNETOM Sola (3A, C) vs MAGNETOM Aera (3B, D) distortion vector magnitude plots with **(3A, B)** and without **(3C, D)** gradient non-linearity correction (using the 3D GRADE phantom by Spectronics) for the LR phase-encode direction as a function of control point distance from the MRI isocenter. **(3E)** The gradient-corrected control point's distortions of both scanners are superposed on the same axes demonstrating significantly lower mean distortions in the MAGNETOM Sola compared to the MAGNETOM Aera scanner.

4A

3D Distortions Summary for MAGNETOM Aera and Sola MRI Scanners in LR direction without gradient corrections

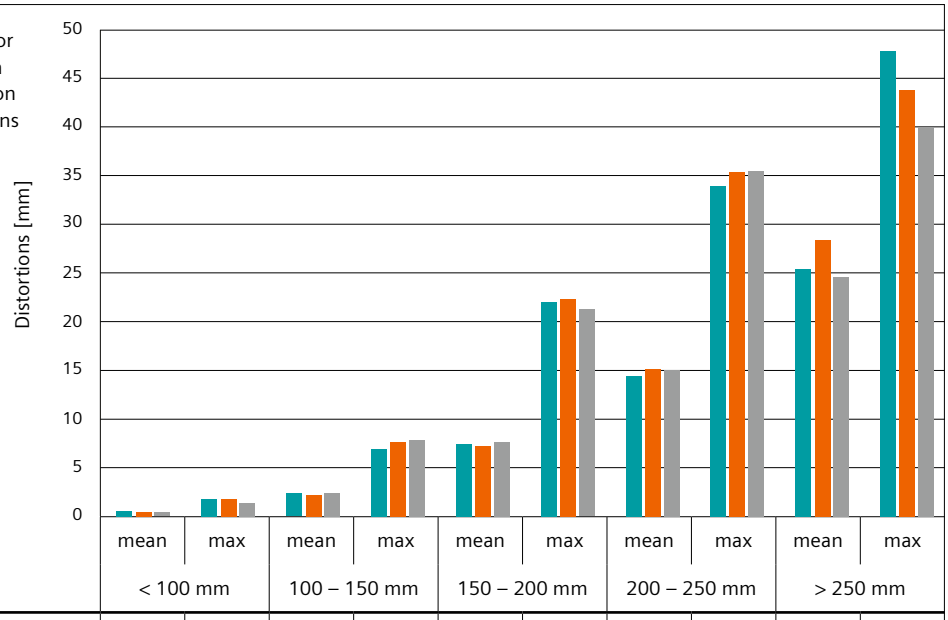

	mean	max	mean	max	mean	max	mean	max	mean	max
	< 100 mm		100 – 150 mm		150 – 200 mm		200 – 250 mm		> 250 mm	
MAGNETOM Aera Combi Dockable Table	0.51	1.80	2.34	6.95	7.48	21.98	14.44	33.95	25.48	47.81
MAGNETOM Aera Tim Dockable Table (standard)	0.48	1.77	2.25	7.67	7.22	22.30	15.15	35.41	28.36	43.81
MAGNETOM Sola BioMatrix Dockable Table (standard)	0.42	1.45	2.42	7.84	7.67	21.24	15.07	35.46	24.58	39.96
	Mean, standard and maximum distortions within specified radial distances from isocenter									

4B

3D Distortions Summary for MAGNETOM Aera and Sola MRI Scanners in LR direction with gradient corrections

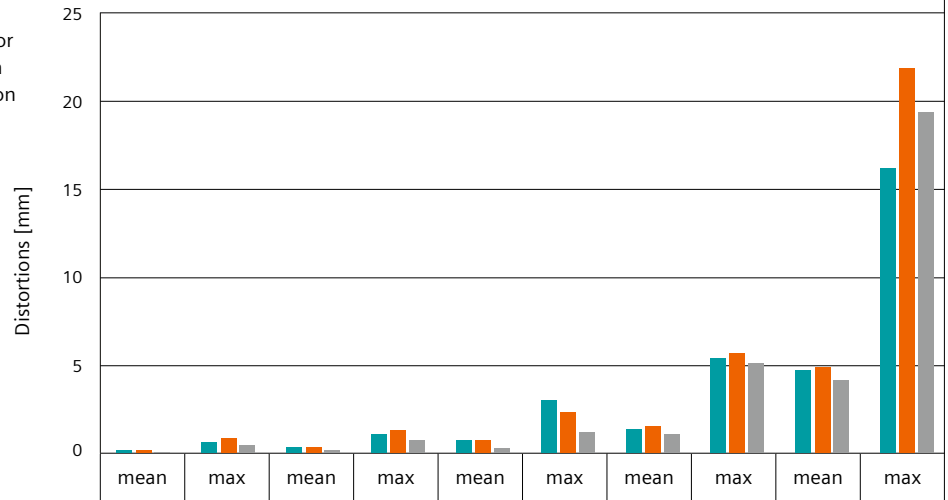

	mean	max	mean	max	mean	max	mean	max	mean	max
	< 100 mm		100 – 150 mm		150 – 200 mm		200 – 250 mm		> 250 mm	
MAGNETOM Aera Combi Dockable Table	0.21	0.70	0.37	1.12	0.77	3.05	1.45	5.42	4.78	16.23
MAGNETOM Aera Tim Dockable Table (standard)	0.22	0.92	0.38	1.36	0.79	2.38	1.59	5.71	4.90	21.83
MAGNETOM Sola BioMatrix Dockable Table (standard)	0.12	0.49	0.21	0.76	0.36	1.26	1.09	5.15	4.17	19.39
	Mean, standard and maximum distortions within specified radial distances from isocenter									

4 3D distortion mean and maximum values across spherical volumes of various radii from the imaging isocenter for the MAGNETOM Sola and MAGNETOM Aera scanners for the Left-Right (LR) phase encode direction without **(4A)** and with **(4B)** gradient corrections turned on for the standard and Combi Dockable Tables (MAGNETOM Aera only).

machines. One problem was found regarding coil QA; in fact SNR references were wrong for the Body-30 receiver coil and as a consequence the QA test kept failing; however this was corrected in version *syngo* MR XA31. Siemens Healthineers service platform allows for automatic QA processes (some QA processes are available on the Siemens Healthineers MAGNETOM World customer platform with MAGNETOM Sola and Vida scanners on *syngo* MR XA31 and later) which take less than an hour and these tests meet most of AAPM TG 284 and TG 100 recommendations. The service or customer QA platform allowed us to perform semi-automatic coil tests based on TG 284 recommendations. The time needed for testing depends on the coil itself (mainly dependant on the number of channels and length), but can range from 5 minutes to more than 20 minutes (e.g. spine-32 array or Body-30). Low-SAR RF pulses (the default setting in some sequences) were found to cause the ACR slice selection thickness test to fail with a value of 6.1 ± 0.2 mm, which was outside the tolerance of 5.0 ± 0.7 mm. The shim and gradient sensitivity had to be re-tuned during the first 9 months of operation for both machines, as well as Body Coil tuning for the MAGNETOM Sola. The shim-tuning was needed within the first 2 months post-commissioning and ramping up of the magnet.

Distortion characterization

Figure 3 presents the raw, uncorrected (3A, 3B) and 3D corrected (3C, 3D) distortion vector magnitude plots as a function of the distance from the MRI isocenter for the MAGNETOM Sola and MAGNETOM Aera platforms. Figure 3E compares the 3D distortion for the MAGNETOM Sola and MAGNETOM Aera with gradient corrections turned on. Panels 3A, 3C and 3B, 3D of Figure 3 illustrate that applying the vendor-supplied gradient correction mitigates, to a large extent, the residual 3D distortion. For a radius of 250 mm, the residual 3D distortion is 35 mm without gradient correction, which reduces to 5 mm with the 3D distortion correction applied. Panel 3E shows that there is a tendency for lower average residual distortion on the MAGNETOM Sola as compared to the MAGNETOM Aera.

Figure 4 presents the mean and maximum 3D distortion values for different radii spheres centered around the imaging isocenter for the MAGNETOM Sola and MAGNETOM Aera scanners. In fact, it first illustrates the large effect of turning the 3D gradient corrections "On". The main effect is a halving, or more, of the mean and maximum residual distortion across the scanner field-of-view. On the MAGNETOM Sola, the average distortion is on the order of 1 mm for imaging radii of 250 mm or less. For radii of up to 200 mm, the maximum distortion is 1.26 mm and the average is 0.36 mm. Distortion values on the MAGNETOM Aera standard table are roughly double the MAGNETOM Sola values for radii up to 200 mm. Distortion values for the Combi-Suite Dockable Table on the MAGNETOM Aera are comparable to values for the standard table.

B_0 inhomogeneity

Results of the B_0 inhomogeneity mapping in the 25 cm sphere for the MAGNETOM Aera and the MAGNETOM Sola 1.5T scanners are compared in Figure 5 in a sagittal slice. Note that the mean of the unwrapped phase (in 5C and 5D) can be close to any multiple of 2π, which explains the different intensities.

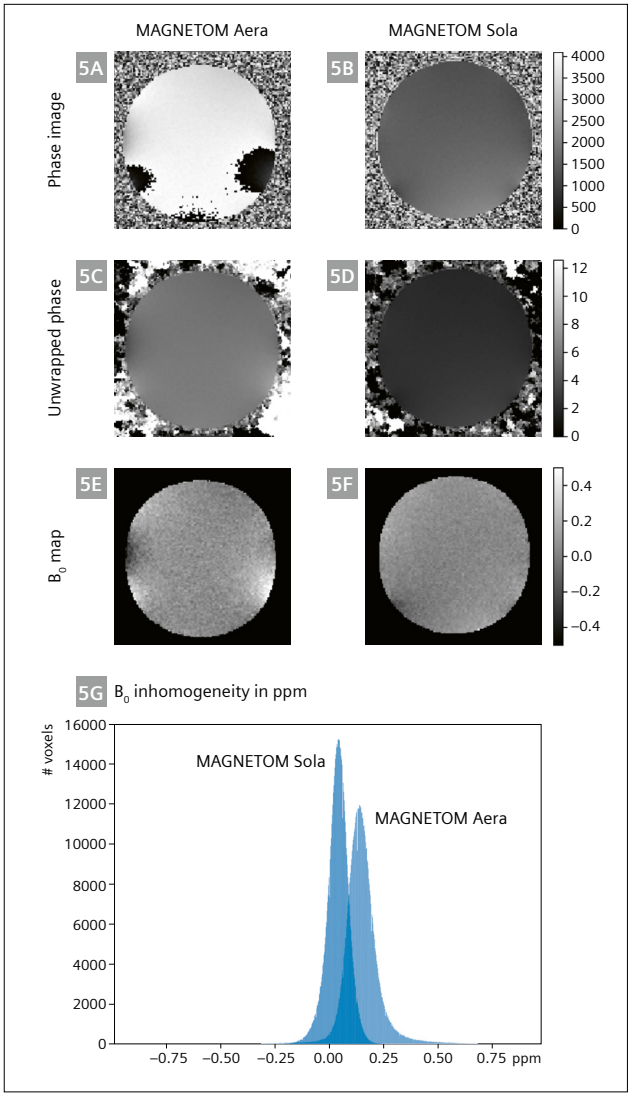

5 B_0 homogeneity test showing **(5A)** wrapped phase image, **(5C)** unwrapped phase image, **(5E)** B_0 inhomogeneity map in ppm for the MAGNETOM Aera system while **(5B)**, **(5D)** and **(5F)** are equivalent for the MAGNETOM Sola system. Sub-figure **(5G)** is showing the histogram of the inhomogeneity superposed for both systems.

Advanced imaging

Figure 6 shows some phantom images and edge detection results from our automated EPI geometric distortions measurement. The distortion in the phase encoding direction in (6B) is shown for both scanners over a period of about 6 months. The range of EPI distortion was between 0 and 2 mm for the MAGNETOM Sola system, while for the MAGNETOM Aera it was between 6 and 8 mm before the upgrade to *syngo* MRXA30 and in the same range as the MAGNETOM Sola after the upgrade. The average EPI ghosting ratio was (mean ± σ) 2.3 ± 0.2% and 1.3 ± 1.7% for the MAGNETOM Sola and MAGNETOM Aera scanners respectively. Example results of the EPI long-term stability test are shown in Figure 7 for the Glover Stability QA protocol, and in Figure 8 for the Weisskoff analysis. The mean percent drift was (mean ± σ) 0.10 ± 0.09% and 0.09 ± 0.05% while the mean percent fluctuation was (mean ± σ) 0.038 ± 0.005% and 0.033 ± 0.002% for the MAGNETOM Sola and MAGNETOM Aera scanners, respectively. In addition, the mean RDC was (mean ± σ) 11.8 ± 1.9 and 14.7 ± 0.8 for the MAGNETOM Sola and MAGNETOM Aera scanner, respectively.

The parallel imaging SNR ratio stability is plotted in Figure 9 over a period of approximately four months for the five ROI locations previously shown in Figure 2. The average SNR ratio over the five locations is close to 1.41 (√2). Figure 10 shows the impact of the number of reference lines and calibration method on the SNR with GRAPPA, including the imaging time to incorporate a metric of efficiency. The results are showing a significant improvement in SNR and efficiency with the integrated calibration in comparison with the gradient echo separated calibration. There was 17% decrease in SNR between 24 integrated lines and 64-24 gradient echo configuration. The SNR improved with the number of reference lines with approximately 37% difference between 96 and 24 integrated lines.

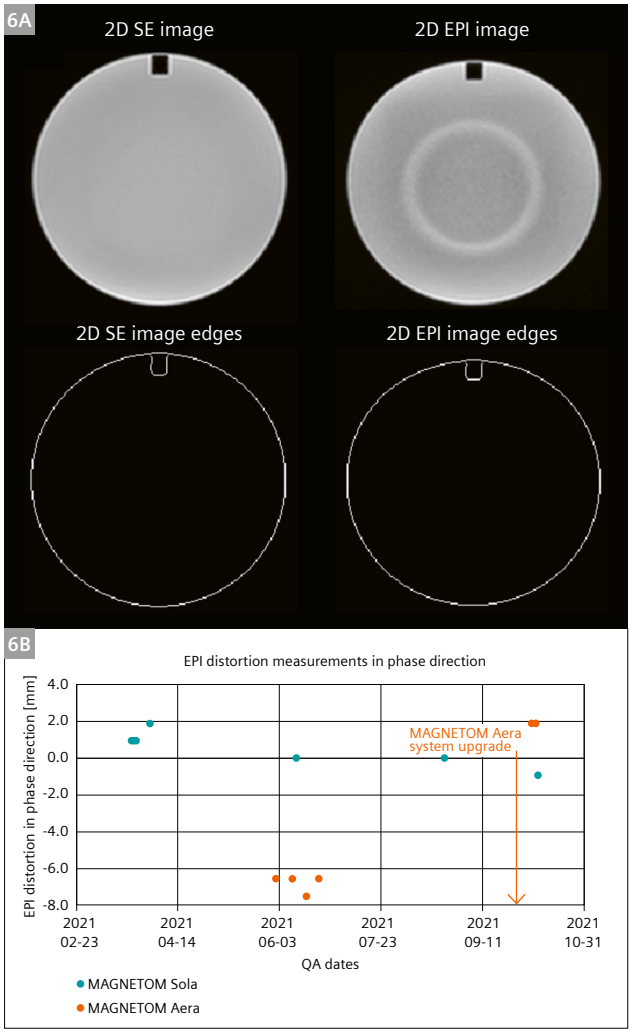

6 EPI distortion test showing **(6A)** the mask identified by the authors' analysis, **(6B)** EPI distortion data accumulated over 6 months for both MAGNETOM Sola and MAGNETOM Aera system.

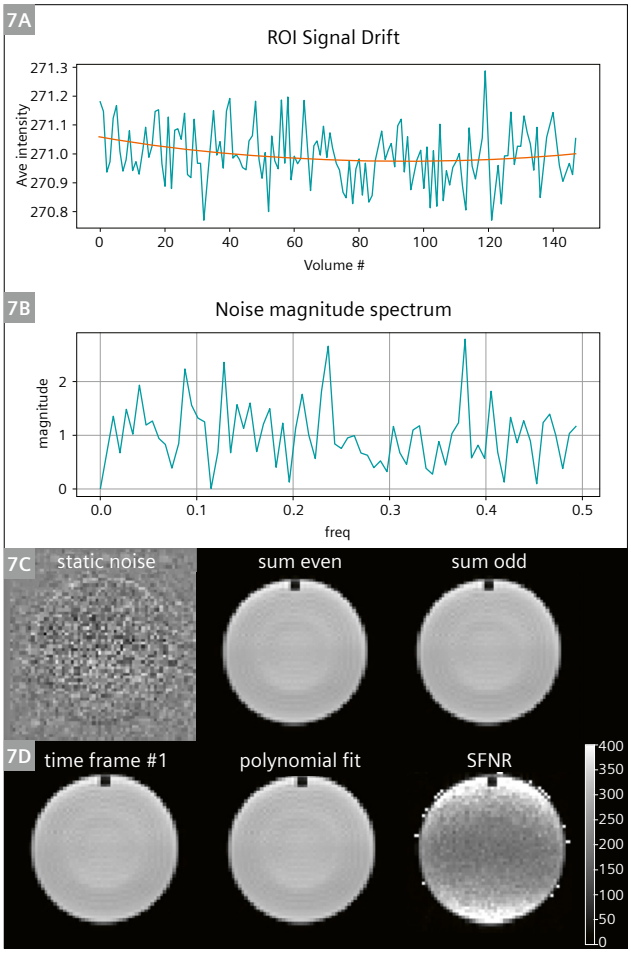

7 EPI stability test showing **(7A)** the signal drift over time (8 min 30 s), **(7B)** the noise magnitude spectrum from the accumulated data, **(7C)** the static noise as well as the even and odd data sum together, **(7D)** image of the first time-frame in combination with the corresponding polynomial fit of that data and the SFNR result.

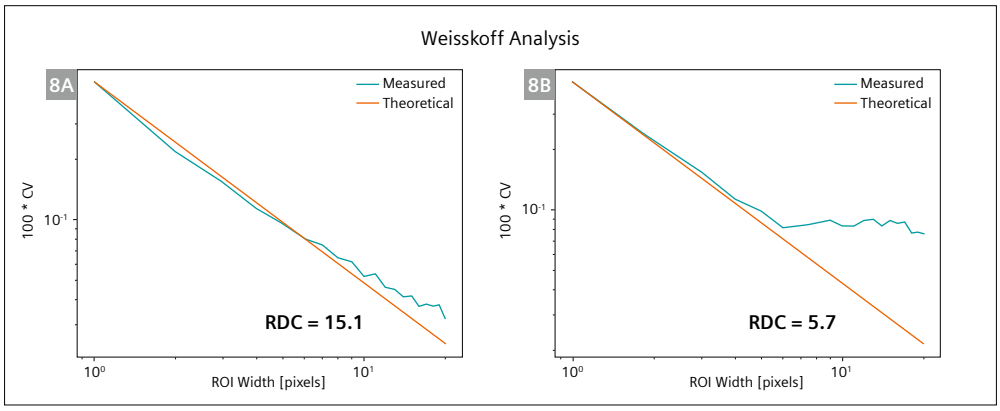

8 Weisskoff analysis of an **(8A)** acceptable and **(8B)** inacceptable result.

9A

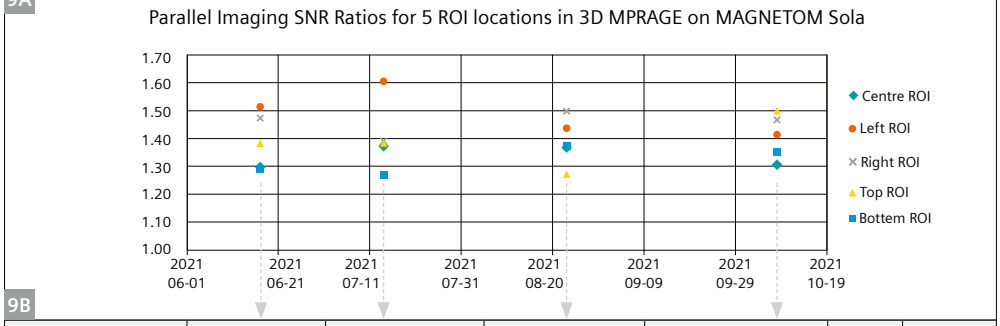

9B

Date	2021-06-17	2021-07-14	2021-08-23	2021-10-08	Mean	Std Dev
Centre SNR ratio	1.29	1.37	1.37	1.31	1.34	0.01
Left SNR ratio	1.51	1.60	1.44	1.41	1.49	0.09
Right SNR ratio	1.47	1.39	1.50	1.47	1.46	0.05
Top SNR ratio	1.38	1.38	1.27	1.50	1.39	0.09
Bottom SNR ratio	1.29	1.27	1.37	1.35	1.32	0.05

9 Parallel imaging stability test showing **(9A)** a plot of SNR for the five identified regions of Figure 2 over a period of approximately 4 months and **(9B)** the table showing the mean and standard deviation over the five different regions.

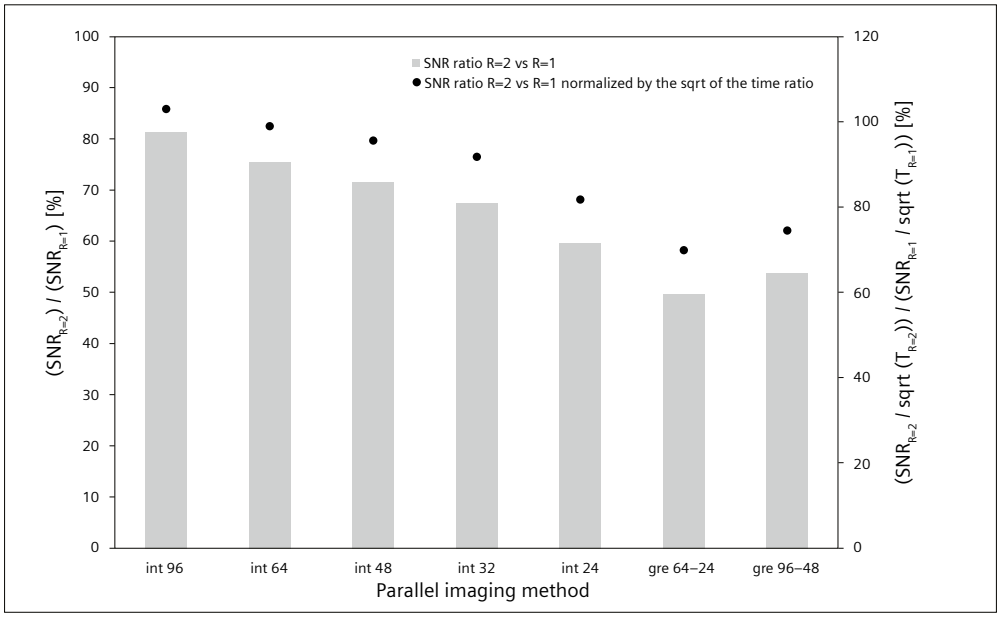

10 Impact of the number of reference lines and calibration method on the SNR with GRAPPA.

Discussion

The complete end-to-end testing required by the AAPM task group reports [20–22] were performed without major issues. Investigation of the Body-30 receiver coil QA test showed a problem with the SNR reference values in version *syngo* MR XA20, the issue was rapidly resolved by Siemens Healthineers in subsequent version *syngo* MR XA31. Baseline data acquired with the coil was used as the reference while waiting for the bug fix, since the problem was detected during acceptance testing. Although the issue was not identified as major, it demonstrates the importance of testing coils as part of the acceptance testing as suggested by the different recommendations. The Siemens Healthineers service and clinical platforms [24] allowed us to cover most of AAPM recommended tests in a timely manner and would fit in a busy clinic, operating the machine 24 hours per day, 7 days per week. In addition to ease of use, the Siemens Healthineers service platform makes it straightforward for the MRI physicist to directly address any failing test or scanner issue with the technical support. A special attention should be given to shimming, particularly within the first 2 months of the magnet ramp-up. The gradient sensitivity was also an important check in our experience, as both machines needed to have their laser-to-isocenter distance re-adjusted (i.e., the programmed table motion that automatically brings the patient or phantom to isocenter after zeroing on the scanner's laser, which depends on the gradient sensitivity). Quality assurance and technical support are important in order to prevent issues and reach optimal scanner performance. For radiotherapy purposes, low-SAR RF pulses should be avoided in order to prevent thicker slices than expected (potentially biasing the MR-CT registration through-slice accuracy). Service key level 7 is needed in order to maintain a detailed record of the different QA results, which are in turn needed to identify trends and avoid exceeding action thresholds over time. The *syngo* MR XA31 software version on the MAGNETOM Sola and MAGNETOM Vida now allows the user to perform Phantom shim check, Gradient sensitivity check and synthesizer check on the customer platform without logging into service mode.

The geometric distortion characterization, performed over 90% of the usable FOV, showed that the vendor-implemented 3D correction algorithm mitigates, to a large extent, the geometric distortions on a sizable portion of the FOV (at least up to a 20 cm radius). The 3D-corrected average distortion is less than 1 mm within a 10 cm radius and less than 2 mm within a 25 cm radius around the isocenter on both the MAGNETOM Aera (Combi Dockable or standard table) and MAGNETOM Sola scanners. These values are within the recommendation of the report 284 [22]. The measured distortion shows a clear downward trend on the MAGNETOM Sola compared to the MAGNETOM Aera; the average distortion on the MAGNETOM Sola is halved compared to the MAGNETOM Aera for radii of up to 20 cm and 50% less than the MAGNETOM Aera for radii of up to 25 cm. These values can be used as an estimate for the magnitude of system-related distortion on both the MAGNETOM Sola and MAGNETOM Aera platforms. Using a different distortion evaluation method may impact the results depending on the phantom field of view, number of data points and analysis method; however the repeatability and set-up sensitivity of the current method was validated in a previous study [26].

The superior B_0 homogeneity of the MAGNETOM Sola in comparison to the MAGNETOM Aera is clearly visible in Figure 5E and 5F and is confirmed by the histogram of the entire images in 5G. There is a significant difference between the histogram centers of approximately 0.1 ppm. In order to ensure a fair comparison, the same standard shimming routine was used on both systems. Therefore, the narrower full width at half maximum of the ΔB_0 histogram for the MAGNETOM Sola scanner is due to the superior intrinsic homogeneity of this magnet.

The EPI distortions on the MAGNETOM Aera scanner were reduced from 6.5 mm following the system installation with *syngo* MR E11E software to 2 mm after a system software upgrade (to version *syngo* MR XA30), which enabled using the exact same EPI sequence as on the MAGNETOM Sola scanner for comparison (version *syngo* MR XA20). The ACR phantom needs to be periodically refilled in order to avoid air bubbles at the surface (especially in the uniform slice of interest), as it could significantly increase the geometrical distortions locally, which could be responsible in part for the improvement seen after the upgrade. The ghosting ratio test is sensitive to the receiver coil arrangement and the image intensity correction filter. In fact, the intensity correction filter was found to be responsible for increasing the noise floor around the image as visible on the left-side/right-side of the phantom in Figure 1, consequently exaggerating the ghost ratio. Therefore, we deemed that either a moderate or no intensity correction is preferable for this QA test.

As demonstrated in Figure 7A the mean signal drift can be very minor on the Siemens Healthineers scanners tested in the current study and we did not observe a consistent tendency towards a positive drift as had been claimed previously [28]. Rather, the drift was occasionally positive and negative. The mean drifts reported in the current study for the MAGNETOM Sola and MAGNETOM Aera are significantly lower than those reported by Glover et al.

(0.3% at the lowest) [28], suggesting an interesting improvement in hardware stability since the early 2000s. The difference in average RDC is again attributed to different software versions (before the MAGNETOM Aera was upgraded to *syngo* MR XA30). Figure 8 shows a typical RDC in 8A and an abnormally low value in 8B. Glover et al. explain that a low RDC is often associated with a non-stationary and irregular time course of the residuals (after polynomial fit of the 150 dynamics).

In the parallel imaging stability test, an average SNR ratio over the five locations was found to be close to 1.41 (= $\sqrt{2}$), which is what one would expect in the case of a geometry factor (*g* factor) of 1. Normally, the geometry factor is greater than unity, but if a regularization is employed in the parallel imaging reconstruction, values below unity are possible [30, 31]. However, a desirable amount of regularization should approach a *g* factor of ~1, which can be assumed when making SNR predictions on 3D MRI protocols with varying factors of acceleration [32]. In GRAPPA parallel imaging, the calibration method was shown to directly impact the SNR. In fact, the integrated method was shown to be significantly better in term of SNR with no significant difference in scan time compared to the GRE method. The SNR increases with the number of reference lines. A previous study recommended a minimum of 32 integrated lines to be used with GRAPPA [33]. The current study is in agreement with Blaimer et al. [33] and further suggests that 48 integrated lines better preserves SNR efficiency since the acquisition time is minimally impacted. High-resolution imaging is needed for radiotherapy planning, making it more difficult to preserve sufficient SNR in an acceptable scan time; therefore we recommend using 48 integrated lines with GRAPPA for these sequences.

Conclusion

The authors' experience showed no major problem during acceptance and commissioning. The Siemens Healthineers service platform was useful and time-saving in permitting medical physicists to perform most of the QA program in a semi-automatic or automatic fashion and in a clinically-acceptable time. The MAGNETOM Sola system was found to be more geometrically precise and accurate, with a more homogenous B_0 field making it suited for external-beam RT planning. Additional in-house tests allowed to track more advanced features and detected software upgrade changes. GRAPPA parallel imaging reference lines and calibration methods were optimized in order to obtain a sufficient SNR in a clinically-acceptable scan time for radiation therapy simulation.

References

1 Khoo VS, Joon DL. New developments in MRI for target volume delineation in radiotherapy. Br J Radiol 2006;79:S2–15.
2 Whitfield GA, Kennedy SR, Djoukhadar IK, Jackson A. Imaging and target volume delineation in glioma. Clin Oncol R Coll Radiol G B 2014;26:364–76.
3 Schmidt MA, Payne GS. Radiotherapy planning using MRI. Phys Med Biol 2015;60:R323–61.
4 Haie-Meder C, Pötter R, Van Limbergen E, Briot E, De Brabandere M, Dimopoulos J, et al. Recommendations from Gynaecological (GYN) GEC-ESTRO Working Group (I): concepts and terms in 3D image based 3D treatment planning in cervix cancer brachytherapy with emphasis on MRI assessment of GTV and CTV. Radiother Oncol 2005;74:235–45.
5 Steenbakkers RJHM, Deurloo KEI, Nowak PJCM, Lebesque JV, van Herk M, Rasch CRN. Reduction of dose delivered to the rectum and bulb of the penis using MRI delineation for radiotherapy of the prostate. Int J Radiat Oncol Biol Phys 2003;57:1269–79.
6 Pötter R, Dimopoulos J, Georg P, Lang S, Waldhäusl C, Wachter-Gerstner N, et al. Clinical impact of MRI assisted dose volume adaptation and dose escalation in brachytherapy of locally advanced cervix cancer. Radiother Oncol 2007;83:148–55.
7 Owrangi AM, Greer PB, Glide-Hurst CK. MRI-only treatment planning: benefits and challenges. Phys Med Biol 2018;63:05TR01.
8 Bauman G, Haider M, Van der Heide UA, Ménard C. Boosting imaging defined dominant prostatic tumors: A systematic review. Radiother Oncol 2013;107:274–81.
9 Monninkhof EM, Loon JWL van, Vulpen M van, Kerkmeijer LGW, Pos FJ, Haustermans K, et al. Standard whole prostate gland radiotherapy with and without lesion boost in prostate cancer: Toxicity in the FLAME randomized controlled trial. Radiother Oncol 2018;127:74–80.
10 Ulin K, Urie MM, Cherlow JM. Results of a multi-institutional benchmark test for cranial CT/MR image registration. Int J Radiat Oncol Biol Phys 2010;77:1584–9.
11 Korsager AS, Carl J, Riis Østergaard L. Comparison of manual and automatic MR-CT registration for radiotherapy of prostate cancer. J Appl Clin Med Phys 2016;17:294–303.
12 Brock KK, Deformable Registration Accuracy Consortium. Results of a multi-institution deformable registration accuracy study (MIDRAS). Int J Radiat Oncol Biol Phys 2010;76:583–96.
13 Pappas EP, Alshanqity M, Moutsatsos A, Lababidi H, Alsafi K, Georgiou K, et al. MRI-Related Geometric Distortions in Stereotactic Radiotherapy Treatment Planning: Evaluation and Dosimetric Impact. Technol Cancer Res Treat 2017;16:1120–9.
14 NessAiver M. Range of Results from over 534 ACR-mandated Annual MRI Performance Evaluations on over 204 Magnets from 8 Vendors Spanning a 10-year Period 2011. http://www.simplyphysics.com/MRI%20QA%20RSNA%202011.pdf (accessed September 21, 2021).
15 Weygand J, Fuller CD, Ibbott GS, Mohamed ASR, Ding Y, Yang J, et al. Spatial Precision in Magnetic Resonance Imaging–Guided Radiation Therapy: The Role of Geometric Distortion. Int J Radiat Oncol 2016;95:1304–16.
16 Poggi S, Pallotta S, Russo S, Gallina P, Torresin A, Bucciolini M. Neuronavigation accuracy dependence on CT and MR imaging parameters: a phantom-based study. Phys Med Biol 2003;48:2199–216.
17 Paulson ES, Erickson B, Schultz C, Allen Li X. Comprehensive MRI simulation methodology using a dedicated MRI scanner in radiation oncology for external beam radiation treatment planning. Med Phys 2015;42:28–39.

18 Price R, Allison J, Clarke G, Dennis M, Hendrick RE, Keener C, et al. 2015 Magnetic Resonance Imaging QUALITY CONTROL MANUAL 2015:126.
19 Glide-Hurst CK, Paulson ES, McGee K, Tyagi N, Hu Y, Balter J, et al. Task Group 284 Report: Magnetic Resonance Imaging Simulation in Radiotherapy: Considerations for Clinical Implementation, Optimization, and Quality Assurance. Med Phys n.d.;n/a.
20 Jackson E, Bronskill M, Drost D, Och J, Pooley R, Sobol W, et al. Acceptance Testing and Quality Assurance Procedures for Magnetic Resonance Imaging Facilities. AAPM; 2010.
21 Yanasak N, Clarke G, Stafford RJ, Goerner F, Steckner M, Bercha I, et al. Parallel Imaging in MRI: Technology, Applications, and Quality Control. AAPM; 2015.
22 Glide-Hurst CK, Paulson ES, McGee K, Tyagi N, Hu Y, Balter J, et al. Task group 284 report: magnetic resonance imaging simulation in radiotherapy: considerations for clinical implementation, optimization, and quality assurance. Med Phys 2021;48:e636–70.
23 Zhang B, Stanescu T, Wachowicz K, King J, Côté J-C. Canadian Partnership for Quality Radiotherapy Technical Quality Control Guidelines for Magnetic Resonance Imaging for Radiation Treatment Planning 2020. https://www.cpqr.ca/wp-content/uploads/2020/09/MRI-2020-09-01_FR.pdf (accessed November 30, 2021).
24 Siemens Healthineers. Commissioning and Quality Assurance (QA) for MAGNETOM systems in radiation therapy n.d. https://cdn0.scrvt.com/39b415fb07de4d9656c7b516d8e2d907/73afee707dbc96c2/8490b30ac680/MR_Quality_Assurance_Guide_for_MR_in_RT_FINAL.pdf (accessed November 11, 2021).
25 Gustafsson C, Nordström F, Persson E, Brynolfsson J, Olsson LE. Assessment of dosimetric impact of system specific geometric distortion in an MRI only based radiotherapy workflow for prostate. Phys Med Biol 2017;62:2976–89.
26 Wyatt J, Hedley S, Johnstone E, Speight R, Kelly C, Henry A, et al. Evaluating the repeatability and set-up sensitivity of a large field of view distortion phantom and software for magnetic resonance-only radiotherapy. Phys Imaging Radiat Oncol 2018;6:31–8.
27 Angers C, Bottema R, Buckley L, Studinski R, Petzold D, Abbassian F, et al. Streamlining Regulatory Activities Within Radiation Therapy Departments Using QATrack+. Health Phys 2019;117:306–312.
28 Friedman L, Glover GH. Report on a multicenter fMRI quality assurance protocol. J Magn Reson Imaging 2006;23:827–39.
29 Weisskoff RM. Simple measurement of scanner stability for functional NMR imaging of activation in the brain. Magn Reson Med 1996;36:643–5.
30 Lin F-H. Prior-Regularized GRAPPA Reconstruction. Proc Intl Soc Magn Reson Med 2006;14:3656.
31 Lin F-H, Kwong KK, Belliveau JW, Wald LL. Parallel imaging reconstruction using automatic regularization. Magn Reson Med 2004;51:559–67.
32 Jutras J-D, Wachowicz K, Gilbert G, De Zanche N. SNR efficiency of combined bipolar gradient echoes: Comparison of three-dimensional FLASH, MPRAGE, and multiparameter mapping with VFA-FLASH and MP2RAGE. Magn Reson Med 2017;77:2186–202.
33 Blaimer M, Breuer FA, Mueller M, Seiberlich N, Ebel D, Heidemann RM, et al. 2D-GRAPPA-operator for faster 3D parallel MRI. Magn Reson Med 2006;56:1359–64.

Contact

Professeur associé Éric Poulin
Département de radio-oncologie et
Axe Oncologie du Centre de recherche
du CHU de Québec
CHU de Québec-Université Laval
Centre intégré de cancérologie
2250, boulevard Henri-Bourassa
Québec, QC, G1G 5X1
Canada
Eric.poulin@chudequebec.ca

The Integration of MRI in Radiation Therapy:

The Power of Multidisciplinary Collaboration

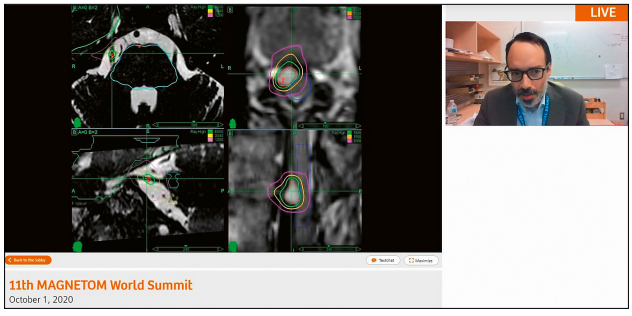

Implementing a Magnet Dedicated to Planning Radiotherapy Treatments

David Roberge
Centre Hospitalier de l'Université de Montréal, Canada

Don't miss the talks delivered by experienced and renowned experts at the MAGNETOM World Summit

www.siemens-healthineers.com/MWS2020-recordings

PETRA Sequence for Catheter Detection in Interstitial High-Dose-Rate (HDR) Brachytherapy

Evangelia Kaza, Ph.D.; Ivan Buzurovic, Ph.D.

Brigham and Women's Hospital, Dana-Farber Cancer Institute, Harvard Medical School, Boston, MA, USA

Introduction

In high-dose-rate (HDR) interstitial brachytherapy treatment planning, determining the dwell positions of radioactive sources relies on accurate localization of the implanted catheters. Currently, catheters are detected in-situ using CT, followed by T2-weighted MRI for target and organs at risk (OARs) delineation. Possible changes in organ or catheter position between the two scans can lead to registration errors in the MR-CT image fusion and affect estimated dose [1]. Brachytherapy dose calculations are performed assuming water as the medium [2], unlike external beam radiotherapy applications which require tissue-related Hounsfield units obtained from CT. Therefore, brachytherapy treatment planning could be performed using MRI only, if it could detect brachytherapy devices with acceptable spatial accuracy. However, brachytherapy applicators, templates, and catheters present no signal on standard MR images, and are thus difficult to discern from surrounding air, vessels, or low signal intensity tissues. Approaches to visualize interstitial catheters include insertion of markers [3] which incur additional costs, or investigational post-processing software to take advantage of magnetic susceptibility differences between metal or air and tissues [4].

Our goal was to detect empty interstitial needles and templates for HDR brachytherapy directly on clinical MR images obtained on a 3T MAGNETOM Vida scanner (Siemens Healthcare, Erlangen, Germany) used for radiotherapy simulations. An FDA approved "pointwise encoding time reduction with radial acquisition" (PETRA) sequence was selected and optimized for this purpose. As a zero TE (ZTE) sequence variant able to image tissues with T2 < 1 ms [5], PETRA was promising for visualizing synthetic polymers whose transverse relaxation times in the order of µs–ms cannot be captured by the longer echo times employed by most clinical sequences. PETRA can provide submillimetre isotropic resolution and is robust to motion artifacts owing to its mainly radial acquisition scheme. Moreover, its 3D properties allow for accurate reconstruction in all 3 orientations, which is important for treatment planning.

Methods

Phantom

Detectability of empty interstitial needles on PETRA images and their positional agreement with CT was investigated using a poultry phantom. A plastic obturator attached to a Syed-Neblett interstitial template (Best Medical International, Springfield, VA, USA) with six ProGuide Sharp Needles 6Fx294mm (Elekta Brachytherapy, Stockholm, Sweden) in the obturator slots was introduced into the giblet filled cavity of a cleaned turkey. Three additional needles were inserted in the turkey breast through the template. The poultry phantom with empty catheters was scanned in the 3T MAGNETOM Vida using a coronal 3D PETRA (TR/TE 3.32/0.07 ms; FOV 300 mm^3 isotropic; voxel size 0.85 mm^3 isotropic; flip angle 6°; bandwidth 400 Hz/px; 100000 radial views; acquisition time 5 min 46 s), and subsequently CT imaged. PETRA MR and CT images were fused by applying a rigid body registration. The coordinates of interstitial catheters on the CT and on the co-registered MR images were extracted for each slice location, and their Euclidean distance was calculated. The mean, median and standard deviation of this metric over all slices were computed as global measures of MR-CT distance for each catheter.

Patients

The feasibility of PETRA's clinical implementation for interstitial needle and template detection was assessed on five gynaecological brachytherapy patients. Anesthetized patients were implanted under ultrasound guidance with a Syed-Neblett interstitial template and ProGuide Sharp Needles in the HDR suite. The catheters were filled with copper strands and patients were imaged on a helical CT. After marker removal, patients were transferred on a BioMatrix Dockable Table and transported to the MR suite, where they were scanned using a bottom BioMatrix Spine 32 coil and a top Body 18 Long coil. Axial T2-weighted 3D SPACE images (TR/TE 1800/167 ms; FOV 288 × 288; voxel size 1.04 mm^3 isotropic; flip angle 120°; bandwidth 668 Hz/px; acquisition time 11 min 11 s) were acquired for lesion and OAR contouring. Axial 3D PETRA images

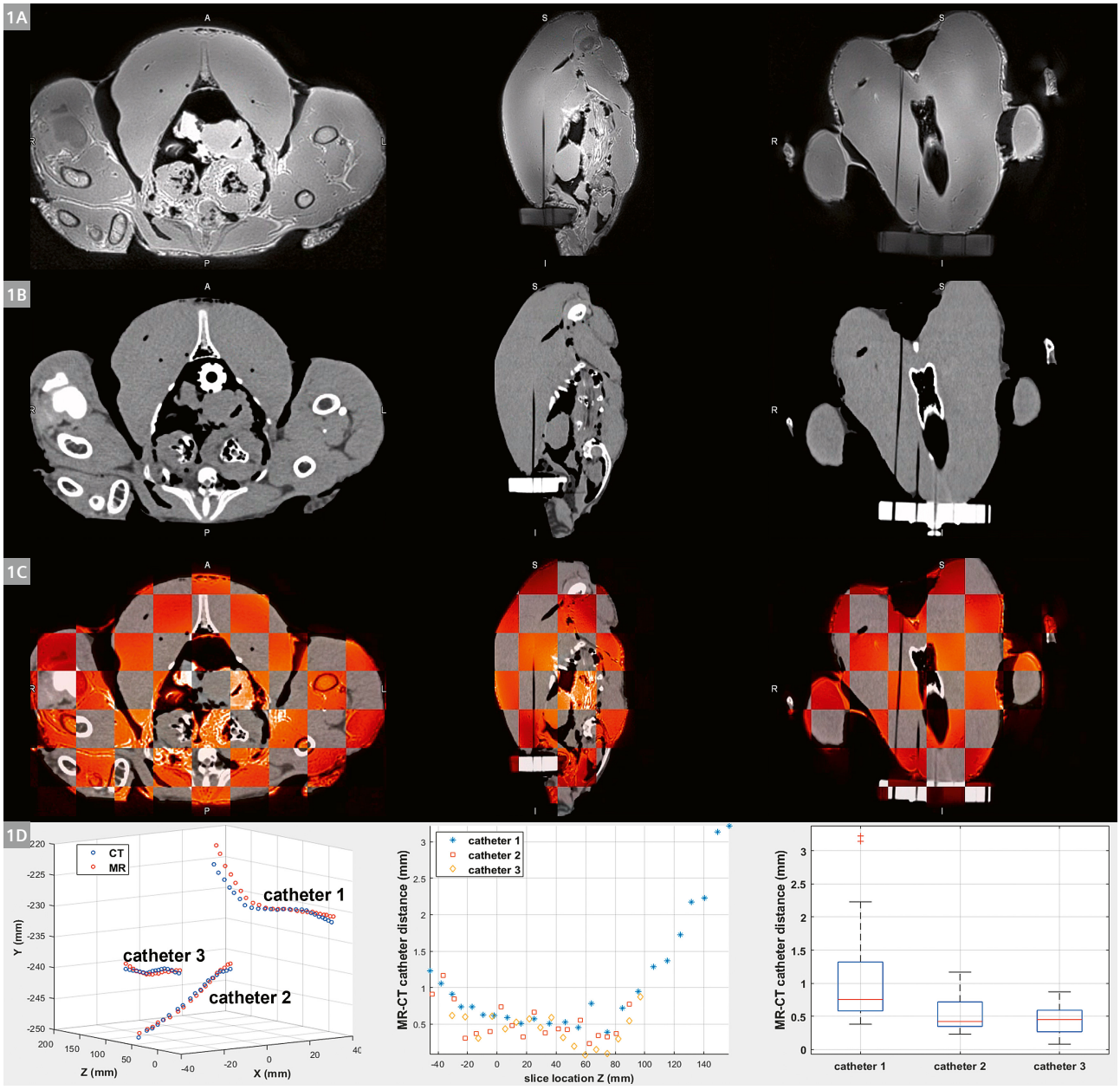

1 **(1A)** PETRA, **(1B)** CT images of a poultry phantom in axial, sagittal, and coronal orientation. Three empty plastic catheters penetrating the turkey breast through an interstitial template were detected with negative contrast. **(1C)** Checkerboard view of the PETRA (red) and CT images (grey) fusion in the three planes. **(1D)** Left: 3D plot of the CT (blue) and PETRA MR (red) coordinates of the points used to track the three interstitial catheters. X: right-left, Y: anterior-posterior, Z: superior-inferior axis. Catheter numbers increased from left to right on the phantom images. Middle: distance between CT and MR point contour coordinates over their common slice locations Z for each catheter. Right: Boxplots of MR-CT point distances for each catheter. Red lines: median; whiskers: minimum and maximum measurement; red crosses: outliers. *Reprinted with permission from [7].*

(TR/TE 3.32/0.07 ms; FOV 416 mm³ isotropic; voxel size 0.90 mm³ isotropic; flip angle 4°; bandwidth 401 Hz/px; 100000 radial views; acquisition time 5 min 55 s) were acquired to investigate needle detectability. Feasibility assessments of tracking empty interstitial catheters on PETRA images and of producing treatment plans using the MR scans only were performed in a treatment planning system (TPS).

Results

Phantom

PETRA detected the empty interstitial needles with negative contrast and the template with intermediate contrast relative to the turkey tissue (Fig. 1A). The plastic obturator and catheter sections outside the poultry flesh were not visualized. PETRA-CT fusion showed very good positional agreement of turkey features and interstitial catheters between the two modalities (Fig. 1C). For all three catheters, the distance of their tracked points on PETRA and CT images was < 1 mm for slice locations between -30 and 100 mm (Fig. 1D). The leftmost catheter 1 with a longer interstitial section presented increasing MR-CT catheter distance for slice locations > 100 mm. Median MR-CT catheter distance was < 1 mm for all catheters, while average distance amounted to 1.12 ± 0.81 mm (mean ± standard deviation) for catheter 1 due to increasing divergence of PETRA and CT catheter positions for slices further from isocenter.

Patients

Figure 2 shows matching CT and MR slices of an example patient. Using PETRA, all empty interstitial catheters could be identified with opposite signal than the marker-filled catheters on CT. In general, catheter locations agreed between MR and CT, considering slight variations in patient position between the two examinations. Nevertheless, organ and needle positions matched better between the

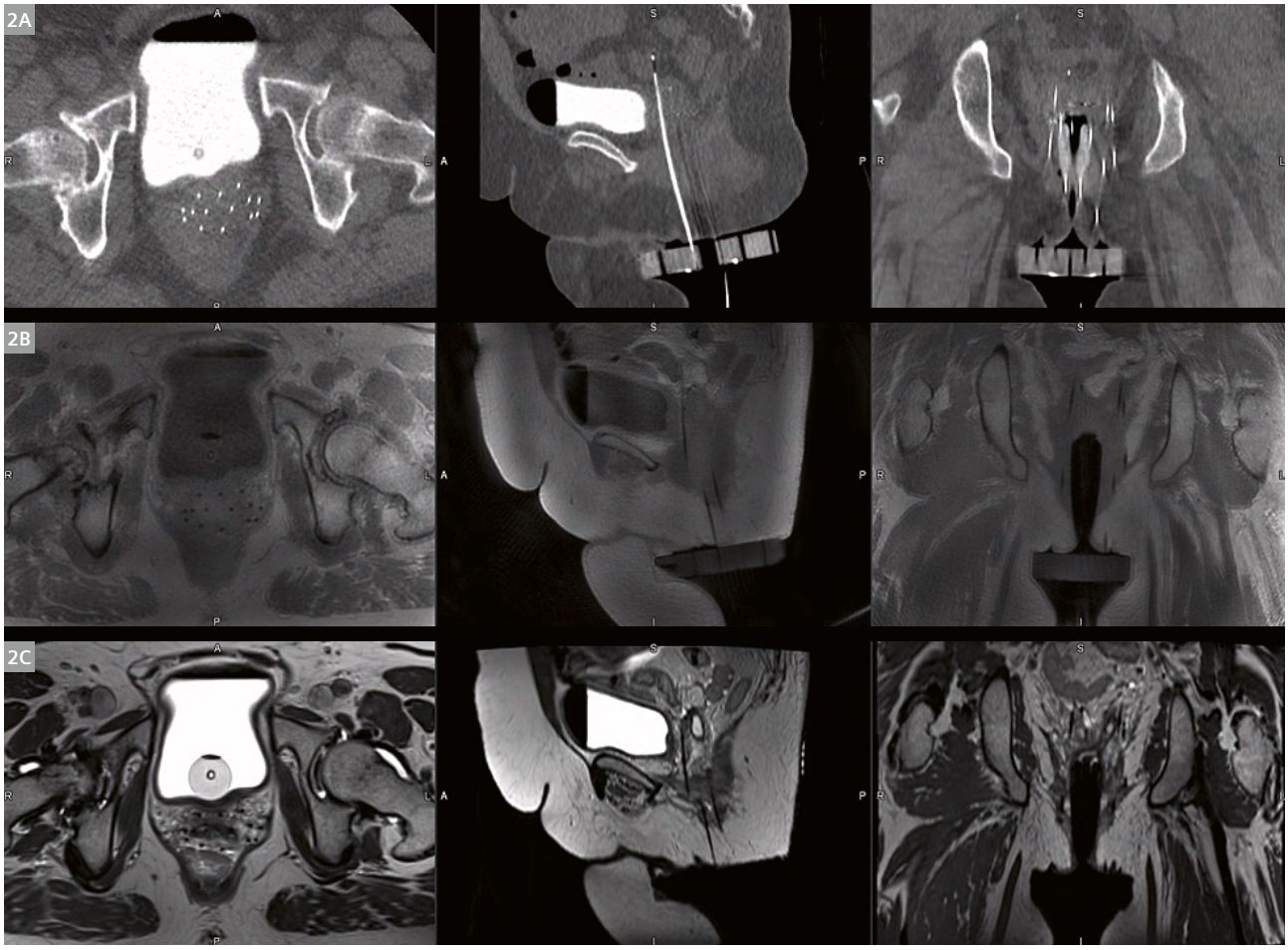

2 Axial (left), sagittal (middle) and coronal (right) images of an endometrial adenocarcinoma patient with 14 interstitial needles perforating a Syed-Neblett template. **(2A)** CT, with copper-filled catheters appearing bright. **(2B)** PETRA with empty catheters detectable by their lack of signal inside tissue, and visible template. **(2C)** SPACE with obscured template, and dark empty catheters more ambiguously differentiated from low signal intensity tissues.

MR datasets which were acquired immediately after each other in the same session. While catheters appeared hypointense on both PETRA and SPACE images, PETRA provided higher spatial resolution and a lower range of overall image contrast than SPACE, which facilitated catheter differentiation from surrounding tissues. The obturator was not visualized on either MR scan, but the interstitial template was well distinguished from the background air on PETRA, contrary to SPACE. Thanks to template visualization on PETRA, interstitial catheters could be followed to their entry hole on the template, allowing for individual catheter identification (Fig. 3A). All empty needles could be tracked on PETRA images using a TPS. Treatment plans could be produced by combining catheter tracking information from PETRA with organ and lesion contours obtained from SPACE (Fig. 3B).

Discussion

Initial PETRA images of a poultry phantom revealed the potential to detect empty interstitial needles with negative contrast, and a clinically acceptable [6] sub-millimetre accuracy compared to CT within 10 cm from scanner isocenter. Increasing disagreement with distance from isocenter may be due to geometric distortions caused by residual gradient non-linearities [7] or to registration errors during fusion. Utilization of a phantom for assessing spatial agreement of PETRA and CT eliminated uncertainties introduced by possible patient position mismatch in clinical scenarios.

Observations for interstitial template and catheter visualization on PETRA images of gynaecological brachytherapy patients were similar as for the phantom. The minimal echo time allowed capturing MR signal from the plastic template but not from the obturator which is made from a different material. The employed low flip angle resulted in a short range of tissue intensities, providing more consistent tissue-catheter contrast than the T2-weighted SPACE, where parts of the lesion also appeared hypointense. This fact, combined with PETRA's high spatial resolution and lower susceptibility-induced distortions than T2-weighted imaging [7] made catheter detection more accurate on PETRA than on SPACE. The additional advantage of determining catheter entry holes on the template allowed for catheter identification. Since a TPS could trace all catheters on PETRA, treatment plans could be produced by fusing SPACE images for treatment contour delineation with the spatially matching PETRA images for needle detection. These plans were comparable to those obtained using the standard CT-based catheter tracking [7], presenting PETRA's potential to replace CT for this purpose. MR-only brachytherapy treatment planning would avoid MR-CT misregistration, reduce anaesthesia time for patients undergoing intra-operative imaging, and spare hospital resources.

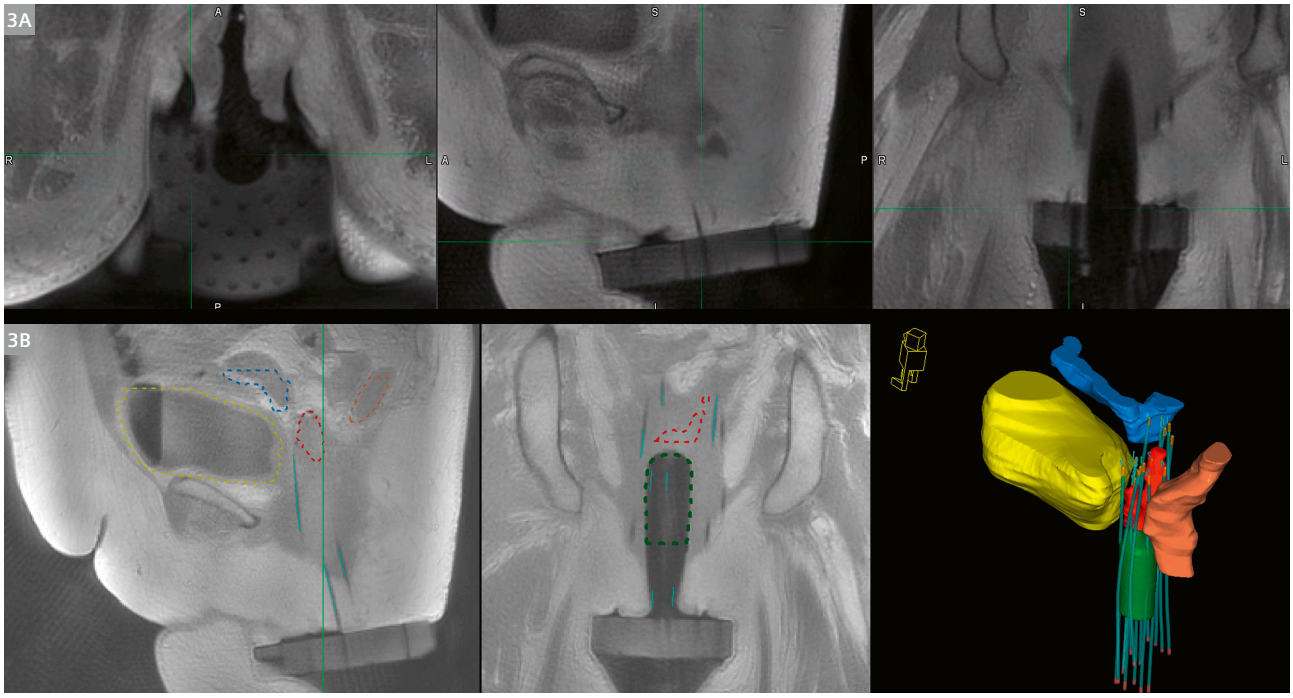

3 **(3A)** PETRA images of an endometrial adenocarcinoma patient zoomed on the interstitial template in all three orientations, with green crosshairs indicating the entry hole of a tracked catheter. **(3B)** Left, middle: sagittal and coronal PETRA views, with overlapping dotted lines indicating contoured structures and turquoise lines showing catheters tracked in a TPS. Right: 3D reconstruction of tracked catheters (turquoise), obturator (green), tumor (red), bladder (yellow), rectum (orange), and bowel (blue). *Reprinted with permission from [7].*

Conclusion

Interstitial HDR brachytherapy catheters and templates were detected on PETRA images of a poultry phantom and of gynaecological cancer patients. Catheters were traceable in a TPS, providing adequate information for treatment plan production. PETRA implementation may pave the way to MR-only treatment planning in interstitial HDR brachytherapy.

References

1 Kirisits C, Rivard MJ, Baltas D, Ballester F, De Brabandere M, Van Der Laarse R, et al. Review of clinical brachytherapy uncertainties: Analysis guidelines of GEC-ESTRO and the AAPM. Radiother Oncol. 2014;110(1):199–212.

2 Sander T. Air kerma and absorbed dose standards for reference dosimetry in brachytherapy. Br J Radiol. 2014;87(1041).

3 Ning MS, Vedam S, Ma J, Stafford RJ, Bruno TL, Cunningham M, et al. Clinical utility and value contribution of an MRI-positive line marker for image-guided brachytherapy in gynecologic malignancies. Brachytherapy. 2020;19(3):305–15.

4 Nosrati R, Paudel M, Ravi A, Pejovic-Milic A, Morton G, Stanisz GJ. Potential applications of the quantitative susceptibility mapping (QSM) in MR-guided radiation therapy. Phys Med Biol [Internet]. 2019;64(14):ab2623. Available from: https://doi.org/10.1088/1361-6560/ab2623

5 Grodzki DM, Jakob PM, Heismann B. Ultrashort echo time imaging using pointwise encoding time reduction with radial acquisition (PETRA). Magn Reson Med. 2012;67(2):510–8.

6 Nath R, Anderson LL, Meli JA, Olch AJ, Stitt JA, Williamson JF. Code of practice for brachytherapy physics: Report of the AAPM radiation therapy committee task group no. 56. Med Phys. 1997;24(10):1557–98.

7 Kaza E, Lee CY, King MT, Dyer MA, Cormack RA, Buzurovic I. cFirst pointwise encoding time reduction with radial acquisition (PETRA) implementation for catheter detection in interstitial high-dose-rate (HDR) brachytherapy. Brachytherapy 2022, in press.

Contact

Evangelia Kaza, Ph.D.
Instructor in Radiation Oncology
Brigham and Women's Hospital
Department of Radiation Oncology
75 Francis Street
Boston, MA, 02115
USA
Ekaza1@bwh.harvard.edu

Ivan Buzurovic, Ph.D.
Assistant Professor of Radiation Oncology
Brigham and Women's Hospital
Department of Radiation Oncology
75 Francis Street
Boston, MA, 02115
USA
Ibuzurovic@bwh.harvard

The Integration of MRI in Radiation Therapy:

The Power of Multidisciplinary Collaboration

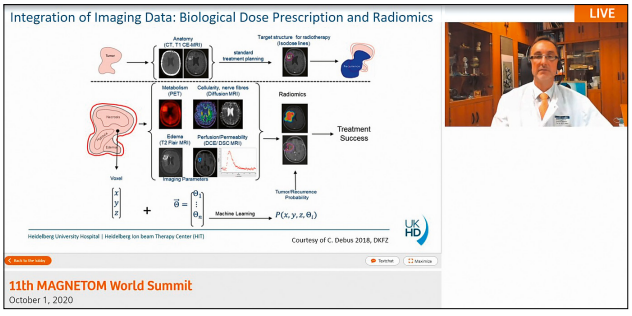

MRI in Radiation Oncology.
See what you treat – treat what you see

Juergen Debus
University Hospital Heidelberg, Germany

Don't miss the talks delivered by experienced and renowned experts at the MAGNETOM World Summit

www.siemens-healthineers.com/MWS2020-recordings

The Application and Utility of Radiotherapy Planning MRI at the Cancer Institute Hospital of JFCR

Yasuo Yoshioka, M.D., Ph.D.

Director of the Department of Radiation Oncology, Cancer Institute Hospital of the Japanese Foundation for Cancer Research (JFCR), Tokyo, Japan

The Japanese Foundation for Cancer Research (JFCR) is the oldest cancer institute in Japan. It consists of the Cancer Institute and the Cancer Institute Hospital of JFCR. The Cancer Institute Hospital of JFCR, located in Koto Ward, Tokyo, is one of the largest cancer hospitals in Japan. The hospital has six linear accelerator rooms with five linear accelerators: three TrueBeam systems and one Clinac EX system (Varian, a Siemens Healthineers Company, Palo Alto, CA, USA), and one Radixact system (Accuray, Sunnyvale, CA, USA). They are constantly running to provide radiotherapy to approximately 1,800 patients per year. All these systems allow for intensity-modulated radiation therapy (IMRT)/image-guided radiation therapy (IGRT). Currently, volumetric-modulated arc therapy (VMAT) or TomoHelical is used for all IMRT patients. IMRT accounted for approximately half of irradiations performed in 2020.

The Department of Radiation Oncology has two CT systems for radiotherapy planning: a SOMATOM Confidence RT Pro (Siemens Healthcare, Forchheim, Germany) and an Aquilion ONE (Canon, Ōtawara, Tochigi, Japan). It also has one self-propelled CT system that incorporates a brachytherapy unit (SOMATOM Definition AS, Siemens Healthcare, Forchheim, Germany). The hospital has five MRI systems, all of which are located in the Diagnostic Imaging Department. Of these, one system – a 3T MAGNETOM Skyra (Siemens Healthcare, Erlangen, Germany) – is shared by the Diagnostic Imaging Department and the Department of Radiation Oncology. The Department of Radiation Oncology has priority to use the MAGNETOM Skyra system for three sessions (1.5 hours) during the day. These are primarily used for radiotherapy planning and also partly for follow-up after the completion of radiotherapy. This article provides details about the application and utility of radiotherapy planning MRI at the Cancer Institute Hospital of JFCR.

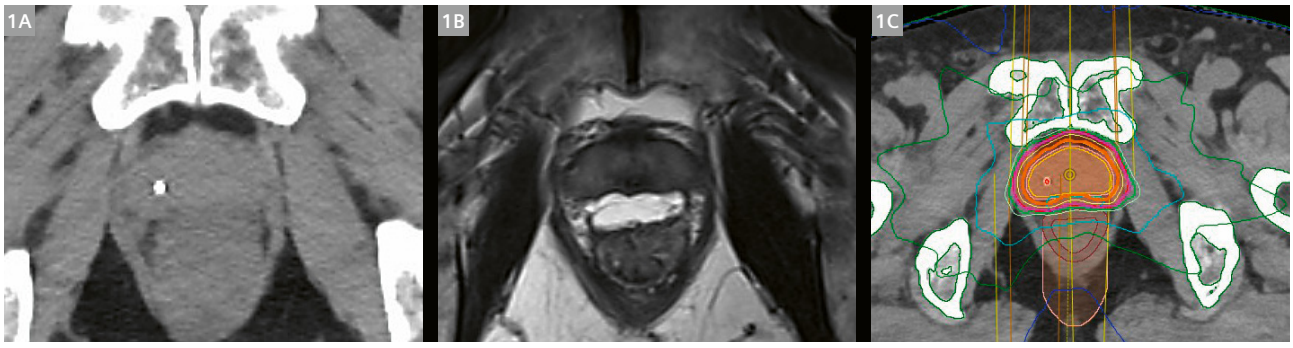

1 A patient who received ultra-hypofractionated radiotherapy for prostate cancer. **(1A)** CT imaging is not good at making a clear distinction between Santorini's plexus surrounding the prostate and the prostate itself, often visualizing the prostate larger than it actually is. Also, CT imaging fails to show a clear border between the hydrogel spacer and the prostate/rectum. **(1B)** MRI clearly visualizes the contour of the prostate and the hydrogel spacer. **(1C)** Structures and isodose lines used for radiotherapy planning. The structure shown in the innermost yellow line is the prostate. The treatment was planned so that the orange bold line (a 100% isodose line) would be generally consistent with the CTV, and the outer bold line in pink (a 90% isodose line) would be generally consistent with the planning target volume (PTV).

Prostate cancer

We use four different radiation modalities for prostate cancer: moderately hypofractionated IMRT (70 Gy in 28 fractions), ultra-hypofractionated stereotactic body radiation therapy (SBRT, 36.25 Gy in 5 fractions), permanent implant brachytherapy (145 Gy), and high dose-rate interstitial irradiation (27 Gy in 2 fractions). Clinically indicated patients can voluntarily choose a treatment from this selection. The radiotherapy planning process is almost the same for IMRT and SBRT: the insertion of a gold marker and a hydrogel spacer 23 days prior to treatment initiation; CT and MRI scans for radiotherapy planning 14 days prior to treatment initiation; input of outline data for two days; radiotherapy planning for two days; and validation and registration for five days.

For the radiotherapy planning CT scan, the patient receives an enema one hour prior to the scan to promote defecation and urination, and then drinks water for urine collection. First, an immobilization device is prepared using the HipFix Thermoplastic Positioning System (CIVCO Radiotherapy, Orange City, IA, USA) and the CT scan is performed. Then the patient moves to the Diagnostic Imaging Department. The radiology technologist also moves to the Diagnostic Imaging Department with the immobilization device. While waiting, with sufficient time allowed for urine collection, the patient is instructed to urinate once and then store urine for one hour. Since the images for qualitative diagnosis are already acquired during preoperative staging MRI, the sequence focusing on prostate outlining is used for radiotherapy planning MRI. A total of three scans are performed: The T2-weighted (T2W) and VIBE FatSat scans provide excellent outlining, and a 3D MEDIC scan enables clear detection of the gold marker. It is known that CT images are not good at making a clear distinction between Santorini's plexus surrounding the prostate and the prostate itself; they visualize the prostate larger than it actually is. It is also difficult to identify the prostate apex and the edge of the hydrogel spacer when CT imaging is used, whereas MRI can detect them more clearly (Fig. 1). Based on these findings, we believe that MRI fusion is mandatory for high-precision radiotherapy for prostate cancer.

Head and neck cancer

At the Cancer Institute Hospital of JFCR, a setup similar to the one used for radiotherapy planning CT imaging is reproduced during radiotherapy planning for IMRT to treat head and neck cancer, and the MR imaging is performed on the same day. This allows an accurate fusion of CT and MRI images, resulting in precise contouring. We also use diagnostic MRI, but it often results in inaccurate fusion due to the difference in imaging postures. The basic type of scan we use is T2W, with the field of view (FOV) being adjusted for each case.

By visualizing not only primary lesions but also cervical lymph node metastases, MRI accurately captures the exact positioning of the target in relation to tissues such as blood vessels, muscles, bone, and nerves, and helps improve the quality of the contouring of the target (Fig. 2). MRI also provides clearer images of postoperative structural changes than plain CT imaging does. This enables better recognition of the muscles around the hyoid bone; the digastric, sternocleidomastoid, and scalene muscles; adipose tissue; and the carotid arteries (Fig. 3).

Generally, the diagnostic MRI is essential for determining the range of the progression of tumors that have invaded the skull base and those found in the head and face areas. Additional scans are also often performed to acquire MRI images for radiotherapy planning, which are

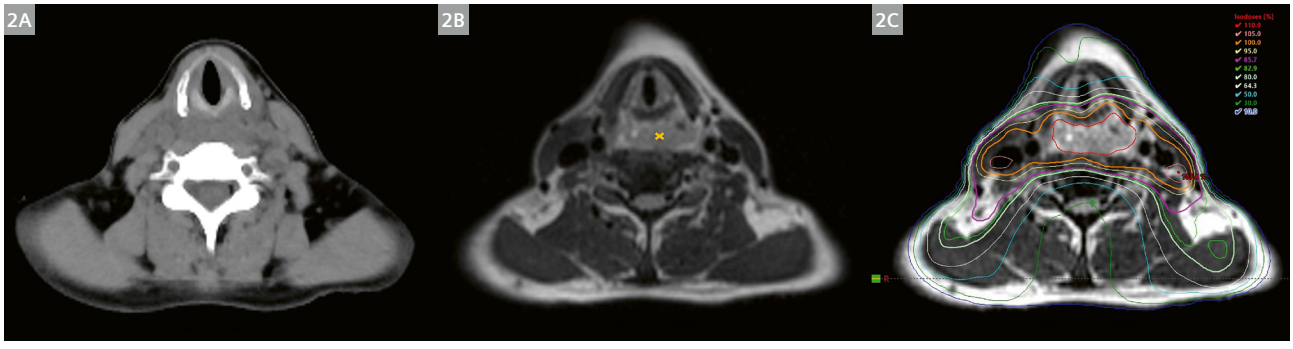

2 Hypopharynx cancer (posterior wall T3). **(2A)** On the radiotherapy planning plain CT scan, the tumor is poorly distinguished from the surrounding structures. **(2B)** On the MRI scan (T2W), the tumor (×) is easily recognized and its border with the prevertebral muscles is clearly visualized. The carotid arteries and cervical veins that serve as an indicator for enclosing the lymphatic region are clearly visualized as a flow void, which makes it easy to recognize the sternocleidomastoid and scalene muscles. **(2C)** A VMAT radiation dose distribution map. This allows for radiotherapy planning that accurately covers the target while avoiding OARs.

fused with diagnostic images for accurate contouring (Fig. 4). MRI can also successfully visualize the sites that are not well visualized by CT imaging because of scattered radiation caused by metal crowns in the mouth.

Conventional fractionation (66 to 70 Gy) to treat head and neck cancer requires a treatment duration of six to seven weeks, during which the tumor lesion changes in size and shape. There are many cases in which extensive cervical lymph node metastases have not completely disappeared at the end of scheduled concurrent chemoradiotherapy (CCRT). If this is the case, one needs to determine whether additional treatment should be provided. We leverage the assessment of the tumor size and signal changes using MRI during CCRT to determine the need for additional administration of anticancer drugs or resection.

MRI is very useful in clinical practice for precision radiotherapy for head and neck cancer and is expected to be indispensable in the future.

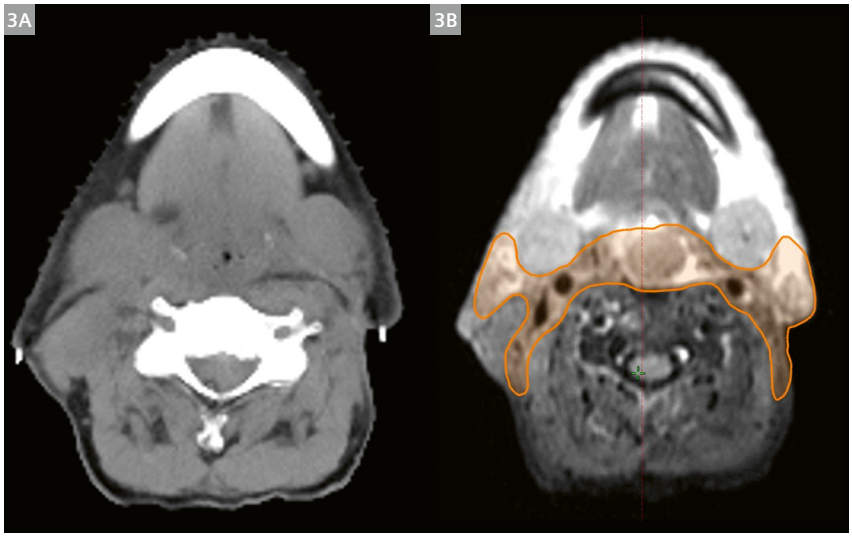

3 Postoperative radiotherapy for larynx cancer (after removal of the entire hypopharynx and larynx, followed by bilateral cervical lymph node dissection, resection of the left sternocleidomastoid muscle, and free jejunal reconstruction). **(3A)** On the radiotherapy planning CT (plain), it is difficult to distinguish each organ, with little adipose tissue in the lymphatic region following cervical lymph node dissection. **(3B)** The use of radiotherapy planning MRI (T2W) makes it easy to identify a postoperative structural change, and to enclose the lymphatic region (orange line) using the carotid arteries and cervical veins, muscles, and submaxillary gland as indicators.

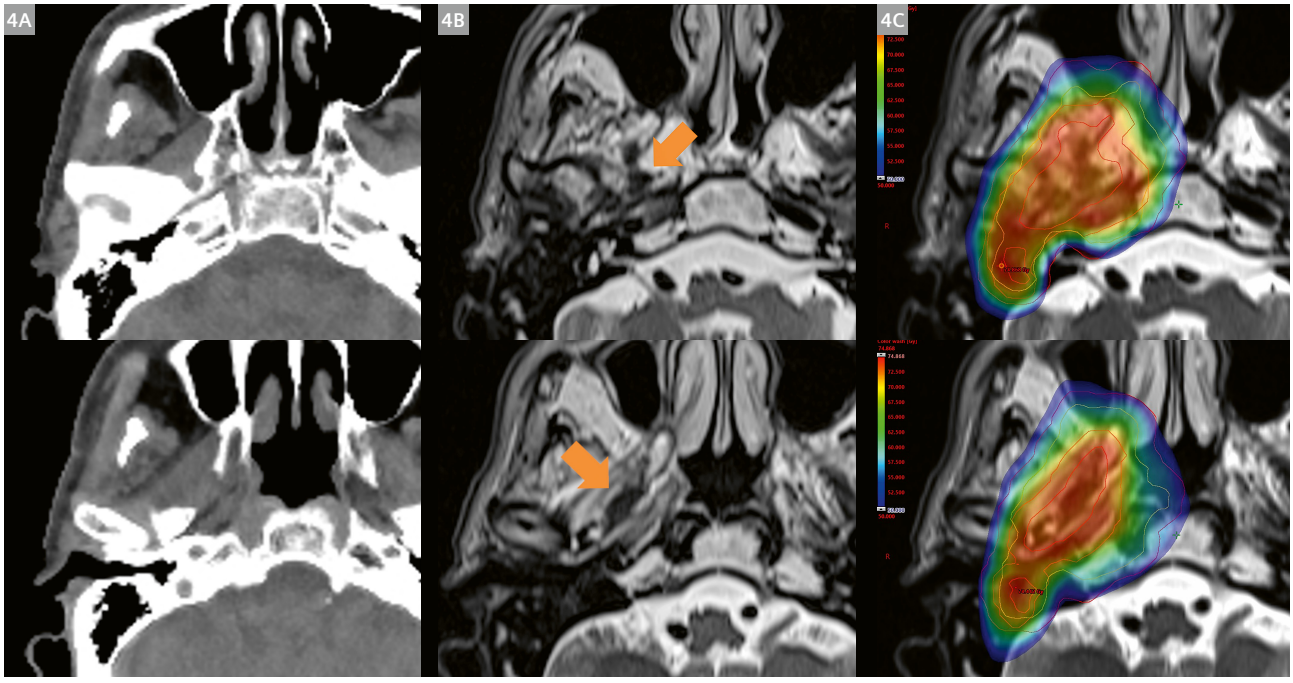

4 Tumor recurrence around the trigeminal nerve following surgery for oral floor cancer. **(4A)** On the plain CT, it is difficult to recognize the lesion. **(4B)** Radiotherapy planning MRI (T2W). The lesion is observed along with the trigeminal nerve (arrow). In addition, the image clearly shows the contrast of the soft tissue or bones at the skull base. **(4C)** A VMAT radiation dose distribution map. Optimal radiotherapy planning is achieved by accurately enclosing the target using MRI.

Vertebral stereotactic irradiation, cervical cancer, and others

Based on the recent idea that radiotherapy for oligometastases may improve the overall survival rate, stereotactic irradiation, which enables local delivery of high radiation doses, began to be actively used for oligometastases. Since the vertebral body is adjacent to vital organs such as the spinal cord and the esophagus, vertebral stereotactic irradiation requires extremely precise radiotherapy planning. As MRI is superior to CT imaging in terms of providing information about how deep the tumor extends inside the vertebral body and visualizing the spinal cord as an organ at risk (to distinguish it from the spinal fluid), we always use MRI in combination with CT imaging when planning vertebral stereotactic irradiation therapy.

The Cancer Institute Hospital of JFCR uses brachytherapy for cervical and prostate cancers. For cervical cancer, external irradiation during the first half of radiotherapy often dramatically reduces the tumor size, resulting in a remarkable difference in the size and shape of the tumor between staging (Fig. 5A) and initiation of intracavitary irradiation (Fig. 5B, C). We use images from the self-propelled CT system that partly incorporates a brachytherapy unit to create plans for intracavitary radiotherapy (Fig. 5D–F). By performing MRI scans immediately before intracavitary irradiation, we have a reference for inputting contours of the clinical target volume (CTV) during intracavitary radiotherapy planning (fusing is difficult due to uterus deformation related to tandem insertion). If intracavitary irradiation fails to give a sufficient dose to the tumor, we use interstitial irradiation. In this case, the

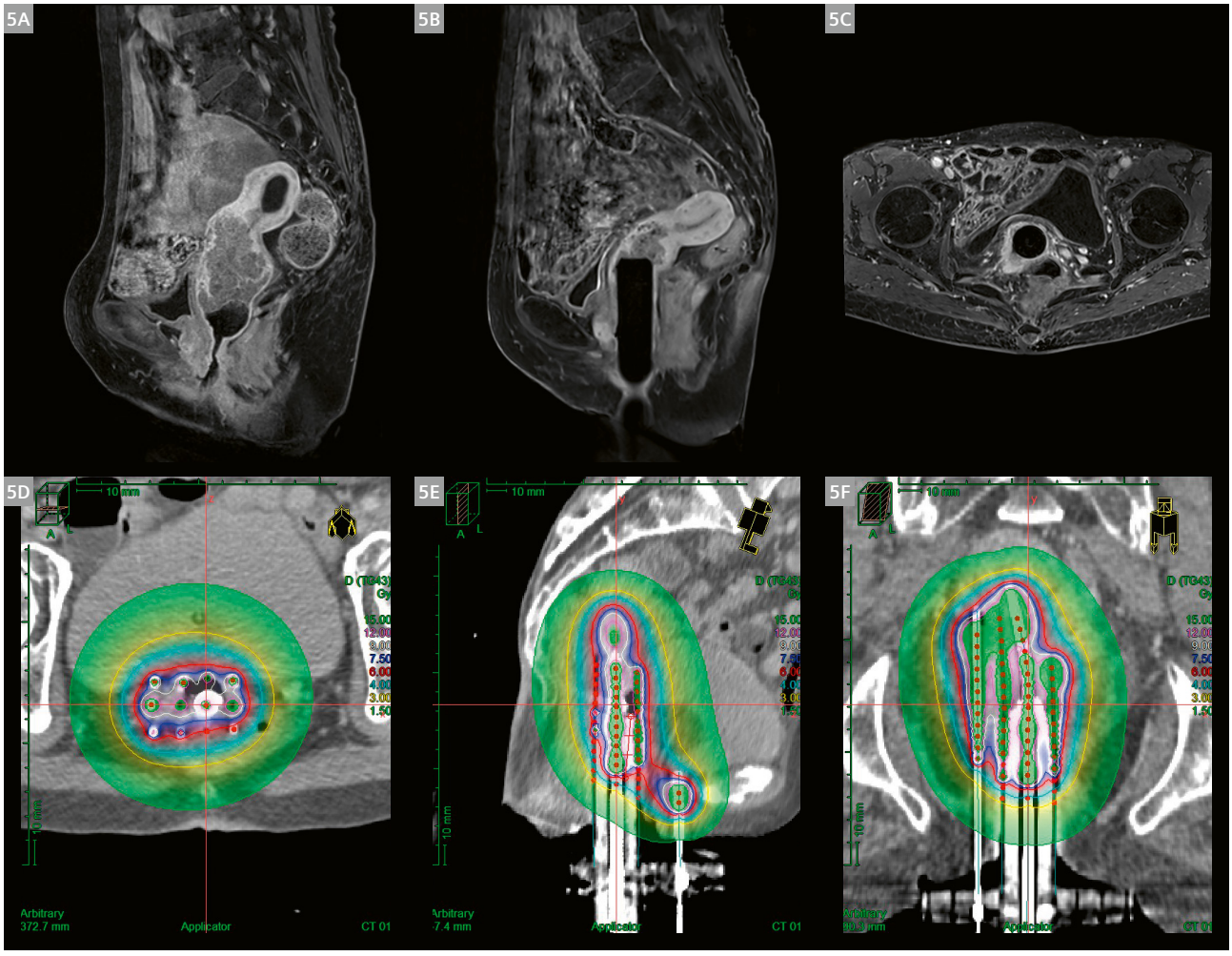

5 A patient who received concurrent chemoradiotherapy for cervical cancer. **(5A)** Staging MRI. **(5B)** An MRI image acquired immediately before interstitial irradiation (with a cylinder inserted for interstitial irradiation); a sagittal section image. **(5C)** A horizontal section image of 5B. **(5D)** A radiation dose distribution map of high dose-rate interstitial irradiation (with CT used as a base); a horizontal section image. **(5E)** A sagittal section image of 5D. **(5F)** A coronal section image of 5D.

cylinder used for interstitial irradiation (which is attached to the template during needle insertion) is inserted into the vagina to acquire MRI images (Fig. 5D–F), and a prior simulation is performed to select the grid point on the template that will be used as the site of needle insertion. In other cases where it is difficult for CT scans to distinguish the tumor from the soft tissue (e.g., esophageal and lung cancers with mediastinal invasion, and pancreatic cancer), we might include radiotherapy planning MRI. For patients with a brain metastasis, on the other hand, we usually use diagnostic contrast-enhanced MRI images directly for radiotherapy planning because endocranial fusion is unlikely to be affected by the base plate or the immobilization device. In this case, we take care to assign it to the radiotherapy planning MRI system (3T MAGNETOM Skyra) at our hospital at the time of the diagnostic MRI scan. This is because the positional accuracy for radiotherapy is guaranteed only for that system.

Summary

The Cancer Institute Hospital of JFCR has two radiotherapy planning CT systems in the Department of Radiation Oncology, and five MRI systems in the Diagnostic Imaging Department. One of the five MRI systems is used for radiotherapy planning during three sessions every day. For radiotherapy planning for IMRT to treat prostate or head and neck cancer, and for vertebral stereotactic irradiation, the following procedures are established:

1) Preparation of the immobilization device using one of the CT systems in the Department of Radiation Oncology
2) CT scan and
3) MR imaging at the Diagnostic Imaging Department.

The negative aspects of these procedures include the following:

a) It takes the patient half a day to complete the imaging examinations due to the time interval between the appointment times for CT and MRI.
b) There may be a change in urine output, stools, and gas during this time interval in patients with prostate cancer.
c) The radiology technologist needs to go back and forth between the two departments carrying the immobilization device, and change the MRI base plates.

From a management point of view, however, sharing with the Diagnostic Imaging Department is a reasonable solution to maintain the utilization rate of the expensive MRI systems. We have been operating in this manner for five years and we currently do not have any major problems. As a radiation oncologist, I realize that the use of MRI has certainly contributed to high-precision radiotherapy planning; however, I see it as our future responsibility to provide clinical data that will improve the local control rate and reduce adverse events. We will be pleased if the way we use MRI helps the readers in some way.

Contact

Professor Yasuo Yoshioka, M.D., Ph.D.
Director, Radiation Oncology Department
Cancer Institute Hospital of the Japanese Foundation for Cancer Research (JFCR)
3 Chome-8-31 Ariake, Koto-ku
Tokyo 135-8550
Japan
Phone: +81 3-3520-0111
yasuo.yoshioka@jfcr.or.jp

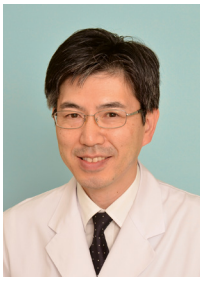

Put the advantages of the MAGNETOM World to work for you!

www.siemens-healthineers.com/magnetom-world-rt

Siemens Healthineers' global MRI community offers peer-to-peer support and information. Radiation Oncologists, Radiologists, Medical Physicists, Technologists and Cardiologists have all contributed with publications, presentations, training documents, videos, case studies and more – all freely available to you via this unique network.

Don't miss the MRI protocols and practical tips and tricks for several body regions from experts for both experts and novice users. The information can help in supporting your entire clinical team and grow your practice.

The centerpiece of the MAGNETOM World Internet platform consists of MAGNETOM users' results. Here you will find articles, case reports and application tips allowing you to optimize your daily work.

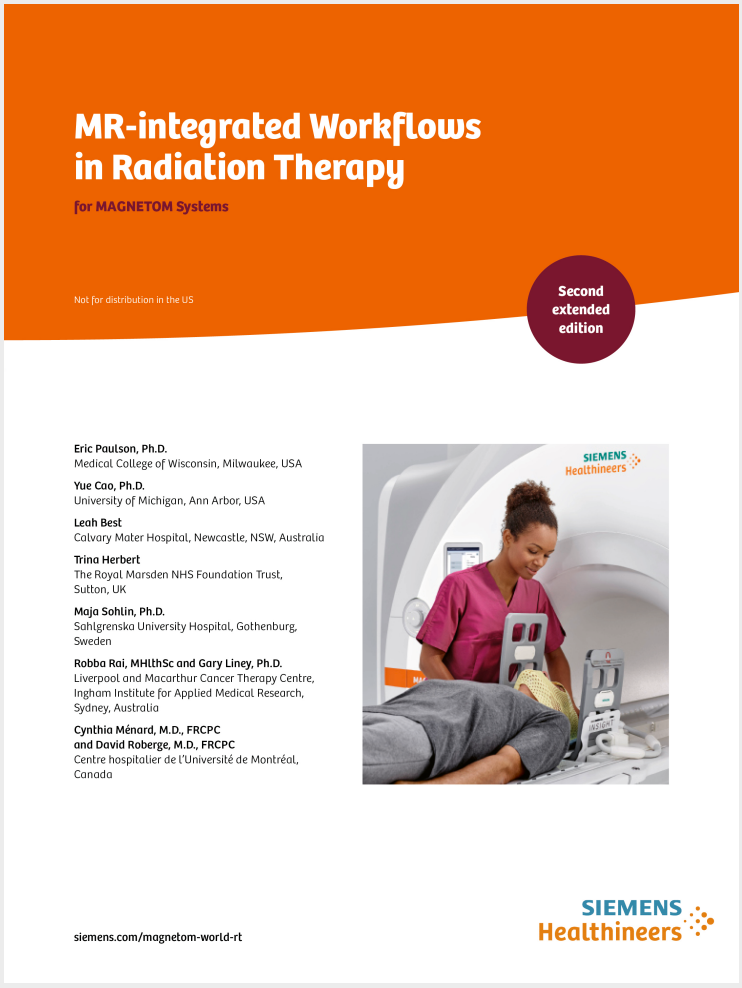

MR-based Synthetic CT. An AI-based Algorithm for Continuous Hounsfield Units in the Pelvis and Brain – with *syngo*.via RT Image Suite

Michaela Hoesl, Ph.D.; Nuria Escobar Corral, Ph.D.; Nilesh Mistry, Ph.D.

Siemens Healthineers

Why MRI in radiotherapy?

Radiotherapy treatment simulation and planning are conventionally performed on computed tomography (CT) images because of the intrinsic relationship between Hounsfield units (HU) and electron density information, needed to model radiation attenuation in the treatment planning system [1]. Compared with CT images, MRI shows superior soft-tissue contrast (Fig. 1) and is becoming the modality of choice for delineation of target organs and organs at risk (OAR) [2]. Moreover, MRI gives access to multiparametric data, such as T1w, T2w, dynamic contrast-enhanced MRI (DCE-MRI), and diffusion-weighted imaging (DWI) [3–7], which play an increasingly important role in the whole workflow from diagnosis, structure delineation, treatment planning, and response assessment.

1 **(1A)** CT, **(1B)** MRI (T2 FLAIR)
Courtesy of Universitätsklinikum Erlangen, Germany.

Dose calculation

Dose calculation requires a 3D electron or mass density map and unfortunately the necessary correlation between the nuclear magnetic properties and electron density is missing. Therefore, MR images cannot directly be used for dose calculation. When MR images are used for contouring, a CT image is required for dose calculation, resulting in a combined MRI-CT workflow.

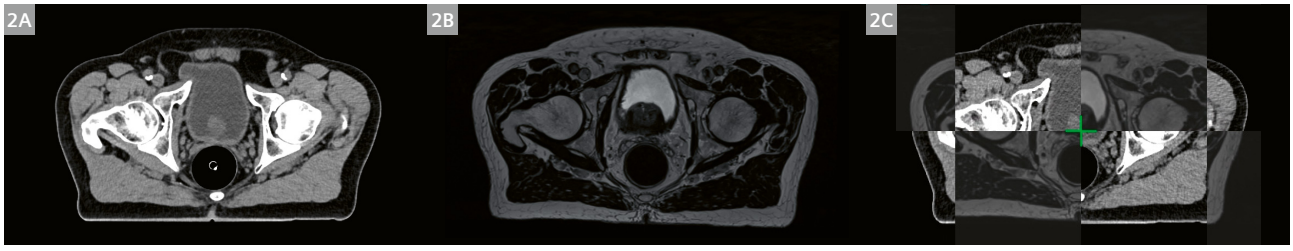

2 **(2A)** Planning CT, **(2B)** T2w MRI, **(2C)** registration visualized with the checkerboard tool[1]. Registration errors may persist and registration can be cumbersome. *Courtesy of Universitätsklinikum Erlangen, Germany.*

[1]*Since syngo.via RTiS VB60.*

Main challenge of a combined MRI-CT workflow

In multimodality workflows, rigid and sometimes deformable image registration (DIR) are employed. When anatomies deviate significantly (bladder filling or rectal filling, Fig. 2) fusing of CT and MRI modalities becomes difficult and adds to uncertainties in the planning process [8, 9].

MR-only workflow for the pelvis and brain

The MAGNETOM Sola (1.5T) and MAGNETOM Vida (3T)[2] are our MRI systems supporting MR-only workflows. Both MAGNETOM RT Pro edition systems are dedicated to RT with continuous development and updates with the latest features for RT simulation:

- Reproducible patient positioning with MR-compatible, certified, and indexed flat tabletop overlays, immobilization devices, and an external laser bridge
- Flexible coils with multiple channels
- RT Dot Engine with dedicated RT protocols including workflow guidance
- Automatic, optimal (2D/3D) distortion correction for spatial integrity for robustness and reproducibility
- QA solutions including an in-depth guide: QA cookbook [10]
- MR-based Synthetic CT with continuous HU

An example of an MR-only workflow protocol for pelvis is shown in Figure 3. The key sequence for MR-based Synthetic CT reconstruction, the T1 VIBE-Dixon sequence, follows the optional T1w and T2w clinical sequences for morphological information precontrast and postcontrast. Additional sequences, such as, for example diffusion-weighted images (DWI), can be acquired to obtain further insights and support target definition [18].

Advanced sequences like DWI can potentially be used for treatment response evaluation [11].

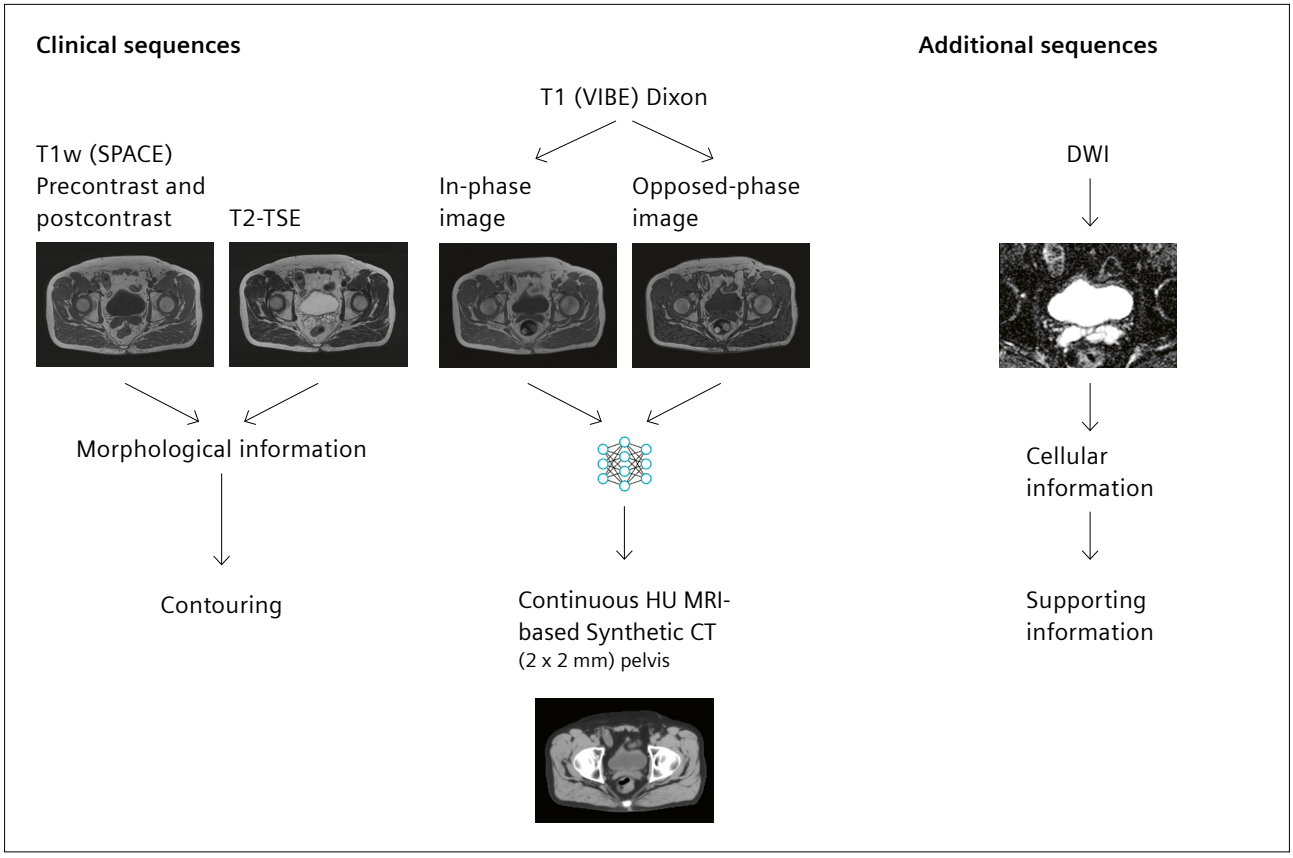

3 Example of a scanning protocol for a prostate MR-only workflow. *Courtesy of Universitätsklinikum Erlangen, Germany.*

[2]*The data acquisition protocols for Synthetic CT are available with syngo MR XA11A and later software versions with MAGNETOM RT Pro edition for MAGNETOM Vida and MAGNETOM Sola, with syngo XA30 and later software Versions for MAGNETOM Aera and MAGNETOM Skyra.*

MR-based Synthetic CT generation algorithm – How does it work?

In recent years, the field of MR-based Synthetic CT imaging has gained substantial interest [12–17]. Different methods have been proposed to create electron density information from MRI artificially [15, 18]. Our latest algorithm for MR-based Synthetic CT is an AI-based algorithm. The model was trained by leveraging deep learning (DL) neural network technology. The DL algorithm uses a combination of multilayer neural networks to learn Synthetic CT reconstruction. Training was accomplished using a large number of datasets for training with 6486 CT and MRI image pairs for brain and 9059 for pelvis (validation sets were 553 for brain and 695 for pelvis). For the training image pairs, CT images were registered to MRI using rigid and deformable registration. The input for the trained deep learning algorithm are only the VIBE-Dixon in-phase and opposed-phase images for Synthetic CT reconstruction. The AI-based Synthetic CT product comes fully trained to the user and does not continue training at the user's site.

The network architecture (Fig. 4) consists of two parts:
Network 1: convolutional neural network (densely connected UNet) for segmentation in three classes: background, bone, and soft tissue from a two-channel input using the MR images.

Network 2: generator and discriminator (conditional GAN) for Synthetic CT reconstruction with continuous HU (one output channel). During training, the input and condition are the MR images concatenated with the segmentation results of the first network (five input channels) to guide the training of the conditional GAN.

- Generator (densely connected UNet): receives a five-channel input (in-phase, opposed-phase Dixon MRI and the segmentation output in three tissue classes) for Synthetic CT reconstruction.
- Discriminator: tries to discriminate the prediction of the generator (Synthetic CT) from the ground truth (real CT image). During training, the information is fed back iteratively to yield a machine-generated Synthetic CT, which is indistinguishable from a real CT image.

VIBE Dixon acquisition for MR-based Synthetic CT reconstruction

MR scanning parameters for the VIBE-Dixon sequence as input for Synthetic CT reconstruction are automatically handled in the RT Dot Engine.
In the RT Dot Engine, axial orientation reformatting and distortion correction are automatically preselected. The neural network imposes certain requirements on the input data. The network expects MR volume pairs in axial orien-

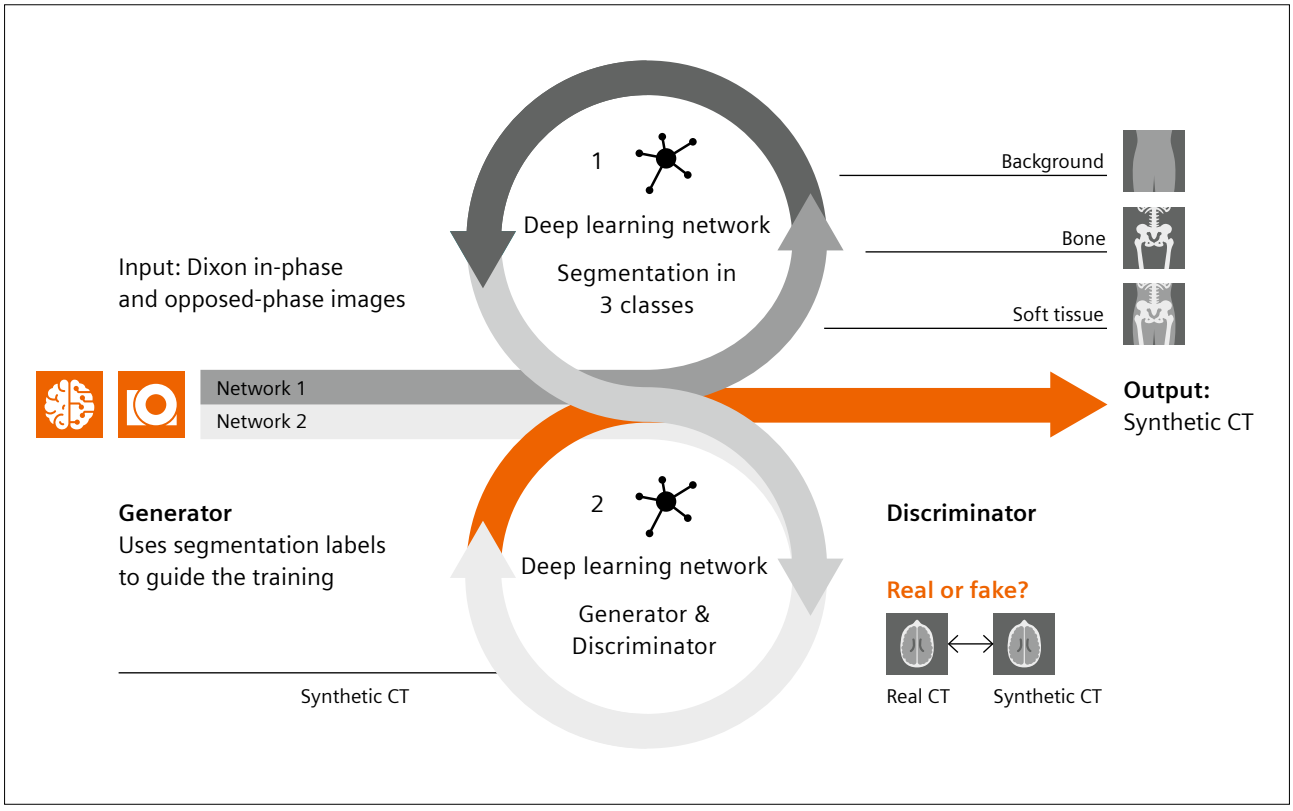

4 The cGAN (conditional generative adversarial network) training scheme.

tation. Therefore, volumes are always reformatted to axial orientation. The fully trained network requires input images with dimensions (in x-axis and y-axis) in multiples of 16, which is also pre-selected in the RT Dot Engine. Otherwise, zero padding is performed before the synthesis. Additionally, input images need 98th percentile normalizations, which is done automatically in the postprocessing pipeline.

The resulting Synthetic CT has an in-plane resolution of 1 × 1 mm (brain) and 2 × 2 mm (pelvis). The slice thickness is determined by the acquired input data.

Synthetic CT import in the treatment planning system

The generated MR-based Synthetic CT image can be exported in HU, relative electron density (RED), and relative mass density (RMD). When exported as HU, for dose calculation the HU values of the synthetic CT have to be converted to RED or RMD in the TPS. For this purpose, the following table can be used. If RED and RMD are chosen as output, the calibration table is automatically applied by the software. The MR-based Synthetic CT image is labeled in DICOM as "CT" and is therefore recognized by the TPS and LINAC as a CT image.

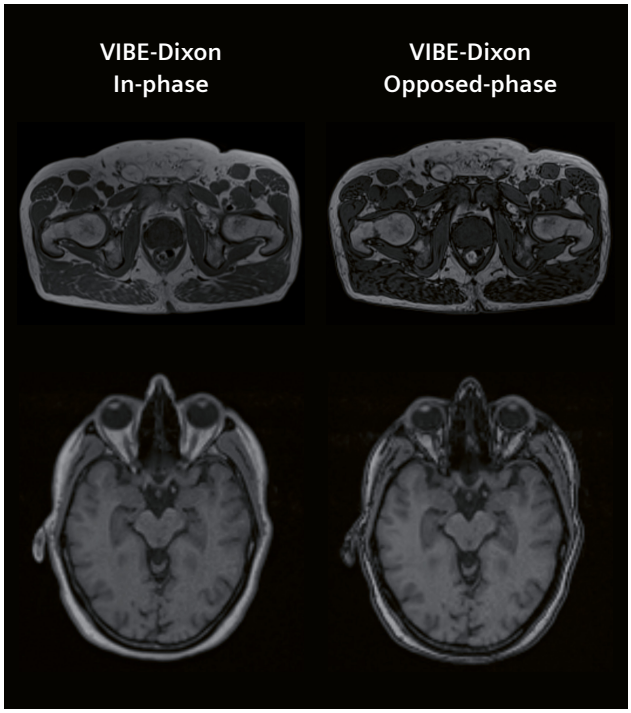

5 VIBE-Dixon in-phase and opposed-phase images of a male pelvis and brain.

T1 VIBE Dixon	1.5T acquisition time	Resolution	3T acquisition time	Resolution
Head	3 min 25 s	1.5 × 1.5 × 1.5 mm³	2 min 22 s	1.3 × 1.3 × 1.0 mm³
Pelvis	2 min 21 s	2.0 × 2.0 × 2.0 mm³	1 min 33 s	2.0 × 2.0 × 2.0 mm³
	4 min 12 s	1.6 × 1.6 × 2.0 mm³	2 min 48 s	1.6 × 1.6 × 2.0 mm³

Table 1: T1 VIBE-Dixon sequence with example acquisition time and image resolution at 1.5T and 3T for brain and pelvis: For pelvis, the acceleration mode CAIPIRINHA [18] was selected with a total acceleration factor of 4–5. For the brain at 1.5T, no acceleration mode was used. At 3T, GRAPPA [19] with a total acceleration factor of 2 was selected.

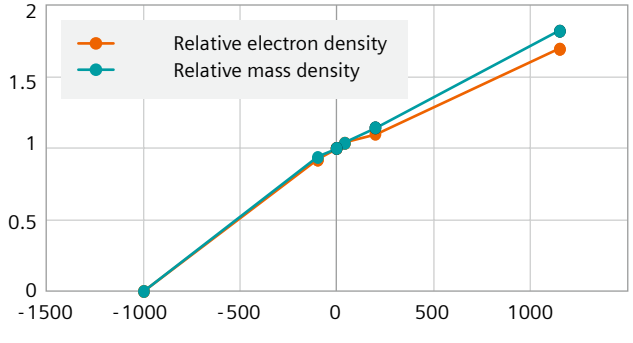

Tissue class	HU value	Relative electron density	Relative mass density
Air	-1000	0	0
Fat	-100	0.924	0.941
Liquid	0	1	1
Brain/muscle	40	1.04	1.04
Spongeous bone	200	1.096	1.143
Cortical bone	1150	1.695	1.823

6 Synthetic CT calibration curve.

MR-based Synthetic CT results for pelvis and brain

In Figure 7, an example of the results obtained for pelvis and brain are shown. Both the soft-tissue window level and bone window level are presented. Besides dose planning, Synthetic CT can be used to verify the patient's position on the LINAC by matching the Synthetic CT with the cone-beam CT or the 2D synthetic DRR (derived from the Synthetic CT) with the flat-panel radiograph (Fig. 8).

Evaluation of geometric fidelity and CT number accuracy

We performed an internal validation of geometric fidelity and HU accuracy. The geometric fidelity test was passed for both brain and pelvis with an average symmetric surface distance (ASSD) of less than 1 mm (0.9 ± 0.1 mm pelvis, 0.8 ± 0.1 mm brain), which is below the in-plane pixel resolution of 1 mm (2 mm) for the brain (pelvis) and therefore negligible. For HU accuracy, line profiles from CT and MR-based Synthetic CT from the same patient were compared. An example of this comparison is shown in Figure 9. In addition to that, the HU values of the MR-based Synthetic CT were evaluated in multiple 2D regions of interest (ROI) of the tissue types: fat, liquid, soft tissue, and bone and were each compared with the expected literature values. All values, including deviations, fell within the expected range and tolerance (Table 2).

For visual inspection of geometric accuracy, *syngo*.via RTiS VB 60 provides a checkerboard tool (Fig. 11A). The HU can be verified in regions of interest using the ROI tool, see Figure 11B.

7 Synthetic CT for the pelvis and brain in two different window levels (W/L): bone and soft tissue.

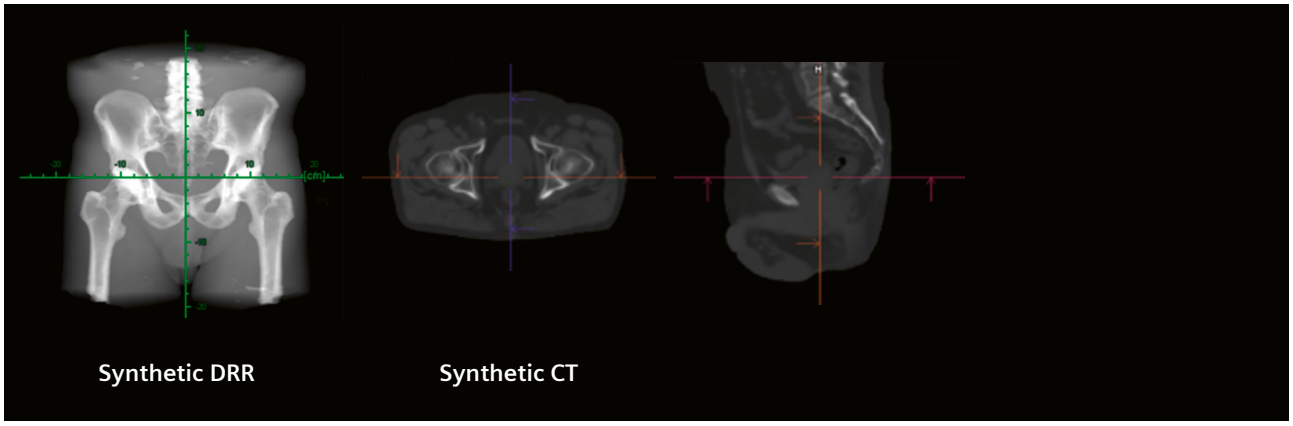

8 Synthetic DRR for matching with DRR and Synthetic CT for matching with cone-beam CT images for patient positioning.

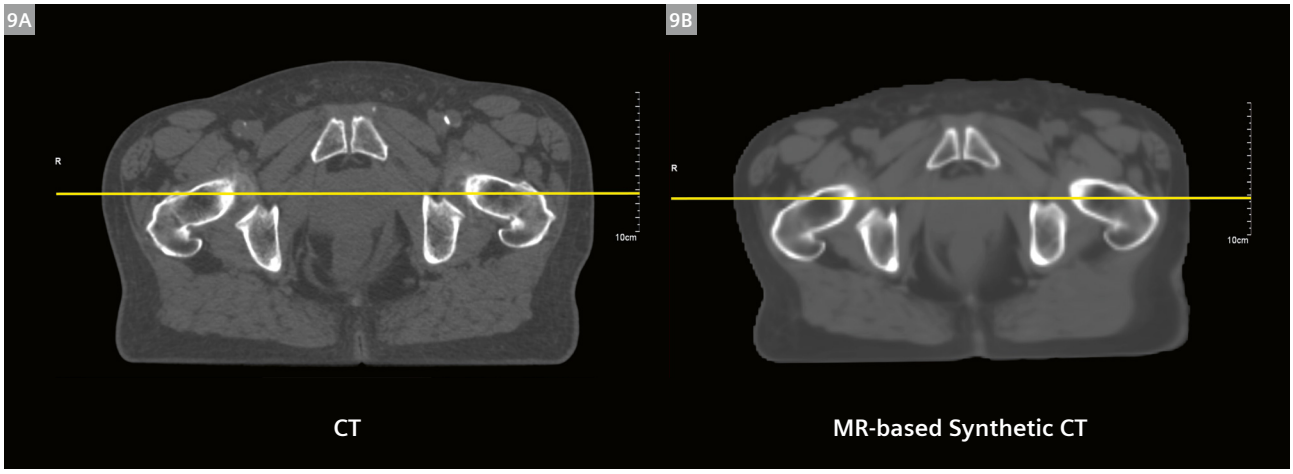

9 **(9A)** Planning CT, **(9B)** MR-based Synthetic CT and graph comparing HU along the line profile (yellow lines).
Courtesy of Centre Hospitalier de l'Université de Montréal – CHUM, Montreal, Canada.

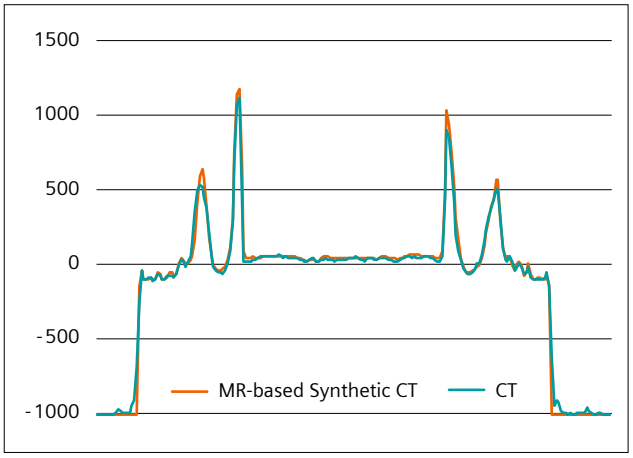

10 Line profile comparison.

ROI	Reference values[3]	Measured in brain	Measured in pelvis
Fat	-100 ± 50	-59 ± 4	-97 ± 1
Liquid (ventricles, bladder)	0 ± 50	7 ± 1	8 ± 2
Soft tissue (brain, muscle)	40 ± 50	27 ± 1	44 ± 2
Cortical bone (skull, femoral head)	1150 ± 200	1103 ± 59	1236 ± 17
Spongeous bone (femoral shaft)	200 ± 200	–	277 ± 9

Table 2: Hounsfield unit (HU) comparison of the MR-based Synthetic CT in multiple regions of interest (ROI) of different tissue types with expected literature values.

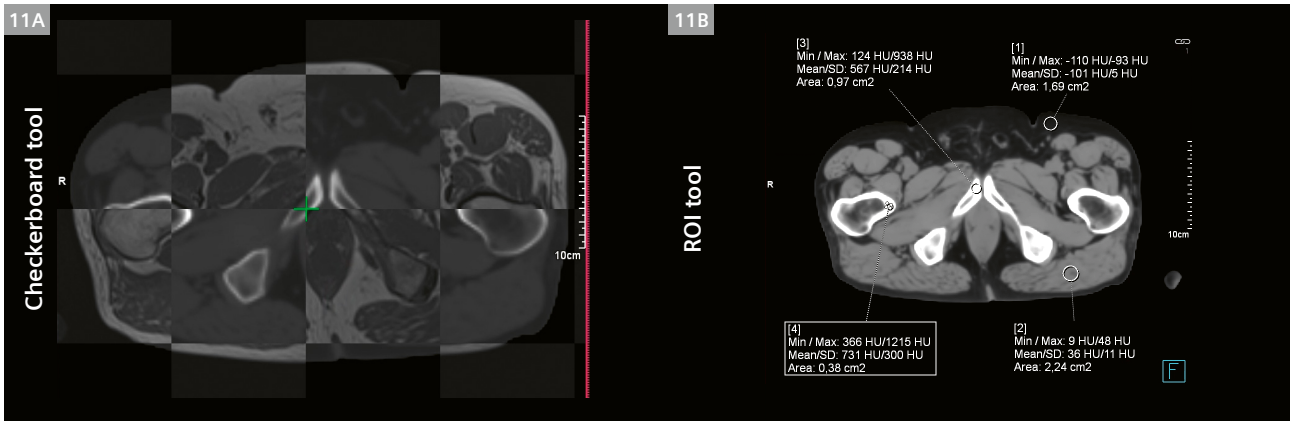

11 Geometric accuracy and HU value verification with checkerboard inspection and ROI tool in a pelvic case.

[3]*Reference values match the CT lookup table (Table 1).*

Clinical evaluation

Dose difference evaluation between the CT and Synthetic CT is the crucial metric for radiation therapy. The dosimetric and spatial positioning evaluation of the new algorithm relative to standard CT-based planning was performed by two independent clinical partners.

Summary

1. Evaluation of the pelvic MR-based Synthetic CT from Brigham & Women's Hospital, Dana-Farber Cancer Institute, Harvard Medical School, Boston, MA, USA[4]
Overall, differences between the original dose distribution and the dose recalculated on the Synthetic CT were: < 1% dose difference in the CTV and evaluated OAR for the seven prostate patients examined. The mean dose difference (ΔDose = Dose (planning CT) – Dose (registered Synthetic CT)) from the CTV was -0.21% relative to total dose.

- 1%/2 mm gamma analysis showed mean agreement of 98.9 ± 0.3% (range 98.4–99.3%).

Regarding spatial positioning evaluation, 0.12 mm/ -0.72 mm/-0.56 mm differences in x-, y-, and z-direction (range: -1.8–1.4 mm) between registered Synthetic CT to CBCT registration and planning CT-CBCT registration.

2. Evaluation of the brain MR-based Synthetic CT from Universitätsklinikum Erlangen, Germany
The mean dose difference was computed and analyzed for all patients for the target volumes (PTV, GTV) and the evaluated organs at risk (brainstem, chiasma, optical nerves).

- < 1% mean dose difference (normalized to the total planned dose) in all the regions of interest
- < 1% (median 0.06%) mean dose differences of PTV and GTV
- < 0.5% and 1.4% mean dose difference for the brainstem and chiasma respectively

[4] *The clinical evaluation was performed on a prototype; its algorithm does not deviate from the released product.*

Full evaluation

1. Evaluation of the pelvic MR-based Synthetic CT from Brigham & Women's Hospital, Dana-Farber Cancer Institute, Harvard Medical School, Boston, MA, USA
A total of seven prostate cancer patients scheduled for subsequent EBRT underwent same-day MRI (MAGNETOM Vida 3T) and CT (SOMATOM Confidence) simulation. All patients were clinically planned and treated using their planning CT scanner. Parameters were as follows:

- CT: 0.976 × 0.976 mm voxel size, 3 mm slice thickness
- MRI: 336 × 448 mm field of view, 2 × 2 mm voxel size, 2 mm slice thickness. T1 VIBE-Dixon Synthetic CT protocol sequence
- TPS: Eclipse 15.6
- Treatment technique: 6 MV X-rays using a VMAT (RapidArc)
- Dose prescription: 180 cGy/fr for 44 fractions. Some patients received simultaneous integrated boosts and altered fractionations.

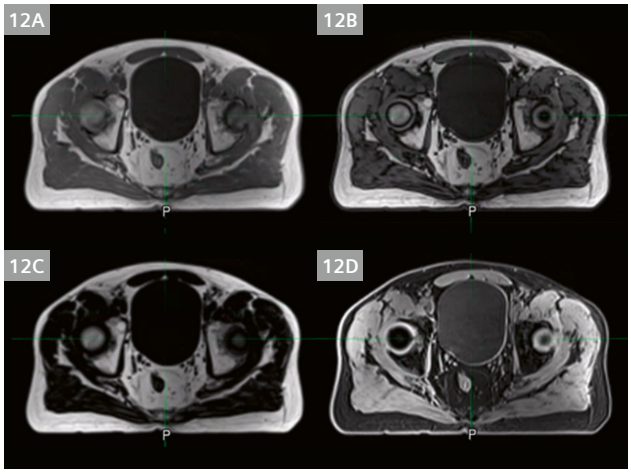

12 Four MR contrasts generated by the T1 VIBE-Dixon scan protocol **(12A)** in-phase (IP), **(12B)** opposed-phase (OP), **(12C)** fat, **(12D)** water. Only 12A and 12B are needed for Synthetic CT postprocessing.

Dosimetric accuracy evaluation of the AI-Synthetic CT
MR-based Synthetic CT images were registered to the planning CT (pCT), resampled and then saved into the frame of reference of the pCT. These registered MR-based Synthetic CTs (called "rsCT" in the following) were then imported into the Eclipse treatment planning system. The clinical treatment plans (based on pCT) were copied and recomputed onto the corresponding rsCT using the same plan parameters. Dose differences were computed in OARs (bladder, rectum, and left and right femoral heads) and the CTV prostate target structure. The original contours (from the pCT scans) were used for all subsequent analyses. Dose distributions obtained using the pCT and the rsCT were compared using a 1%/2 mm gamma criteria [19].

Assessment of spatial localization accuracy (cone-beam CT (CBCT) registration)
Spatial (on treatment) localization accuracy of the Synthetic CT was evaluated by comparing Synthetic CT to CBCT registration results with pCT-CBCT registration in Eclipse/Aria using the Image Registration tool. The first five CBCT scans of each patient were used for this study. Two types of translation-only registrations were performed:

- CBCT scans were registered to the space of the pCT.
- CBCT scans were registered to the space of the rsCT (Synthetic CT registered to the planning CT).

Differences in the translation vectors of the pCT-CBCT registration and rsCT-CBCT registration (e.g., Δx = translation_x(pCT)−translation_x (rsCT)) were calculated and averaged among the five CBCT cases.

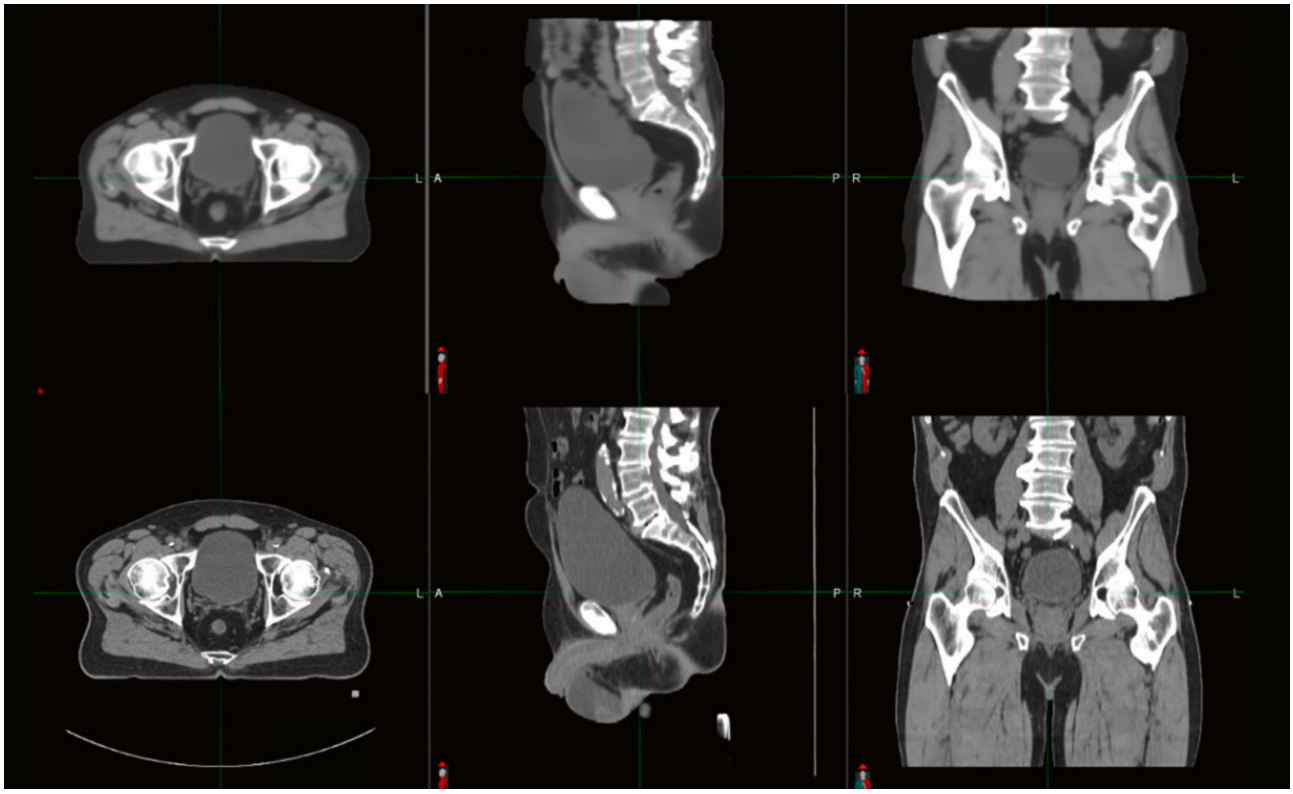

13 MR-based Synthetic CT (top) compared with conventional planning CT (bottom) of the same patient.

Dosimetric results in the pelvis

Differences between the original dose distribution on the pCT and the recalculated dose distribution on the Synthetic CT were globally < 1% for the seven patients examined. The difference in the dose calculated for the prostate (CTV), penile bulb (when contoured), bladder, rectum, and both femoral heads are tabulated in Table 3. The mean dose difference (ΔDose = Dose (pCT)–Dose (rsCT)) to the CTV was -0.21% relative to the total dose. Results of gamma analysis at 1%/2 mm showed a mean agreement of 98.9 ± 0.3% (range 98.4–99.3%).

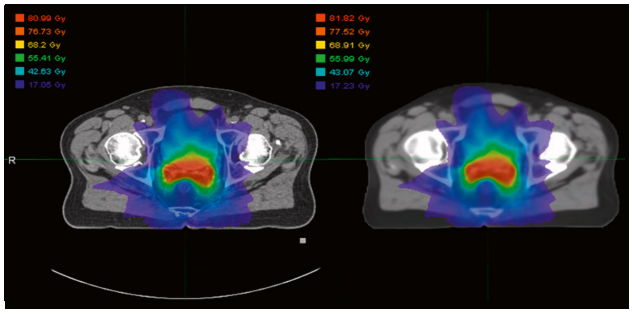

14 Exemplary dose distributions of a treatment plan calculated on the planning CT (left) and the MR-based Synthetic CT (right).

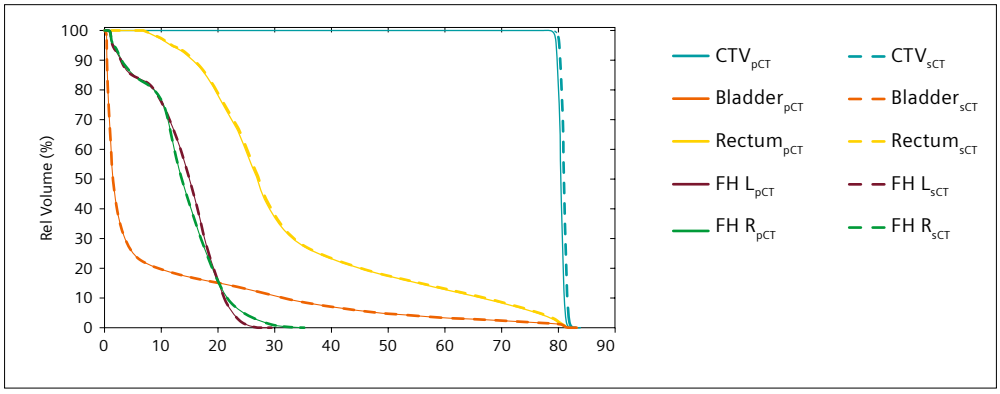

15 Dose volume histograms were compared in CTV and OARs (bladder, rectum, and femoral heads).

Patient	CTV (% difference)	Bladder (Gy)	Rectum (Gy)	Femoral head left (Gy)	Femoral head right (Gy)	Gamma 1%/2mm
1	-0.62%	-0.05	-0.15	-0.04	-0.08	99.1%
2	0.28%	0.02	-0.05	0.19	0.07	98.4%
3	-0.49%	-0.08	-0.31	0.01	-0.05	98.4%
4	-0.74%	-0.43	-0.62	0.06	0.12	99.2%
5	-0.08%	0.03	-0.33	0.07	0.09	99.3%
6	0.58%	-0.03	-0.13	-0.03	-0.03	99.3%
7	-0.30%	-0.01	-0.05	-0.14	-0.05	98.9%
Mean	-0.21%	-0.078	-0.23	0.017	0.01	98.9%
STD	0.44%	0.16	0.20	0.10	0.08	0.3%

Table 3: Differences in dose distributions of pCT- and Synthetic CT-based dose plans. Dose differences in CTV, PTV, and OAR were calculated as ΔDose = Dose(pCT) - Dose(rsCT).

Spatial localization accuracy results (CBCT registration)

Differences between rsCT-CBCT registration results and pCT-CBCT registration were assessed (Table 4). On average, 0.12 mm/-0.72 mm/-0.56 mm in x-, y-, and z-direction respectively (range: -1.8–1.4 mm) were observed.

Patient	1	2	3	4	5	6	7	Mean	STD
X (mm)	1.4	0.46	0.1	-1.3	0.08	-0.36	0.5	0.12	0.83
Y (mm)	-1.1	-1.06	-0.26	-1.22	-0.14	-1.44	0.2	-0.72	0.63
Z (mm)	-1.02	-1.2	-0.56	1.14	-0.48	0	-1.8	-0.56	0.94

Table 4: Difference in the translation vector (mm) between rsCT-CBCT registration and pCT-CBCT registration. Difference was calculated as translation (pCT)–translation (rsCT) in X, Y, Z axes.

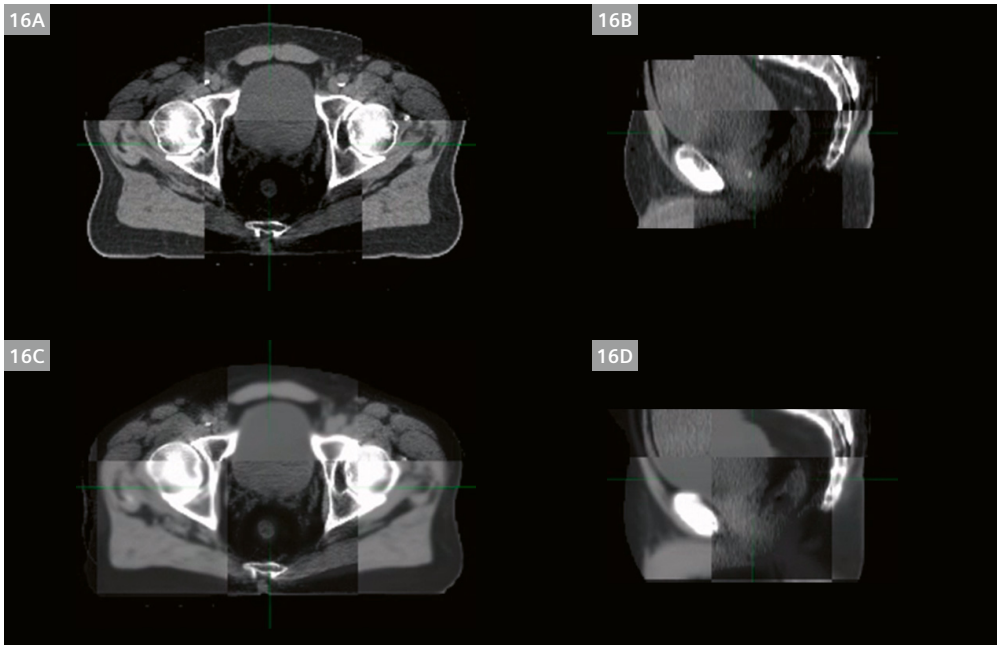

16 Localization accuracy comparison using the original planning CT data to CBCT registration as the reference **(16A, 16B)**, versus CBCT registration to the MR-based Synthetic CT **(16C, 16D)**.

2. Evaluation of the brain MR-based Synthetic CT from Universitätsklinikum Erlangen, Germany

A total of five brain cancer patients underwent MRI (MAGNETOM Sola 1.5T) and CT (SOMATOM go.Open Pro) simulation with a maximal time delay of five days. Both simulation images were acquired in a dedicated RT setup to minimize differences in the head position between MRI, CT, and RT treatment.

The five patients were scheduled for subsequent EBRT. All patients were treated with 6 MV X-rays using a VMAT (RapidArc) treatment technique with different dose prescriptions. A clinical treatment plan according to institutional clinical guidelines was optimized on the planning CT. The thermoplastic mask structure was removed on the planning CT image to obtain the same body contour as in Synthetic CT. The same plan was recalculated on the Synthetic CT. The mean doses of the target volumes (PTV, GTV) and OARS (brainstem, chiasma, optical nerves) were compared. In all the regions of interest, the mean dose differences were below 1% (normalized to the total planned dose).

The mean dose difference for PTV and GTV were overall below 1%, with a median of 0.06%. For the brainstem and chiasma, the mean dose difference was overall below 0.52% and 1.37% respectively.

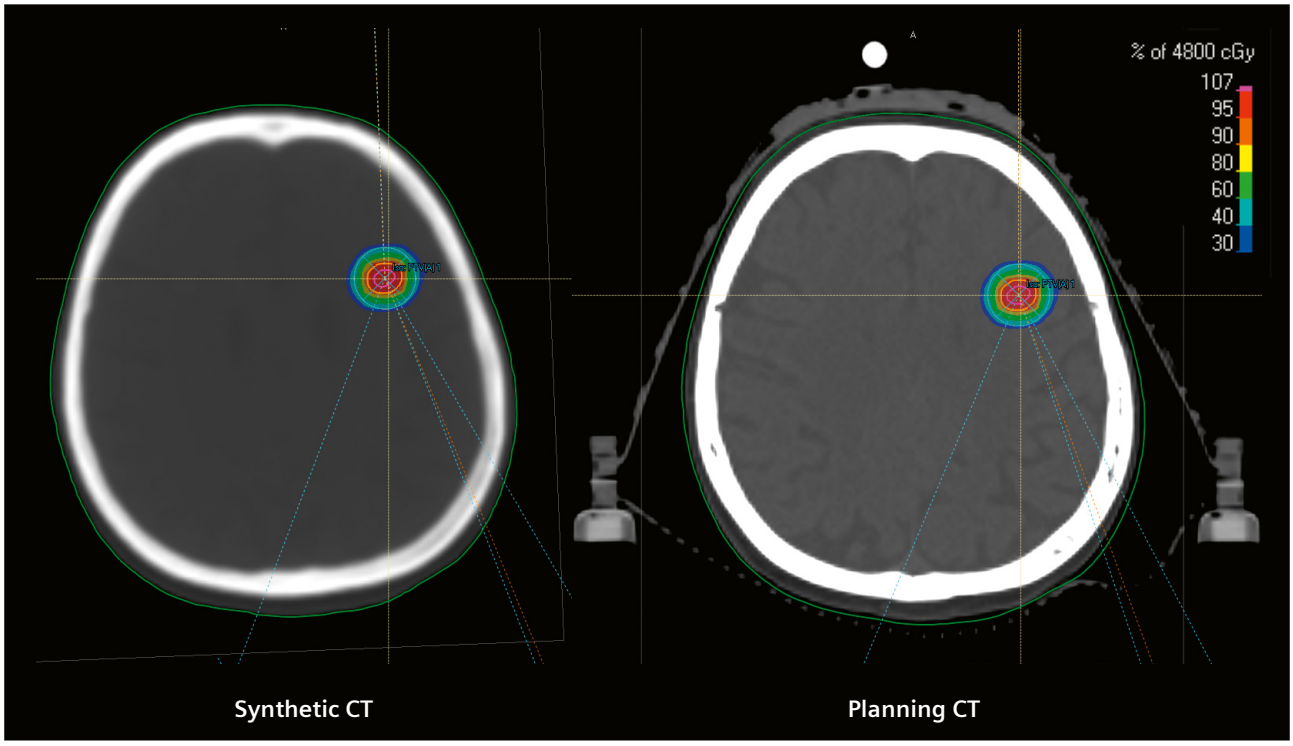

17 Dose distribution on Synthetic CT and CT with corresponding DVHs.

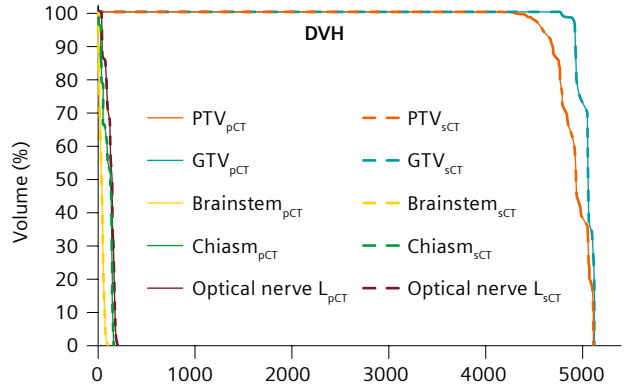

Mean dose [cGy] in ROI	on CT	on sCT
PTV	4919	4914
GTV	5045	5038
Brainstem	34	34
Chiasma	100	100
OPT_NRV_L	125	124
OPT_NRV_R	19	19

18 Mean dose on the planning CT and Synthetic CT (sCT) in six regions of interest for one patient.

Patient	Prescription dose	PTV	GTV	Brainstem	Chiasma
P1	12fx × 4 Gy	- 0.10	-0.14	0	0
P2	25fx × 2 Gy	0.08	0.08	0.17	0.42
P3	28fx × 1.8 Gy	0.83	0.85	0	1.37
P4	12fx × 4 Gy	- 0.04	-0.04	0.52	0.46
P5 (Plan 1)	1fx × 18 Gy	0.04	0.04	0	0
P5 (Plan 2)	1fx × 20 Gy	0.55	0.49	0	0
Median		0.06	0.06	0	0.21
95th percent		0.75	0.74	0.41	1.10
Max.		0.83	0.85	0.52	1.37

Table 5: Differences in dose distributions of planning CT and Synthetic CT in the PTV, GTV, and two organs at risk structures, the brainstem and chiasma, for the different patients. P5 has received two plans for two different target volumes.

Conclusion of clinical Synthetic CT evaluation

In pelvis and brain, dosimetric errors were small and on average < 1% for target structures. Automated matching localization errors for pelvis were small and, on average, ~ 1 mm along each axis. For brain, they were not evaluated.

A potential limitation is that fiducials (and some calcifications) are generally converted to soft tissue, which precludes the ability to localize by fiducial when preferred or necessary. In the special case of prostate SBRT, for example, it would be desirable to have a fiducial-based localization methodology implemented.

However, a method to contour the fiducials and override the HUs in the Synthetic CT is available in the *syngo*.via RT Image Suite. This method was not evaluated in this clinical study.

In conclusion, the MR-based Synthetic CT solution provided a clinically appropriate level of dosimetric and spatial accuracy for standard fractionation cases. Overall, the Synthetic CT created by *syngo*.via RT Image Suite VB601 provides a clinically reasonable alternative to a CT simulation exam and may be used clinically in the treatment planning and treatment of prostate pelvic standard fractionation radiation therapy as well as for brain treatment planning.

Clinical partners

Prof. Atchar Sudhyadhom, Ph.D. (Brigham and Women's Hospital, Boston, MA, USA); Siti Masitho, Ph.D. (Universitätsklinikum Erlangen, Germany); Prof. Christoph Bert, Ph.D. (Universitätsklinikum Erlangen, Germany); Florian Putz, Ph.D. (Universitätsklinikum Erlangen, Germany)

Software requirement	*syngo*.via RT Image Suite VB60; Deep learning-based Synthetic CT algorithm license
MRI scanner requirement and field strength	Training and testing were performed on a wide range of Siemens Healthineers 1.5T and 3T MAGNETOM MRI scanners: MAGNETOM Aera, MAGNETOM Skyra, MAGNETOM Sola, MAGNETOM Vida, MAGNETOM Sola Fit. The data acquisition protocols for Synthetic CT are available with *syngo* MR XA11A and later software versions for MAGNETOM RT Pro edition for MAGNETOM Vida and MAGNETOM Sola, with *syngo* XA30 and later software versions for MAGNETOM Aera and MAGNETOM Skyra.
In-plane resolution	1 × 1 mm brain; 2 × 2 mm pelvis
Slice thickness	Slice thickness is controlled by the input slice thickness, determined by the acquired input T1 VIBE-Dixon sequence.
Geometric distortion	The 3D distortion is automatically selected for the sequences in the RT Dot Engine.
Algorithm training	• Trained with a fixed number of datasets during product development and locked at the time of release. The algorithm does not learn continuously in the field. • Updates do not take place automatically. • Training and validation images were randomly assigned from the data pool. • Brain: 6486 training image sets (CT + MR) and 553 validation sets • Pelvis: 9059 training image sets and 695 validation sets • Data augmentation of the original data has been performed.
MR-based Synthetic CT generation	The acquisition time at the scanner is limited to only one sequence: T1 VIBE Dixon. Acquisition times may vary between 1 min 33 s and 4 min 12 s depending on field strength, clinical site, and acceleration modes.

Table 6: Practical information

References

1 R. W. Brown, Y.-C. N. Cheng, E. M. Haacke, M. R. Thompson, and R. Venkatesan, "Magnetic resonance imaging: physical principles and sequence design", John Wiley & Sons, 2014.
2 R. Speight et al., "IPEM Topical Report: An international IPEM survey of MRI use for external beam radiotherapy treatment planning", Phys. Med. Biol., vol. 66, no. 7, 2021.
3 G. P. Liney et al., "Quantitative evaluation of diffusion-weighted imaging techniques for the purposes of radiotherapy planning in the prostate", Br. J. Radiol., vol. 88, no. 1049, pp. 1–6, 2015.
4 W. D. Foltz et al., "Readout-segmented echo-planar diffusion-weighted imaging improves geometric performance for image-guided radiation therapy of pelvic tumors", Radiother. Oncol., vol. 117, no. 3, pp. 525–531, 2015.
5 D. Thorwarth, M. Notohamiprodjo, D. Zips, and A.-C. Müller, "Personalized precision radiotherapy by integration of multi-parametric functional and biological imaging in prostate cancer: a feasibility study", Z. Med. Phys., vol. 27, no. 1, pp. 21–30, 2017.
6 C. Dinis Fernandes et al., "Quantitative 3T multiparametric MRI of benign and malignant prostatic tissue in patients with and without local recurrent prostate cancer after external-beam radiation therapy", J. Magn. Reson. Imaging, vol. 50, no. 1, pp. 269–278, 2019.
7 M. A. Speight, Richard Dubec, Michael Eccles, Cynthia L George, Ben Henry, Ann Herbert, Trina Johnstone, Robert I Liney, Gary P McCallum, Hazel Schmidt, IPEM topical report: guidance on the use of MRI for external beam radiotherapy treatment planning. Physics in Medicine and Biology, 2021.
8 K. K. Brock, "Adaptive Radiotherapy: Moving Into the Future", Semin. Radiat. Oncol., vol. 29, no. 3, pp. 181–184, 2019.
9 K. Latifi, J. Caudell, G. Zhang, D. Hunt, E. G. Moros, and V. Feygelman, "Practical quantification of image registration accuracy following the AAPM TG-132 report framework", J. Appl. Clin. Med. Phys., vol. 19, no. 4, pp. 125–133, 2018.
10 QA cookbook: Commissioning and Quality Assurance (QA) for MAGNETOM systems in radiation therapy, siemens-healthineers.com/magnetom-world-rt 2021 HOOD05162003187576
11 C. Tsien, Y. Cao, and T. Chenevert, "Clinical Applications for Diffusion Magnetic Resonance Imaging in Radiotherapy", Seminars in Radiation Oncology, 24(3), 218–226, 2014.
12 M. A. Schmidt and G. S. Payne, "Europe PMC Funders Group Radiotherapy Planning using MRI", Phys. Med. Biol., vol. 60, no. 22, pp. R323–R361, 2015.
13 E. Paradis, C. Yue, T. S. Lawrence, C. Tsien, K. Vineberg, and J. M. Balter, "Assessing the dosimetric accuracy of MR-generated synthetic CT images for focal brain VMAT radiotherapy Eric", Int J Radiat Oncol Biol Phys, vol. 93, no. 5, pp. 1154–1161, 2015.
14 E. S. Paulson et al., "Consensus opinion on MRI simulation for external beam radiation treatment planning", Radiother. Oncol., vol. 121, no. 2, pp. 187–192, 2016.
15 E. Johnstone et al., "Systematic Review of Synthetic Computed Tomography Generation Methodologies for Use in Magnetic Resonance Imaging–Only Radiation Therapy", Int. J. Radiat. Oncol. Biol. Phys., vol. 100, no. 1, pp. 199–217, 2018.
16 L. Vandewinckele et al., "Overview of artificial intelligence-based applications in radiotherapy: Recommendations for implementation and quality assurance", Radiother. Oncol., 2020.
17 C. K. Glide Hurst et al., "Task Group 284 Report: Magnetic Resonance Imaging Simulation in Radiotherapy: Considerations for Clinical Implementation, Optimization, and Quality Assurance", Med. Phys., 2021.
18 J. M. Edmund and T. Nyholm, "A review of substitute CT generation for MRI-only radiation therapy", Radiat. Oncol., vol. 12, no. 1, pp. 1–15, 2017.
19 D. A. Low et al., "A technique for the quantitative evaluation of dose distributions", Med Phys May; 25(5): 565-61, 1998.

Contact

Michaela Hösl, Ph.D.
Global Product Marketing Manager
Cancer Therapy
Siemens Healthineers VAR CTH M&S PMK
91294 Forchheim, Germany
michaela.hoesl@siemens-healthineers.com

Clinical Evaluation of a Receiver Coil Custom Designed for MR Simulation of Immobilized Patients

James M Balter[1,2]; Dinank Gupta[2]; Michelle M Kim[1]; James A Hayman[1]; Karen Vineberg[1]; Yue Cao[1,2]; Daniel Gareis[3]; Dan Coppens[4]

[1]Department of Radiation Oncology, University of Michigan, Ann Arbor, MI, USA
[2]Department of Biomedical Engineering, University of Michigan, Ann Arbor, MI, USA
[3]NORAS MRI products GmbH, Höchberg, Germany
[4]Qfix, Avondale, PA, USA

Introduction

There has been significant adoption and/or adaptation of MR scanners to support the needs of Radiation Oncology treatment simulation. A plethora of MR-compatible immobilization devices and phantoms have been developed and imaging sequences have been customized to better suit the needs of supporting planning and guidance of precision radiation treatments. In addition, a number of synthetic CT generation tools have been released commercially. To date, however, little has been done to customize RF coils to better suit the needs of scanning patients immobilized for radiation therapy treatment. This issue was noted as one potential concern for maintaining consistent image quality for scanning certain body sites, most notably the head and neck region. Most existing coil combinations suffer from challenges including increased claustrophobia due to placing coils in high proximity to the patient's eyes, poor SNR due to contributing coil elements being placed distal to the anatomy being scanned, image intensity non-uniformities and technical challenges for reproducibly and conveniently assembling coil combinations around the patient [1].

While a few attempts have been made at customizing existing coil combinations and/or building unique holders for use of existing coils [2], very little effort has been placed in truly optimizing receiver coils for radiation therapy simulation purposes. The introduction of a flexible coil that can be integrated into an immobilization mold has demonstrated the promise of such technology for radiation therapy simulation [3]. To date, however, no such coils have been developed with intracranial radiation

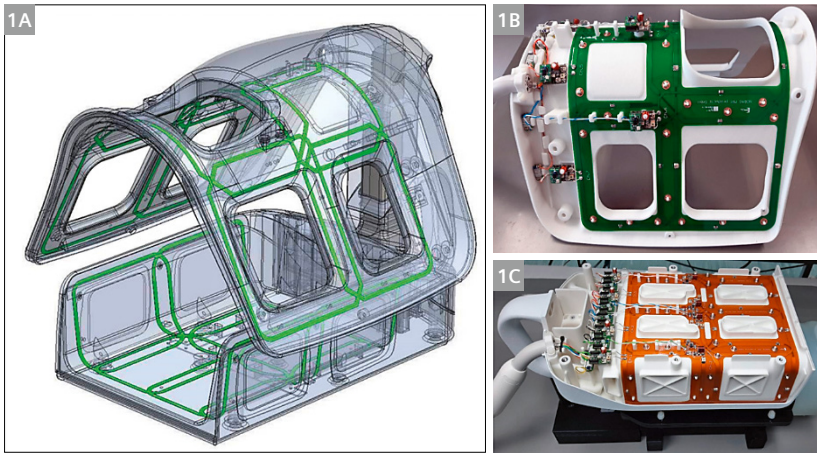

1 Schematic diagram of Encompass receiver coil **(1A)**, as well as pictures of the compositions of the anterior **(1B)** and posterior **(1C)** structural elements.

therapy in mind. This report describes a novel coil that was designed to be conveniently integrated with a commonly used commercially available immobilization system. The performance of this coil on phantom as well as patient images, as well as utility to support MR-only simulation for precise treatment of intracranial tumors, is reported.

Methods

The Encompass coil[1] was developed in partnership with two companies (Qfix and NORAS), with specifications developed specifically to support scanning of patients immobilized using the Encompass™ line of cranial immobilization equipment. The coil consists of two separate components, an anterior 7-channel coil and a posterior 8-channel coil. A design diagram and internal images of the coil are shown in Figure 1. The coil was designed to minimize B_0 and B_1 distortions, and incorporate low-noise preamplifiers, active and passive decoupling, and a safety fuse in each channel. The patient is positioned with the posterior component in place, and the anterior section is then attached via a height-adjustable stand. To reduce noise and increase comfort, patients are given ear plugs prior to being placed in their immobilization masks. Figure 2 shows an example image of a patient being positioned in the coil for MR Simulation.

To evaluate the performance of this coil, a series of patient and phantom scans were performed. The ACR standard phantom was scanned using the Encompass coil on a 3T MRI Simulator (MAGNETOM Skyra, Siemens Healthcare, Erlangen, Germany), and resulting images compared to those acquired using a standard 20-channel head and neck coil as well as a combined anterior 18-channel surface coil and 8 elements of a posterior spinal coil in a configuration compatible with scanning patients immobilized in masks for Radiation Oncology treatment [4], referred to herein as RTCombo.

Under an institutional review board-approved protocol, a series of 10 patients with intracranial tumors who were scheduled for stereotactic treatment were scanned using the Encompass coil following conventional CT-based simulation for intracranial stereotactic treatment planning. Standard T1-weighted post-contrast, T2 FLAIR, diffusion-weighted (using an echo planar sequence), and T1 VIBE Dixon images (in support of synthetic CT generation for MRI-only treatment planning and positioning support) were acquired. A subset of these patients were further scanned, without immobilization, using the 20-channel head and neck coil.

Diffusion-weighted images (at b = 0 s/mm^2) were analyzed to estimate the relative signal to background ratio, which was compared to measurements of equivalent images from other subjects scanned using the 20-channel head and neck coil under different research protocols.

Synthetic CT image volumes were generated using a Unet architecture previously trained on 6500 MR-CT image pairs, from T1-weighted (in-phase) images acquired using the VIBE Dixon sequence [5]. These images were compared to simulation CT scans acquired for radiosurgical treatment planning for intensity similarity, accuracy of dose calculation, and accuracy of supporting alignment to Cone Beam CT (CBCT) scans used for patient positioning. The synthetic CT scans were spatially aligned to the treatment planning CT scans using rigid body transforms. Using a previously reported comparison method [4], treatment plans were generated using the synthetic CT scans for attenuation mapping. These plans were then re-calculated using attenuation mapped from the treatment planning CT scans, and the resulting differences in dose recorded.

The cone beam CT (CBCT) image volumes used to support patient positioning for treatment for these subjects were spatially aligned to the CT as well as synthetic CT scans, and the differences in the transformations were recorded.

[1] *While this study has been performed using the prototype coil, the Qfix Encompass 15-channel Head Coil is released and available for sale.*

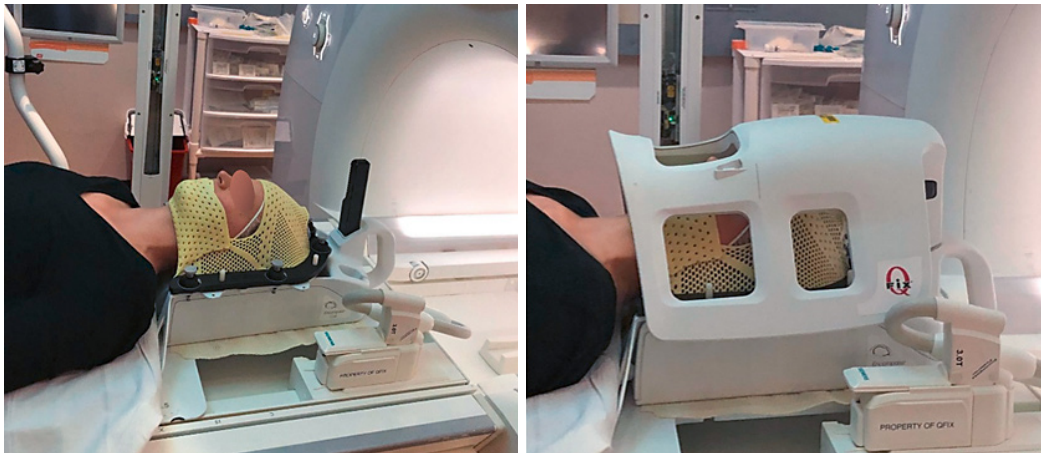

2 Example patient positioning using the Encompass coil. The immobilization frame is indexed to the posterior coil section, and the anterior coil is subsequently attached via a height-adjustable connection.

Results

Figure 3 shows images from the various sections of the ACR phantom from the Encompass coil as well as the 20-channel coil. All tests passed successfully. Figure 4 shows images from the uniform section of the phantom scanned with the Encompass, 20-channel head and neck, as well as combined anterior surface and posterior spine coils. The prototype coil passed all ACR phantom test criteria. SNR values, measured in the center of the uniform section of the phantom, were 88.5, 89.9 and 44.4 for the prototype, 20-channel and RTCombo coils, respectively.

Human subject images (examples shown in Figure 5) were qualitatively reviewed by a physician specializing in intracranial treatment and deemed to be of sufficient quality for clinical use. Analysis of ADC maps from DWI showed higher signal to background ratio for the prototype coil (20.7) versus the 20-channel coil (15.6). Figure 6 shows a comparison of a synthetic CT scan, generated from the T1 VIBE images, to the corresponding clinical CT scan acquired for simulation.

The synthetic CT image volumes compared well with simulation CT scans, with average Mean Absolute Error values of 4.7, 180.5 and 5.7 HU in regions of brain parenchyma, skull, and ventricles across the 10 patients studied, similar to those reported using a 20-channel head and neck coil for non-immobilized patients [5]. Figure 7 shows an example of a treatment plan generated using the synthetic CT from the Encompass coil-acquired VIBE images, as well as that plan with dose re-calculated using the attenuation map generated from the treatment planning CT scan. Treatment plan comparisons across the 10 patients showed dose differences of 2.3 +/-0.9% of the mean dose to the planning target volumes, with the systematic mean dose variation primarily due to the lack of the immobilization frame in the synthetic CT image volumes.

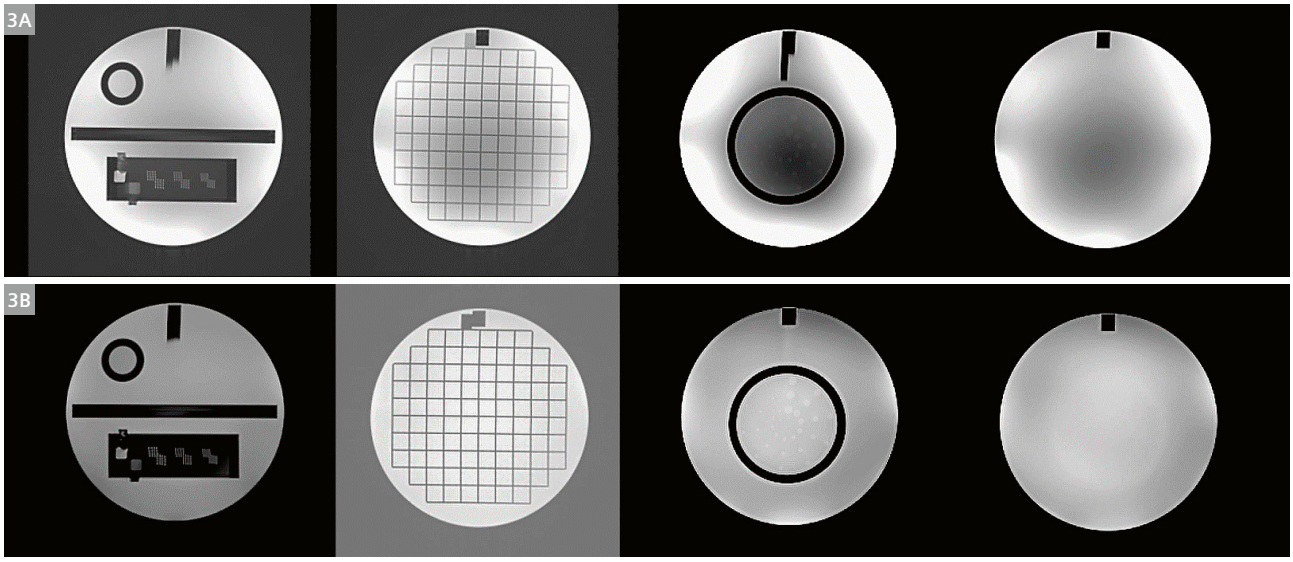

3 Sections of the ACR QA phantom scanned with the Encompass coil **(3A)** and 20-channel conventional Head and Neck coil **(3B)**.

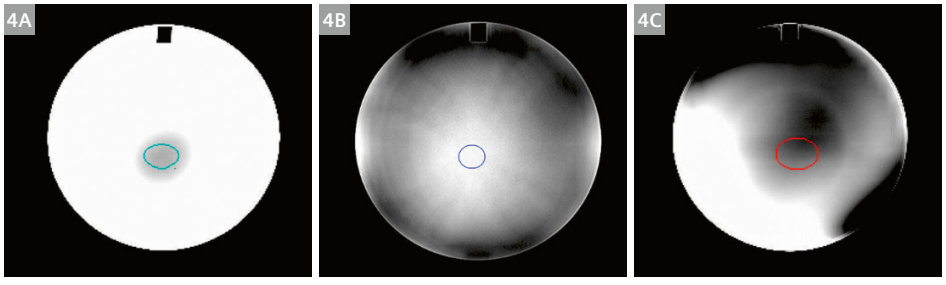

4 Uniform sections of the ACR phantom and regions of interest (contours) used to assess SNR from the **(4A)** Encompass, **(4B)** 20-channel head and neck coil, and **(4C)** RTCombo coil combination.

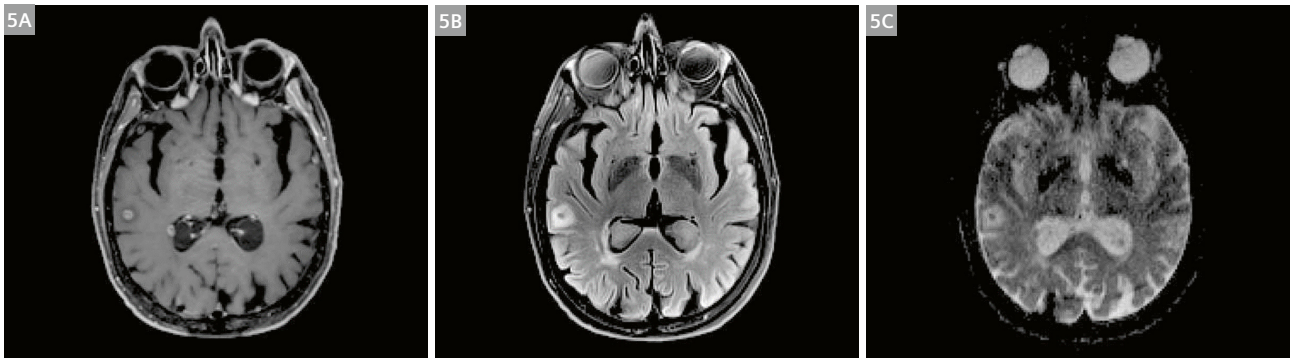

5 Example T1-weighted post contrast **(5A)** and Fluid Attenuated Inversion Recovery **(5B)** images, along with a map of Apparent Diffusion Coefficients **(5C)** for a subject acquired using the Encompass coil.

6 Example synthetic CT image volume **(6A)** generated from images acquired with the Encompass coil and actual CT **(6B)** acquired for treatment planning.

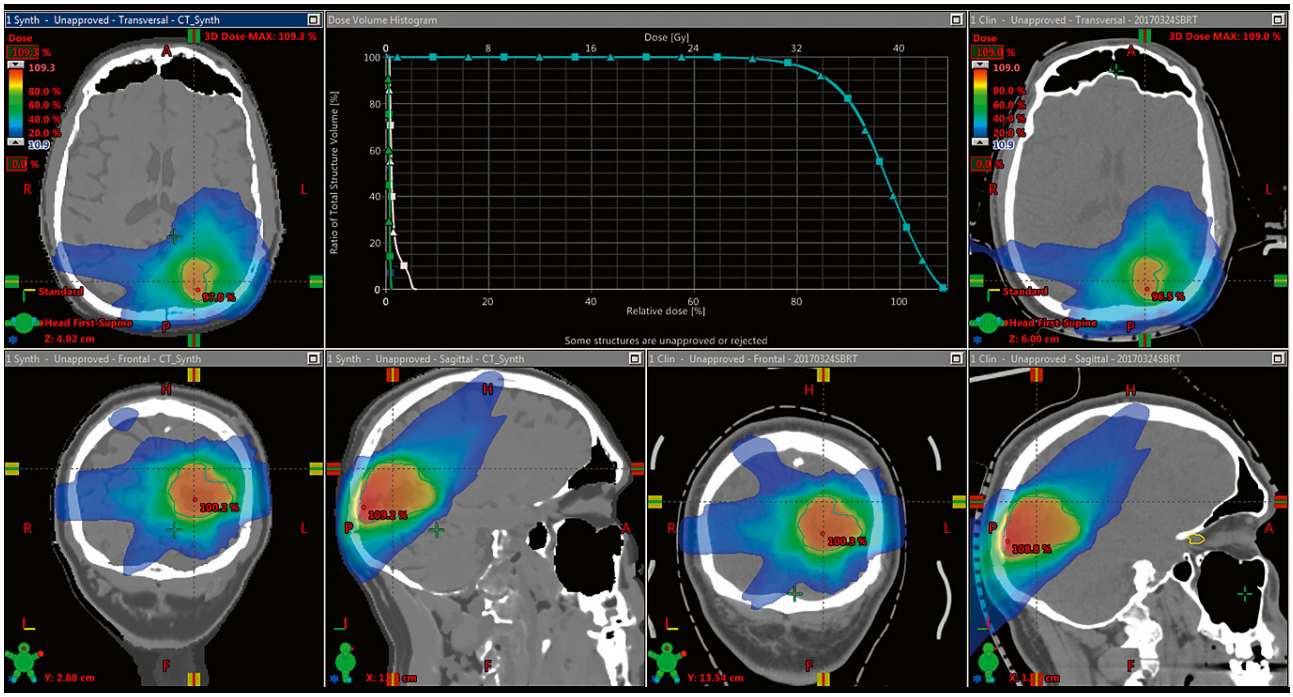

7 Comparison of dose distributions for a plan generated using the synthetic CT from the Encompass coil simulation (left, plan "1 Synth") with that from the treatment fluences used to recalculate dose using the attenuation map from the clinical CT scan (right, plan "1 Clin"). Dose volume histograms are shown for the synthetic CT (squares) and clinical (triangles) plans for the treatment target (blue), brainstem (white) and optic chiasm (green).

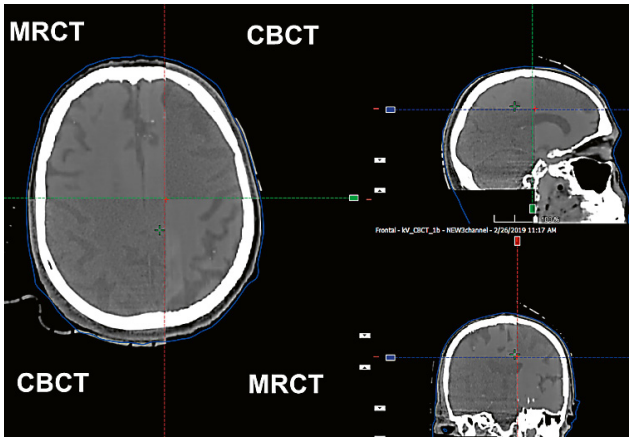

8 Example alignment of a synthetic CT (MRCT) generated from VIBE Dixon images acquired using the Encompass coil with a cone beam CT (CBCT) scan acquired for patient positioning.

	Left-Right	Ant-Post	Inf-Sup
mean	-0.04	0.00	0.07
σ	0.14	0.20	0.23
min	-0.3	-0.5	-0.3
max	0.3	0.4	0.5

Table 1: Differences between CBCT-CT and CBCT-synthetic CT alignments applied to target centers (mm)

Figure 8 shows an example alignment of synthetic CT with CBCT from a treatment. Table 1 summarizes the differences between CBCT-CT and CBCT-synthetic Alignment. A mean difference between CT and Synthetic CT of 0.1 mm (standard deviation of 0.3 mm) was observed across all patients.

Conclusion

Tests performed on the Qfix Encompass coil[1], designed to support MR simulation for immobilized patients, demonstrated image quality comparable to commercial general purpose coils for clinical use for precision radiation therapy of intracranial stereotactic treatment targets. Synthetic CT images generated using this coil are sufficiently similar to CT scans to support MR-only treatment planning and image guided patient positioning for radiosurgery.

Acknowledgments

Supported by NIH R01EB016079 and Qfix.

References

1 Glide-Hurst CK, Paulson ES, McGee K, et al. Task Group 284 Report: Magnetic Resonance Imaging Simulation in Radiotherapy: Considerations for Clinical Implementation, Optimization, and Quality Assurance. Med Phys. 2021.
2 Paulson ES, Erickson B, Schultz C, Allen Li X. Comprehensive MRI simulation methodology using a dedicated MRI scanner in radiation oncology for external beam radiation treatment planning. Med Phys. 2015;42(1):28-39.
3 Tyagi N, Zakian KL, Italiaander M, et al. Technical Note: A custom-designed flexible MR coil array for spine radiotherapy treatment planning. Med Phys. 2020;47(7):3143-3152.
4 Paradis E, Cao Y, Lawrence TS, et al. Assessing the Dosimetric Accuracy of Magnetic Resonance-Generated Synthetic CT Images for Focal Brain VMAT Radiation Therapy. Int J Radiat Oncol Biol Phys. 2015;93(5):1154-1161.
5 Gupta D, Kim M, Vineberg KA, Balter JM. Generation of Synthetic CT Images From MRI for Treatment Planning and Patient Positioning Using a 3-Channel U-Net Trained on Sagittal Images. Front Oncol. 2019;9:964.

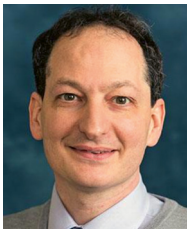

Contact

James M. Balter, Ph.D., FAAPM
Professor and Associate Chair
for Physics Research
Department of Radiation Oncology
University of Michigan
Tel.: +1 (734)936-9486
jbalter@umich.edu

Meet Siemens Healthineers

Varian is part of Siemens Healthineers. Together, we are better positioned to push the boundaries of innovation and shape the future of healthcare and cancer care. The people working for Varian, a Siemens Healthineers Company, are committed to the company they work for, and are passionate about the opportunities ahead to accelerate our global patient impact and transform oncology. In this section we introduce you to colleagues from all over the world – people who put their hearts into what they do.

David Schaal, Ph.D.

Dave Schaal graduated with a Ph.D. in experimental analysis of behavior from the University of Florida in 1988. He completed a postdoctoral fellowship in neurobehavioral pharmacology at the University of Minnesota before accepting a position in the Department of Psychology at West Virginia University in 1991. His lab conducted research on the effects of psychotropic drugs on animals' sense of passing time. He joined the Department of Neurosurgery at Stanford in 2002, collaborating on research on neuroprotection from stroke. There he worked with John Adler, inventor of the CyberKnife Robotic Radiosurgery System, which eventually led to his career in the radiation oncology industry. After years at Accuray Incorporated and ViewRay Incorporated, Dave happily joined the Medical Affairs team at Varian Medical Systems, where he heads the Strategic Publications Group, and learns something new every day.

Palo Alto, CA, USA

How did you first come into contact with MRI?
I have two experiences with MRI, despite not technically working in the field. At Stanford, CA, USA, I worked with researchers who labeled neural stem cells with superparamagnetic iron oxide nanoparticles, then implanted them near damage caused by experimentally induced cortical stroke in rats. A 7T scanner allowed detection of the cells as they migrated toward the stroke damage – it was fascinating. More recently I worked for ViewRay, and learned about the potential benefits of guiding radiotherapy with MRI. When I joined Varian I was happy to focus at least some of my efforts on the Ethos device, which is a clear competitor with ViewRay despite not having an onboard MRI.

What do you find most motivating about your job?
I loved academia – research and teaching and service to colleagues – and unless I'd found a way to satisfy those passions in an industry setting, I would not have considered leaving that life. But I have been lucky to be in a position that requires constant reading, learning, teaching, and service to colleagues, for each company I worked for. Being able to continue and share my love of science is extremely motivating for me. I'm grateful to have found my passions in a business that allows international travel and friendships and requires me to pay attention to the leading edge of the fascinating and constantly changing field of oncology.

What do you think are the most important developments in radiation oncology?
In the last generation technological developments have allowed the creation of radiation treatments delivered extremely precisely to a 3D volume that conforms closely to the tumor and minimizes radiation exposure to nearby normal tissues. This required the development of high-quality 3D CT imaging (often supplemented by MR imaging), computer-aided creation of 3D volumetric treatment plans based on that 3D imaging, delivery technology (such as the multi-leaf collimator, or MLC) to deliver 3D plans, software and hardware to further refine those plans (i.e., intensity-modulated radiotherapy, or IMRT), and on-table imaging and dose tracking technology to assure that these exquisitely created plans are accurately delivered. Delivery improvements such as volumetric modulated arc therapy (VMAT), non-coplanar delivery, and real-time tracking of the target location improved things further. We are now at the point of being able to adapt plans based on pre-session on-table 3D imaging, further reducing the impact of day-to-day anatomical variation on treatment

quality. Soon, I'm sure, it will be routine to also adapt based on biological information about the target. To all this we can add patient- and tumor-specific genomic information, targeted systemic and immunotherapies, a proliferation of minimally invasive local tumor treatments in addition to precision radiotherapy, and lots of promising future developments, and we're in a position to give primary and metastatic cancer patients an excellent chance of cure and extended high-quality life. It's exciting to be part of these consequential developments.

If you could do whatever you wanted for a month, what would you do?
I'd love to take my wife, dog, and musical instruments to a cottage on the Atlantic coast of Nova Scotia, Canada. We'd go to sleep to the sound of the surf, we'd play and create music, we'd take long walks with the dog, we'd read books. We have family in Nova Scotia that we could visit. There's also a wild animal rescue facility nearby where we could volunteer. And we'd spend some time thinking about what awaits us when our work life is over.

Get to know us

Find more portraits of our colleagues around the world!

www.magnetomworld.siemens-healthineers.com/meet-siemens-healthineers

Not for distribution in the US

On account of certain regional limitations of sales rights and service availability, we cannot guarantee that all products included in this brochure are available through the Siemens sales organization worldwide. Availability and packaging may vary by country and is subject to change without prior notice. Some/All of the features and products described herein may not be available in the United States.

The information in this document contains general technical descriptions of specifications and options as well as standard and optional features which do not always have to be present in individual cases, and which may not be commercially available in all countries.

Due to regulatory reasons their future availability cannot be guaranteed. Please contact your local Siemens organization for further details.

Siemens reserves the right to modify the design, packaging, specifications, and options described herein without prior notice. Please contact your local Siemens sales representative for the most current information.

Note: Any technical data contained in this document may vary within defined tolerances. Original images always lose a certain amount of detail when reproduced.

Siemens Healthineers Headquarters
Siemens Healthcare GmbH
Henkestr. 127
91052 Erlangen, Germany
Phone: +49 9131 84-0
siemens-healthineers.com

Published by Siemens Healthcare GmbH · Order No. A91MR-1100-114C-7600 · Printed in Germany · 11835 0422 · *©Siemens Healthcare GmbH, 2022*

siemens-healthineers.com/magnetom-world-rt